CYTOTOXICOLOGICAL RESPONSE TO ENGINEERED NANOMATERIALS: A PATHWAY-DRIVEN PROCESS

A Dissertation

by

AMELIA ANTONIA ROMOSER

Submitted to the Office of Graduate Studies of
Texas A&M University
in partial fulfillment of the requirements for the degree of

DOCTOR OF PHILOSOPHY

May 2012

Major Subject: Toxicology

Cytotoxicological Response to Engineered Nanomaterials: A Pathway-Driven Process

CYTOTOXICOLOGICAL RESPONSE TO ENGINEERED NANOMATERIALS: A PATHWAY-DRIVEN PROCESS

A Dissertation

by

AMELIA ANTONIA ROMOSER

Submitted to the Office of Graduate Studies of
Texas A&M University
in partial fulfillment of the requirements for the degree of

DOCTOR OF PHILOSOPHY

Approved by:

Co-Chairs of Committee,	Christie M. Sayes
	Michael F. Criscitiello
Committee Members,	Weston Porter
	Michael McShane
Intercollegiate Faculty Chair,	Weston Porter

May 2012

Major Subject: Toxicology

ABSTRACT

Cytotoxicological Response to Engineered Nanomaterials: A Pathway-Driven Process.

(May 2012)

Amelia Antonia Romoser, B.S., Texas A&M University

Co-Chairs of Advisory Committee: Dr. Christie M. Sayes
Dr. Michael F. Criscitiello

Nanoparticles, while included in a growing number of consumer products, may pose risks to human health due to heavy metal leaching and/or the production of reactive oxygen species following exposures. Subcellular mechanisms of action triggered as a result of exposure to various nanoparticles are still largely unexplored. In this work, an effort to elucidate such toxicological parameters was accomplished by evaluating oxidative stress generation, changes in gene and protein expression, and cell cycle status after low-dose exposures to a variety of metal and carbon-based nanomaterials in primary human dermal cells. Additionally, mitigation of nanoparticle toxicity via microencapsulation was investigated to assess the feasibility of utilizing nanomaterials in dermally implantable biosensor applications.

Cellular immune and inflammatory processes were measured via qPCR and immunoblotting, which revealed gene and protein expression modulation along the NF-κB pathway after a variety of nanoparticle exposures. The role of immunoregulatory transcription factor NF-κB was examined in an oxidative stress context in cells exposed to a panel of nanoparticles, whereby glutathione conversion and modulation of oxidative

stress proteins in normal and NF-κB knockdown human dermal fibroblasts were monitored. Results revealed decreased antioxidant response and corresponding increased levels of oxidative stress and cell death in exposed normal cells, compared to NF-κB incompetent cells. However, reactive oxygen species production was not an absolute precursor to DNA damage, which was measured by the comet assay, γ-H2AX expression, and flow cytometry. Protein analysis revealed that map kinase p38, rather than p53, was involved in the halting of the cell cycle in S-phase after ZnO exposures, which caused DNA double strand breaks.

Microencapsulation of fluorescent quantum dot nanoparticles, specifically, was utilized as a method to improve system functionality and surrounding cellular viability for the purpose of a dermal analyte detection assay. *In vitro* results indicated a functional localization of nanoparticles, as well as cessation of cellular uptake. Subsequently, cellular metabolism was unaffected over the range of time and concentrations tested in comparison to unencapsulated quantum dot treatments, indicating the usefulness of this technique in developing nanoparticle-driven biomedical applications.

ACKNOWLEDGEMENTS

I would like to thank my committee chairs, Dr. Christie Sayes and Dr. Michael Criscitiello for their tireless support and extension of knowledge. They have both been exceptional mentors to me in many aspects of life. My remaining committee members, Dr. Michael McShane and Dr. Weston Porter, have also given their guidance and support freely throughout the course of this research. Furthermore, Drs. Criscitiello, Porter, and McShane have each graciously participated in successful research collaborations, serving to diversify my research experience while in the toxicology program.

Additionally, I would like to thank several professors who have assisted me in collaborative efforts. Dr. Kenith Meisner, TAMU Biomedical Engineering, committed his time and knowledge in an extensive effort that resulted in publication and a furthering of my understanding in microencapsulation and the physics of materials science. Thanks to Dr. Robert Burghardt, Director of the TAMU College of Veterinary Medicine Image Analysis Center, a gifted instructor of microscopy techniques and image acquisition.

Dr. Stephen Safe and his laboratory have been instrumental in guiding me in protein analysis techniques. Many in the Safe lab, including Sandeep Sreevalsan, Indira Jutooru, and Gayathri Chadalapaka provided regular suggestions and expertise. Dr. Weston Porter's graduate student, Kelly Scribner, was a constant source of support to me and great personal friend.

My sincere appreciation goes to my lab members, J. Michael Berg, Ahmed Ridha, Aishwarya Sooresh, and David Figueroa, who provided daily encouragement, inspiration, and insight throughout my program at Texas A&M University. Finally, thanks to my parents for their belief in me and to my husband and daughter for their patience, love, and support.

TABLE OF CONTENTS

CHAPTER Page

LIST OF FIGURES

FIGURE Page

FIGURE Page

LIST OF TABLES

CHAPTER I

INTRODUCTION

Nanomaterials are defined as materials that have at least one dimension between 1-100 nm (1 nm = 10^{-9} m) and typically exhibit physicochemical properties not shared by coarser particles of the same chemical composition (Académie des Sciences and Académie des Technologies, 2004; Hansen et al., 2007; Nanoscale Science Engineering and Technology Subcommittee, 2004; The Royal Society and The Royal Academy of Engineering, 2004). The actual size threshold whereby these new properties can be seen is still a matter of debate and a new study has reported that 30 nm and less for metal and metal-oxide particles is nearer to the point at which this phenomenon actually occurs (Auffan et al., 2009a). At this scale, the much larger particle surface-to-volume ratio plays a significant role in interaction at the biological interface. Due to the 'non-bulk' properties of nanoparticles, including their atypical surface structure and surface reactivity, processes such as dissolution, redox reactions or the generation of reactive oxygen species may be enhanced. Such properties may elicit biological responses that would not be produced by larger particles of the same chemical composition.

1.1. Nanoparticle uses and dermal exposure

Nanotechnology is among the fastest growing areas of scientific research and has important applications in a wide variety of fields. The nanotechnology industry is

---

This dissertation follows the style of Molecular Immunology.

expected to generate revenues between $2.6 trillion and $3.1 trillion by the years 2014 and 2015, respectively (Dai, 2010; Schmidt, 2009). Since 2005, the number of consumer products containing nanomaterials has increased dramatically each year, and approximately half of these products are of dermal relevance, such as cosmetic, sunscreen, and personal care products (Figure 1.1) (Woodrow Wilson International Center for Scholars, 2011). Applications include incorporation into commercially available products such as cosmetics and sunscreens, pharmaceuticals, stain resistant and insect resistant clothing, wound care strategies, sports equipment, dental bonding, and cleaning products. Additionally, there are many current and possible future applications for nanotechnologies as drug delivery systems, nanomedicine components, environmental remediators, and cellular imaging agents.

Nanomaterials afford many unique advantages over larger sized materials, such as antioxidative and antibacterial properties, increased variation in material color, and improved light scattering ability. However, while these novel applications continue to expand in breadth, there is increasing concern regarding the safety of these materials. It has been estimated that $2.6 trillion in manufactured goods will contain nanomaterials by 2014, as 3 to 4 emerging nanotechnology-based consumer products are entering the market per week (National Institute of Standards and Technology (NIST), 2009). That said, the overall safety of acute or chronic exposures to nanoparticles arising from widespread use of nanoparticles and products containing nanoparticles remains relatively unknown. It is known that heavy metals are known to be detrimental to human and environmental health. Many of these new products contain nanoparticles comprised of

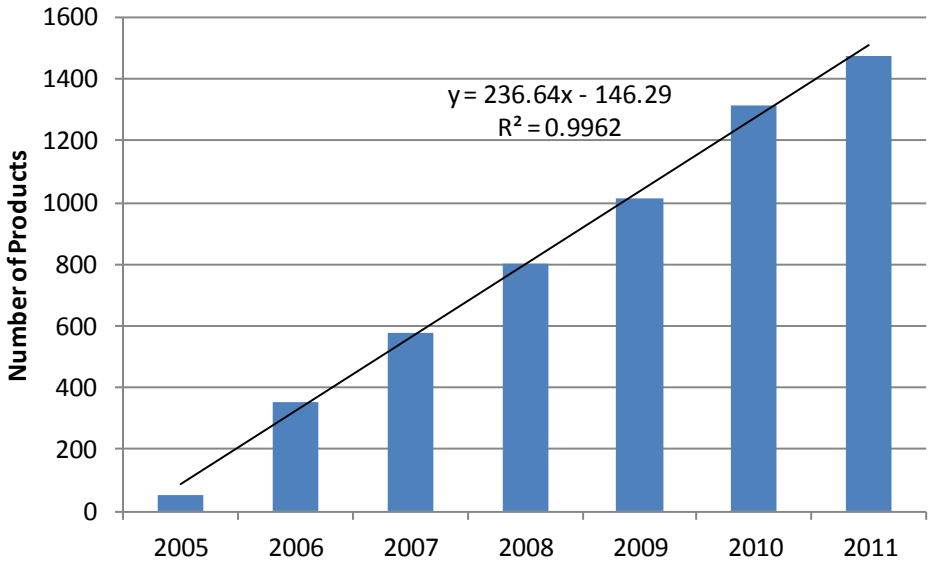

Fig. 1.1 Nanoparticle incorporation into consumer products. The trend in commercially available consumer products containing nanomaterials since the year 2005 is represented. Approximately half of these products in any given year are used in dermal applications. (Adapted from Nanotechnology Consumer Products Inventory, Woodrow Wilson International Center for Scholars, 2011).

bioavailable metals such as silver, zinc, iron, and cadmium, to name a few.

Within the emerging discipline of Nanotoxicology, there exists a gap between materials safety evaluation and the technology developments that are swiftly producing new materials, synthesis techniques, applications, and products ready for the market. The 2004 Royal Society & the Royal Academy of Engineering report stated that nanoparticles should be treated as new chemicals from a risk perspective because they can overcome the body's normal protective barriers due to their very small size (Nasterlack et al., 2008; National Institute of Occupational Safety and Health (NIOSH), 2007; Schulte et al., 2008; The Royal Society and The Royal Academy of Engineering, 2004). The fact that nanoparticles are a thousand times smaller than most microscale materials tested to date raises concern regarding human exposure (Kielhorn et al., 2006). Nanoparticles are capable of breaching biological barriers via inhalation, dermal absorption, and the digestive tract (Alvarez-Roma et al., 2004; Baroli et al., 2007; Chen and Schluesener, 2008; Hillyer and Albrecht, 2001; Jani et al., 1990; Oberdorster et al., 1994; Peters et al., 1997; Ryman-Rasmussen et al., 2006), as well as by voluntary injection, absorption, or implantation for pharmaceutical delivery systems (Bianco et al., 2005; Guterres et al., 2006; Klumpp et al., 2006; Lademann et al., 1999). With regard to dermal exposures, humans are likely to encounter nanoparticles by one of the following three ways: occupational exposure, consumer product exposure, or biomedical application exposure. The skin is the largest organ of the body, accounting for more than 10% of body mass. It possesses the crucial role of protective barrier to the external environment, as well as other functions such as homeostasis maintenance and

metabolism. Depending on the physicochemical properties of the material in contact with skin, multiple pathways of penetration across the skin barrier have been identified, including intercellularly, transcellularly, and via hair follicles and sweat glands (Scheuplein, 1967). A variety of factors, including skin barrier integrity, anatomical location, and presence of skin diseases such as atopic eczema, contact dermatitis, and psoriasis can influence extent of the dermal uptake at the site of exposure (Crosera et al., 2009). Injury, such as that from UV exposure and wounds are also factors to consider, as well as age and hydration state. Moreover, flexing of the skin, detergents, and chemicals can increase skin absorption (Filon et al., 2006; Nielsen et al., 2007).

A handful of studies in the literature exist that have investigated the ability of nanoparticles to penetrate skin (Baroli et al., 2007; Chen and Schluesener, 2008; EPA, 2007; Filon et al., 2006; Gopee et al., 2009; Isakovic et al., 2006; Kielhorn et al., 2006; Mortensen et al., 2008; Oberdorster et al., 2005; Rouse et al., 2007; Samberg et al., 2010; Senzui et al., 2010; Xia et al., 2010; Zhang and Monteiro-Riviere, 2008), but many fewer have been able to quantify the amount of nanomaterial that was capable of breaching the stratum corneum (Gopee et al., 2009; Wu et al., 2009). Discrepancies in published results are common, however, and seem to be related to differences in techniques and methods utilized, absence of standardized protocols, and varying laboratory conditions. The skin is often considered less permeable and the risk perception by this route is less than that of respiratory exposures (Donaldson et al., 2006; Limbach et al., 2007; Nel et al., 2006; Oberdorster et al., 2005; Shimada et al., 2006). However, in the literature there are studies which suggest that the skin is an important

route of entry for nanoparticles both in occupational and consumer settings (Gopee et al., 2009; Mortensen et al., 2008; Ryman-Rasmussen et al., 2006; Sonavane et al., 2008; Vogt et al., 2006) and it has been specifically shown that certain particles are more prone to dermal penetration based upon their physicochemical properties or the nature of the vehicle they are suspended in (Xia et al., 2010).

Human skin consists of the epidermis, dermis, and subdermis. The epidermis, or outermost layer of dermal tissue, consists of the stratum corneum and underlying tissue, mainly comprised of keratinocytes. Upon topical application of a foreign substance, penetration through the stratum corneum depends upon many factors, regarding both the dermal tissue and the substance. Factors that affect flux of solute include molecular size (MW), octanol–water partition coefficient (Kow) and melting point (Mpt) of the solute (Roberts and Sloan, 2000). It has also been reported that in damaged skin (abraded, tape stripped, burned or UV exposed, etc), the SC hydrophilic–lipophilic gradient may also influence the penetration of particulate formulations applied topically (Nielsen, 2005; Nielsen et al., 2007). Additionally, the type of formulation in which agents are dispersed, and the application method will likely affect the absorption outcomes for any skin condition.

Results of dermal nanoparticle penetration studies differ widely, depending on the nanomaterial tested, host species, and condition of skin, among other factors. While some have concluded that the stratum corneum resists penetration, others have found nanoparticles capable of breaching this barrier. For example, it has been concluded that quantum dots can penetrate through the epidermis into the dermis, especially with

flexing of the skin or by way of hair follicles (Mortensen et al., 2008; Zhang and Monteiro-Riviere, 2008), whereby microscopy from these publications revealed that a considerable portion of the dose penetrated to the dermis. Silver is currently being utilized as an antimicrobial agent in many dermal applications and has been found to penetrate both intact and damaged skin (Larese et al., 2009; Samberg et al., 2010). Titanium dioxide, a common ingredient in sunscreens and cosmetics, is generally recognized as safe for dermal exposure. However, while most titanium dioxide studies involving healthy skin report an absence of penetration, this may not necessarily be the case with damaged skin (Senzui et al., 2010). Hydroxylated fullerenes are currently included in many cosmetic preparations with the intention of preventing oxidative damage to the skin due to aging and sun exposure. Unfortunately, there have also been reports of toxicity associated with exposure to fullerol and other similar carbon-based nanomaterials. For example, Xia et al. (2010) have recently reported that, depending on the vehicle composition, pristine fullerene nanoparticles can penetrate deeply into the stratum cornea in healthy skin, as tested both *in vitro* and *in vivo* (Xia et al., 2010). In another study, fullerol caused delayed cell death characteristic of apoptosis, including DNA damage in rodent and human glioma cells, which was determined to be caused in the absence of ROS (Isakovic et al., 2006). The dermal permeation capability or toxicity of fullerol, specifically, has not been assessed, although fullerene-based peptides were shown to penetrate intact skin, which was exaggerated with mechanical stress leading to infiltration into the dermis (Rouse et al., 2007).

1.2. Reactive oxygen species generation by nanoparticles

ROS is a collective term used for a group of highly reactive molecules which contain oxygen (e.g. H2O2, O2•-, HO•, ROO•). A large number of publications have arisen due to findings of ROS generation resulting from exposure to a variety of nanoparticle types (Brown et al., 1999; Hussain et al., 2006; Lipovsky et al., 2011; Nel et al., 2006; Rancan et al., 2002; Sayes et al., 2004; Wilson et al., 2002). It has also been established that this occurrence of ROS production may be as a result of nanoparticles interacting with cellular material and/or simply originating from the nanoparticles themselves (Kaewamatawong et al., 2005; Lin et al., 2006; Stone et al., 1998). However, the ability of a nanoparticle to induce such a biological response is dependent upon the type of nanoparticle, as results have shown that some types are more apt to generate ROS than others in the same system (Rallo et al., 2011; Xia et al., 2006). Several hypotheses have been proposed to explain the mechanism of action leading to the cellular state of oxidative stress caused by ROS generation. Relating to nanoparticle exposures, increased surface area, crystal structure, chemical composition, and altered surface chemistry are thought to play a large role (Berg et al., 2009; Jiang et al., 2008; Schins, 2002). Additionally, it is thought that reactions involving nanoparticles or dissolved nanoparticle components may also increase cellular oxidative stress due to inflammatory mediator recruitment, which act to produce ROS (Brunner et al., 2006; Xia et al., 2008). ROS generation within the cell can cause a shift in glutathione oxidation state, which is commonly utilized as a means to assess overall cellular redox status

(Pastore et al., 2003). Glutathione is an antioxidant that prevents damage to cellular components in the presence of ROS (Pompella et al., 2003).

This work is an effort to elucidate the inflammatory and immunological response mechanism potential in a dermal model exposed to both metal containing and carbon-based nanomaterials, while considering the influence of physicochemical characteristics of the nanoparticles. Changes in gene and protein expression are measured, as well as metabolic activity, ROS generation, and resulting DNA damage. Additionally, the role of the immune and inflammatory response pathway regulator, NF-κB, is investigated. These studies examining the toxicological effects stemming from nanoparticle exposure are examined utilizing an *in vitro* system to model human health effects.

1.3. Cellular signaling pathway modulation

As the toxicological response to nanoparticles on the cellular level is beginning to be investigated, knowledge of regulatory cellular signaling pathways involved after exposures are of particular interest. A careful review of the current literature reveals publications that focus on nanoparticle-invoked pathways whose main function falls into one or more of the following categories: inflammatory response, immune response, oxidative stress/anti-oxidative protection, DNA damage, apoptosis, and autophagy (refer to Table 1.1). Previous reports with nanoparticle exposures (and other treatments) suggest that not all of these responses are present in a given cell at one particular time or dosing concentration. For example, the cell may mount an antioxidant response to deal with the "insult" of the nanoparticle exposure by activating Nrf-2, a key transcription

factor involved in upregulating antioxidant genes, or the exposure may trigger more of an inflammatory response, in which NF-κB plays a role. A disturbance of the cellular redox equilibrium and subsequent oxidative stress has been shown to trigger multiple stress pathways and transcription factors of redox-sensitive nature, such as nuclear factor-erythroid 2-p45–related factor 2 (Nrf2), which activates expression of antioxidant genes, as well as nuclear translocalization of nuclear factor kappa B (NF-κB) and activator protein-1 (AP-1), which act to promote inflammatory mediator genes (Cho et al., 2006; Rahman et al., 2006).

It has also been shown that, following perturbation of one of these transcription factors or other important regulatory proteins, a DNA damage response pathway may be initiated, whereby p53 is a likely player. In other words, the type of exposure exerts influence over pathway selection. Figure 1.2 highlights these potential pathways that could be activated on the cellular level following nanoparticle exposure.

1.3.1. NF-κB (inflammatory response)

NF-κB has been implicated previously in nanoparticle exposures. NF-κB is a major transcription factor responsible for regulating genes of both the innate and adaptive immune response (Livolsi et al., 2001). NF-κB becomes activated through distinct signaling components: inactivated, cytosolic NF-κB is complexed with the inhibitory IκBα (NFKBIA) protein. A variety of intra- and extracellular signals, such as ROS, cytokines, UV irradiation, and growth factors, are recognized via integral

Table 1.1 Pathway-driven responses in biological systems exposed to nanoparticles.

Pathway Identified	Particle-Type	Genes or Proteins Modulated	System and Doses	Citation
NF-κB (p65)	ZnO, 24-70 nm	NF-κB, IL-8, p-p65, p-IκB	BEAS-2B cells, 2-8 μg/mL	(Wu et al., 2009)
MAPKs (ERK1/2)	CdSe/ZnS QD, 10.5 nm avg	TNF-α, CXCL8, p47phox, p-p38	PBMC, THP-1 cells (0.2-25 nM) and BALB/c mice (2 nmol/mouse)	(Lee et al., 2009)
NF-κB, AP-1, NRF-2 (all postulated)	6 combustion-derived NPs (UfCP, SootL, SootH, Ptx90, DEP, PtxG), 800-43 m^2/g SA	CSF2, CXCL1/5, IL-6, MT1/2, CYP1A1, NQO1, OGG1	BALB/cJ mice BAL and PMN (0.5-50 μg/μL)	(Stoeger et al., 2009)
MAPK (ERK), Nrf-2	Si, porous (5-15 nm) and fumed (7 nm), 349.71 and 644.44 m^3/g SA	SOD, HO-1	BEAS-2B cells, 1mg/L	(Eom and Choi, 2009b)
ERK, p-38, Nrf-2, JNK	CeO_2, (15, 30, and 45 nm)	Nrf-2, HO-1, p-38, JNK, SOD	BEAS-2B cells, 1mg/L	(Eom and Choi, 2009a)
HIF-1α	Tungsten carbide cobalt, 62 nm	SOX2, ID2, FOXO4 and others related to hypoxia response, carbohydrate metabolism, endocrine pathways, and targets of several transcription factors	HaCaT keratinocytes, 33 μg/mL	(Busch et al., 2010)
NF-κB	ZnO (<100 nm), CdS (10 nm)	NF- κB	IP15 (glomerular mesangial) and HK-2 (epithelial proximal) cell lines, 5 $\mu g/cm^2$	(Pujalté et al., 2011)
NF- κB	TiO_2, P25, 170 nm aggregated size	NF- κB, TLR4	NIH/3T3, 10 ng/mL	(Chen et al., 2011)
p53	Nickel ferrite	p53, survivin, bax/bcl-2 and casapase	A549, 25-100 μg/mL	(Ahamed et al., 2011)

Table 1.1 Cont.

Pathway Identified	Particle-Type	Genes or Proteins Modulated	System and Doses	Citation
Akt, ERK1/2	NPCB, 14 nm (Printex 90)	Akt, ERK1/2, GSK-3 fusion protein	RLE-6TN rat lung epithelial cells, 1-10 μg/cm^2	(Unfried et al., 2008)
EGF-R, MAPK	ufCB, 14 nm (Printex 90)	ERK1/2, JNK1/2, casp3, Phosphotyrosine	RLE-6TN rat lung epithelial cells, 1-10 μg/cm^2	(Sydlik et al., 2006)
Cell cycle, MAPK, Nrf-2, PI3K/AKT, glycolysis, and others	TiO_2, P25	SOD2, YWHA2, PRDX6, YWHAB,YWHAE,YWHA2, AMPK2 and GSK-3 α/β, and others	BEAS-2B, 10 μg/mL	(Ge et al., 2011)
NF- κB	Poly(acrylic acid)-coated gold, 5, 10, and 20 nm in the presence of fibrinogen	Mac-1 integrin receptor, NF-κB	THP-1, 10 μg/mL	(Deng et al., 2011)
NF- κB	CdSe/ZnS-COOH QD, 15 nm	NF- κB , TNF-α, IL-1B and IL-10, HMOX-1, IL-6	HDF, 30 and 60 nM	(Romoser et al., 2011b)
NF- κB, cAMP/PKA, HIF-1α, JNK, PKC/Ca^{++}, TGF-β/SMAD, ERK, cell cycle, C-myc, p53	Ag, Au, Pt, Al2O3, Fe3O4, SiO2, and ZnO with respective primary diameters of 13, 12, 13, 12, 8, 19, and 20 nm	NF- κB, CRE, HIF-1α, AP-1, NFAT, SMAD, SRF, E2F, MyC, p53	RAW 264.7 macrophages, 0.375-100 μg/mL	(Rallo et al., 2011)
P53, JNK	Ag (2 different sources compared), polydisperse particles 20 nm or less	Cyt c, Bax, Bcl-2, JNK, PARP, p53	NIH3T3 mouse fibroblasts, A10 rat vascular smooth muscle cells, and HCT116 human colon cancer cells, 50 and 100 μg/mL	(Hsina et al., 2008)

membrane receptors, which can lead to the activation of the enzyme IκB kinase (IKK or IKBKB).

The role of IKK is to phosphorylate the NF-κB-associated IκBα protein, resulting in ubiquitination and dissociation of IκBα from NF-κB. IκBα is degraded by the proteosome and the liberated NF-κB is then translocated into the nucleus where it binds to specific DNA motifs in promoters, termed response elements. It is capable of upregulating genes involved in immune cell development and maturation, as well as those dedicated to survival, inflammation, and lymphoproliferation (Zandi, 1997). Improper activation of NF-κB can lead to inflammatory diseases, whereas persistent suppression is known to cause depressed immune cell function and cell growth.

Wu et al. showed that, in human bronchial epithelial cells exposed to ZnO NPs, NF-κB is actually required for the upregulation of inflammatory marker IL-8. NF-κB was also found to be activated in response to CdSe/ZnS quantum dots (Romoser et al., 2011b), titanium dioxide (Chen et al., 2011), gold (Deng et al., 2011), combustion products (Stoeger et al., 2009), iron oxide, aluminum oxide, and silica dioxide (Pujalté et al., 2011), and ZnO in other works. ZnO, however, has been found to also downregulate NF-κB in macrophages (Rallo et al., 2011). This discrepancy may be partially explained by the time point levels that were checked, as the renal cell study probed for response at an earlier time point (1 hr).

1.3.2. Nrf2 (oxidative stress)

Nrf2, a basic leucine zipper-type transcription factor, is a member of the ‘‘cap ‘n’

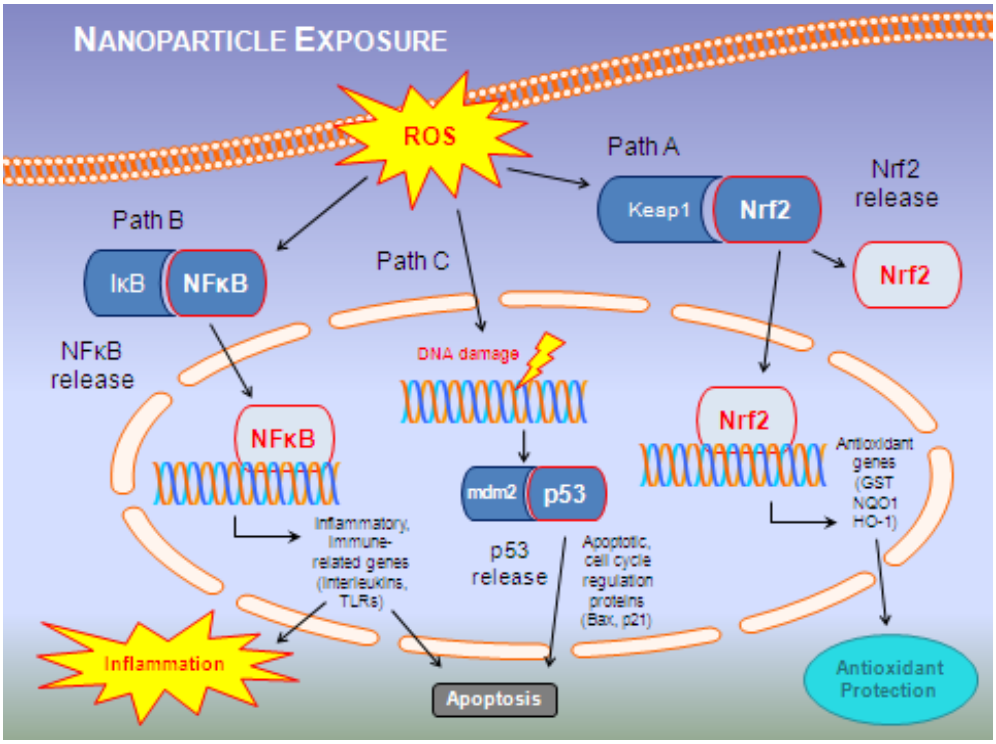

Fig. 1.2 Nanoparticle-induced pathway schematic. Several cell signaling pathways known to be triggered after exposure to ROS-generating nanoparticles are represented. Responding mechanisms may be inflammatory, genoprotective, or antioxidant in nature. The type and extent of reaction is system and nanomaterial-dependent.

collar'' family consisting of six members. Nrf2 is typically retained in an inactive cytosolic state via interaction with actin-binding Keap1, a protein that also mediates its degradation via the ubiquitin–proteasome pathway (Cullinan et al., 2004; Kobayashi, 2004). Nrf2 plays an important role in the cellular detoxification process by transactivating reporter genes linked to antioxidant response elements associated with phase II detoxifying genes (Kwong et al., 1999; Venugopal and Jaiswal, 1996; Venugopal and Jaiswal, 1998). Nrf2 also mediates the induction of detoxifying genes, NAD(P)H quinine oxidoreductase 1 and glutathione *S*-transferases (GSTs), by way of the antioxidant butylated hydoxyanisole (Itoh et al., 1997). Nrf2 regulates the expression of other detoxifying genes such as heme oxygenase 1 (HMOX1), superoxide dismutase 1 (SOD1), catalase, UDP-glucuronosyltransferase (UGT), and g-glutamylcysteine synthetasen (GCS) (Alam et al., 1999). This has been determined due to published data reporting lower expression of these genes in the Nrf2 knockout mice (Chan and Kan, 1999). Pro-oxidants activate Nrf2, which is likely due to oxidation of Keap1 and/or Nrf2 phosphorylation by kinases such as protein kinase C (PKC), Akt or PKR-like endoplasmic reticulum kinase (PERK) (Nguyen et al., 2004). The importance of Nrf2 in the cellular stress response is apparent in Nrf2 knockout mice, which develop severe autoimmune disease resembling systemic lupus erythematosus (Li et al., 2004). Furthermore, even young Nrf2-incompetent animals are highly susceptible to oxidative stress exerted by various chemicals, leading to pathological disorder susceptibility, including cancer (Itoh et al., 2004). While this work does not assess activation of Nrf2

directly, genes and proteins downstream of Nrf2, such as HMOX1 and SOD1 are investigated after nanoparticle exposures.

The published literature has recently begun to elucidate the importance of Nrf2 involvement with regard to nanoparticle exposures. Stoeger, et al. examined the effects of six different combustion-derived nanoparticles in mice and correlated their findings in a cell-free ascorbate *in vitro* system as a means to predict toxicity (Stoeger et al., 2009). They found that by utilizing surface area as a measure of exposure, their simple quantitative model based on oxidative potential, coupled with *Cyp1a1* induction capacity, was an appropriate indicator of inflammatory potential *in vivo*. Eom, et al. found in two different studies using human bronchial epithelial cells that Nrf2 translocated to the nucleus for activation of antioxidant genes, such as HMOX1 and Cu/Zn SOD. MAP kinase member, ERK, was involved in silica exposures, whereas phosphorylation of p38 occurred in CeO_2 exposures (Eom and Choi, 2009a; Eom and Choi, 2009b). Another recent study also found upregulation of catalase, SOD, and MAPK/ERK with exposures to 10 μM and 100 μM P25 TiO_2, also in bronchial epithelial cells (Ge et al., 2011).

1.3.3. DNA damage response

Many proteins are involved in maintaining the cellular genomic integrity. Although maintaining this integrity is essential to avoid cancer initiation, but limited DNA damage may be tolerated by the cell through a system of repair mechanisms. Should repair pathways fail, replication of damaged DNA may induce changes in the

genetic sequence inherited by the daughter cells. Inability to maintain the genomic material may lead to accumulation of DNA damage. Loss of genome integrity further leads to changes in gene expression, resulting from deletions or duplications. Several different repair pathways, equipped with precisely-tuned sensing mechanisms, are present in eukaryotic cells and specific to the type of damage that is present (Elvers, 2011).

Induction of DNA damage or replicative stress triggers a complex network of proteins known collectively as the DNA damage response (DDR). DNA damage is recognized by sensor proteins that recruit and activate transducer and effector or mediator proteins, inducing those which control cell cycle progression (Petrini and Stracker, 2003). This signaling cascade may induce cell cycle arrest to allow time for DNA repair or cell death via apoptotic mechanisms.

Upon DNA strand damage, ataxia telangiectasia and Rad3 related (ATR) is a protein kinase which recognizes ssDNA regions present after uncoupling of the replication fork formed by resection of DNA ends (Adams et al., 2006; Jazayeri et al., 2006; Zou and Elledge, 2003). Although ATR is typically associated with single strand breaks, ATM can activate ATR via phosphorylation of TopBP1 in response to DSBs as well (Elvers, 2011). ATM is recruited and activated by MRE11-RAD50-NBS1 (MRN) sensory complex (Lee and Paull, 2005), then acetylated by TIP60, stimulating its disassociation into active monomers (Bakkenist and Kastan, 2003; Sun et al., 2005). The checkpoint kinases CHK1 and CHK2 also play major roles in the signaling that occurs after DNA damage. CHK2 is constitutively expressed throughout the cell cycle and

activated as needed in response to DNA damage, whereas CHK1 is preferentially expressed during S and G2 phases, but is amplified in response to the presence of DNA damage (Kaneko et al., 1999; Lukas et al., 2001). ATM is known to primarily signal through CHK2 and ATR through CHK1 (Gatei et al., 2000).

ATM activation can lead to phosphorylation of H2AX as part of the DNA damage response, which serves to activate proteins involved in the cell cycle checkpoint control and halt cell cycle progression until the damage is repaired (Hanasoge and Ljungman, 2007). The phosphorylation signal on histone H2AX works as a platform for the recruitment of repair factors to the site of the break, as it is necessary for the recruitment of other factors to the sites of DNA damage (Paull et al., 2000). The presence of γ-H2AX, the active form of the histone, at the chromatin region nearest the site of the DSB, along with other proteins summoned by γ-H2AX, facilitates the activation of cell cycle checkpoints (Paull et al., 2000). The technique of analyzing differences in γ-H2AX levels after exposure to potential DNA damaging compounds is a well established procedure and is prevalent in the literature (Fernandez-Capetillo et al., 2002; Podhorecka et al., 2010; Stewart et al., 2003). Furthermore, others have reported activation of this histone variant after nanoparticle exposures, indicating the importance of the technique for assessing nanomaterial-driven genotoxicity (Bhabra et al., 2009; Mroz et al., 2008; Trouiller et al., 2009).

Both ATM and ATR may phosphorylate p53 (Cortez et al., 1999; Siliciano et al., 1997), thereby promoting nucleotide excision repair (NER) (Ford and Hanawalt, 1997). Additionally, p38-activated MK2 may directly phosphorylate CDC25B and C, inducing

cell cycle arrest (Manke et al., 2005; Reinhardt et al., 2007). However, p38 kinase may or may not phosphorylate p53 after exposure in response to UV stimulation (Bulavin et al., 1999; Reinhardt et al., 2007), which is likely dependent upon the cell type analyzed.

1.3.4. P38 and DNA damage

The p38 MAPK subfamily plays important roles in cytokine production and the stress response. Recent reports have also demonstrated additional functions for p38 MAPKs, for example, in the inhibition of cell cycle progression (Ambrosino and Nebreda, 2001; Reinhardt and Yaffe, 2009). p38 is activated by stimuli such as environmental or genotoxic stressors, transforming growth factor-β, and the inflammatory cytokines tumor necrosis factor and interleukin-1 (Wagner and Nebreda, 2009). Activation of p38 MAPK through environmental stress can mediate cell death (Wood et al., 2009). Activated p38 phosphorylates transcription factors important in the regulating cell growth and apoptosis, including cAMP response element-binding proteinhomologous protein/growth arrest DNA damage 153 (CHOP/GADD153) (Wang and Ron, 1996), and NF-kB (Korus et al., 2002; Ridley et al., 1997). p38 lies downstream of mitogen-activated protein kinase (MAPK)/ERK-kinases (MEKs): MAPK kinases-3, -6, and SAPK/ ERK-kinase-1. Using a quantitative microinjection approach, Molnar et al showed in 3T3-NIH fibroblasts that a GTPase, Cdc42H, can inhibit cell cycle progression at G1/S through a mechanism requiring activation of p38 (Molnar et al., 1997). In response to DNA damage stimuli that induce DSBs, activation of p38 MAPK can also lead to the induction of a G2/M cell cycle checkpoint through p53-

dependent and independent mechanisms (Bulavin et al., 2001; Mikhailov et al., 2005; She et al., 2001).

Trouiller et al reported that mice given TiO_2 nanoparticles in drinking water gave rise to γ-H2AX-positive cells at doses of 50-500 ppm, whereas micronuclei formed at the 500 ppm concentration (Trouiller et al., 2009). Another study using TiO_2 and ZnO in a dermal context found that their particles could catalyze oxidative DNA damage in cultured human fibroblasts (Dunford et al., 1997). Sharma et al also reported significant DNA damage utilizing the comet assay in primary human keratinocytes with 14 ppm ZnO (Sharma et al., 2011). Auffan et al found that, in human dermal fibroblasts, a concentration as low as 6 ppm could induce significant SSBs and cause formation of binucleate cells (Auffan et al., 2009b). Additionally, it has been shown recently that some nanoparticles can cause cell cycle arrest in response to DNA damage. For example, G1 arrest was observed in mouse lung epithelial cells exposed to C60 and SWCNT (Jacobsen et al., 2008), and carbon black coated with benzo(a)pyrene gave rise to S-phase arrest in human lung epithelial cells (Mroz et al., 2007). Additionally, AshaRani et al. reported that starch-coated silver NPs induced concentration-dependent G2/M phase arrest and DNA damage in human glioblastoma cells and fibroblasts (AshaRani et al., 2009). Silver NPs were also found to induce S and G2/M phase arrest in Jurkat T cells (Eom and Choi, 2010), but G1 arrest in RAW264.7 macrophages (Park et al., 2010) using similar concentrations of nanomaterials. Additionally, SiO_2 NPs induced G2/M arrest in human embryonic embryo cells (Wang et al., 2009). The goal of this research, as it relates to DNA damage, was to elucidate the DDR mechanism potential in a dermal

model exposed to three metal oxide nanomaterials, while considering the influence of physicochemical characteristics of the nanoparticles.

Lastly, nanoparticles may be amended to either improve functionality, to control location, or to protect the nanoparticle or surrounding biological system from potential damage (Gaihre et al., 2011; McShane and Ritter, 2010; McShane, 2002; McShane, 2006; Romoser et al., 2011a). Chapter 5 discusses the mitigation of quantum dot-induced toxicity in human dermal cells via quantum dot microencapsulation in an effort to accomplish these tasks.

1.4. Summary

Nanoparticles are currently in many commercially available products for dermal use. Since it has been shown that some nanoparticles are capable of penetrating dermal tissue, depending on a variety of factors, including, but not limited to the nanoparticle characteristics and condition of the skin, investigation into subsequent toxicity and methods to protect biological surroundings is warranted. Analysis of oxidant generation is important in nanoparticle exposure scenarios and when assessing the outcome of the cell, as production of ROS leads to oxidative stress, thereby initiating subsequent cellular pathways. Several major pathways have been implicated in nanoparticle exposure studies, including the Nrf2 antioxidant pathway, NF-κB inflammatory and immune response pathway, and DDR pathway. It has been reported that NF-κB is important, if not critical, in initiating inflammatory mediators and determining cell survival in response to the presence of nanoparticles. If DNA damage occurs with

nanoparticle exposures, it is typically concentration-dependent, but tends to be exacerbated by the decreased size of nanoparticles, compared to their larger-sized counterparts of identical composition. Therefore, very low concentrations of nanomaterials may cause damage. Deciphering cellular pathway-driven toxicity, while considering nanoparticle physicochemical characteristics and the impending oxidative stress potential, will assist in further defining the risks associated with nanoparticle usage.

CHAPTER II

QUANTUM DOTS TRIGGER IMMUNOMODULATION OF THE NF-κB PATHWAY IN HUMAN SKIN CELLS*

2.1 Introduction

Quantum dots (QDs) are crystalline semiconductors approximately 1-20 nm in diameter. QD nanocrystals composed of CdSe cores and ZnS shells have received attention due to their unique electronic and optoelectronic properties at nanoscale levels and their widespread applications (Azzazy et al., 2007; Delehanty et al., 2008; Hild et al., 2008; Jamieson et al., 2007; Li et al., 2007; Medintz et al., 2008; Michalet et al., 2005; Walling et al., 2009). Because of their unique characteristics, QDs are used at increasing rates for a wide variety of industrial and consumer-based applications, including biomedical imaging agents, inks, and solar panels (Alivisatos et al., 2005; Gao et al., 2004; Michalet et al., 2005; Roco, 2003). QDs may also pose risks to human health, where unintended exposure to nanomaterials may occur at the workplace or during end product use via inhalation, dermal absorption, or gastrointestinal tract absorption (Rzigalinski and Strobl, 2009). Dermal exposures to QD particles have shown toxicities due to heavy metal exposure and/or the production of reactive oxygen intermediates (ROIs) (Derfus et al., 2004; Kirchner et al., 2005b; Ryman-Rasmussen et al., 2007).

---

*Reprinted with permission from "Quantum dots trigger immunomodulation of the NFκB pathway in human skin cells" by Romoser, et al., 2011. *Molecular Immunology*, 48, 1349-1359, Copyright [2011] by Elsevier Ltd.

Due to the growing number of potential uses that are offered by QD materials, consumer handling and manufacturer exposure to QDs is likely to increase. Nanoscale materials are thought to impose increased adverse effects on organisms than microscale materials because of their finer sizes and corresponding larger specific surface areas per unit mass (Maynard and Kuempel, 2005; Monteiller et al., 2007; Oberdorster et al., 2005). However, it is largely unknown which specific pathways or subcellular mechanisms of action are triggered as a result of QD exposure. Many investigators have shown that QDs can be internalized into cells and others have speculated the route of entry for particular QDs (Duan and Nie, 2007; Jaiswal et al., 2003; Zhang and Monteiro-Riviere, 2009), but what are the mechanisms of injury and key participants on the molecular level in the cell and how do those processes develop? We hypothesized that immune mediators of inflammation may be initiated in the exposed cell layers.

In an attempt to fill this gap, human epithelial keratinocytes (HEK), found in the epidermis, and human dermal fibroblasts (HDF), located in the dermis, were utilized to query the molecular interactions with QDs. Dermal cells were chosen because contact with the skin is one of the routes of exposure to QDs. Zhang et al. (2008) and Mortensen et al. (2008) both concluded that QDs of similar or identical structure and composition to those used in this study could penetrate through the epidermis into the dermis, especially with flexing of the skin or by way of hair follicles (Mortensen et al., 2008; Zhang and Monteiro-Riviere, 2008). Microscopy from their publications revealed that a considerable portion of the dose penetrated to the dermis. These studies used concentrations which ranged from 1-2 μM. However, this manuscript focuses on the

nanomolar concentration range, yielding cellular viability between 15% and 100% in both HEK and HDF cells. A recent development in the nanotoxicology literature noted the importance of conducting *in vitro* experiments with a concentration range of nanoparticles that would not fully overwhelm the culture, as this would likely be inconsistent with equivalently-dosed *in vivo* studies (Oberdorster, 2010). Similarly, Zhang et al. (2006) found genetic perturbation in dermal cells exposed to 8 and 80 nM concentrations of silica-coated QDs (Zhang et al., 2006). From this range, we selected the lowest observable adverse effect level (LOAEL) concentrations of 30 and 60 nM to further investigate the mechanisms of cellular pathway stimulation by probing for adverse or protective responses in the fibroblasts. The human dermal fibroblast cell line was of interest partially due to its proximity to the vascular system and its importance in maintaining the structural framework of the tissue (Figure 2.1). Also, fibroblasts possess an elaborate cytokine response system, which allows these sentinels to initiate the process of inflammation (Le et al., 1987).

In an effort to increase current knowledge regarding pathways of the human cellular response to QDs, we have quantitatively investigated effects of an engineered QD on the expression of 50 unique genes in HDF cell cultures. In this study, we compared the dose-response and time-course effects of CdSe/ZnS-COOH QD nanoparticles in cells that induce or suppress one or more of the following effects: inflammation, immunoregulation, apoptosis, and cellular stress. Specifically, we found

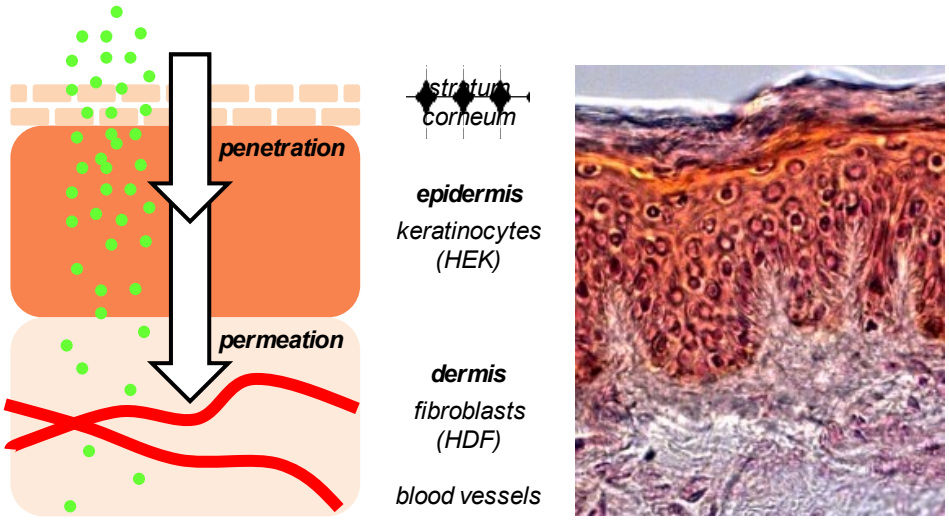

Fig. 2.1 Schematic representation of the experimental design. Infiltration through the stratum corneum allows penetration of the nanoparticles into the epidermis, which consists partially of keratinocytes. Further movement of QDs (green) into the dermis could occur, which houses dermal fibroblasts and increased vasculature (left). A porcine skin section is shown (right) as a representative comparison image, where 10 µm thick sections of skin removed from a 6 month old Yucatan Miniature Swine were H&E stained and imaged at 40X on a Zeiss AxioImager.Z1.

that many mRNA perturbations occurred in genes of the NF-κB pathway, which is involved in each of these processes. NF-κB is a major transcription factor responsible for regulating genes of both the innate and adaptive immune response (Livolsi et al., 2001). NF-κB becomes activated through distinct signaling components: Inactivated, cytosolic NF-κB is complexed with the inhibitory IκBα (NFKBIA) protein. A variety of extracellular signals can be stimulated via integral membrane receptors, which can then activate the enzyme IκB kinase (IKK or IKBKB). The role of IKK is to phosphorylate the NF-κB-associated IκBα protein, resulting in ubiquination and dissociation of IκBα from NF-κB. IκBα is degraded by the proteosome and the liberated NF-κB is then translocated into the nucleus where it binds to specific DNA motifs in promoters, termed response elements. Here, it can upregulate genes involved in immune cell development, maturation, and proliferation, as well as those dedicated to survival, inflammation, and lymphoproliferation (Zandi, 1997). Conversely, a suppression of nuclear NF-κB can result in TNFα-induced apoptosis (Antwerp et al., 1996; Beg and Baltimore, 1996; Liu et al., 1996; Wang et al., 1996). This decrease in nuclear translocation is due to increased levels of IκBα, which we found to be upregulated in our study.

Quantitative-PCR revealed both time and concentration dependent patterns of gene regulation. From our analyses of these data, we deduced that the particles used in this study influenced regulation of genes and proteins along the NF-κB pathway, as evidenced by deviations of relevant gene expression (*NFκB, IL-1B, IRAK1/2, CASP1*). Results from western blotting also revealed increased induction of inflammatory proteins

(HMOX-1, IL-1B, TNF-α) caused by stress, which is thought to arise from ROI and/or metal-induced toxicity in response to QD exposure.

To our knowledge, this work is the first to examine immune and inflammatory responses arising from QD exposure in dermal cells. Very few studies exist that have analyzed this type of cellular response to QDs. Hoshino et al. (2009) found that direct injections of QD/nucleotide complexes into the peritoneal cavity of mice resulted in inflammation with the infiltration of inflammatory cells (Hoshino et al., 2009). They also found that the same complex induced the production of both proinflammatory cytokines and chemokines. Rehberg et al. (2010) recently found that, depending on surface modification, QDs can modulate leukocyte adhesion and migration (Rehberg et al., 2010). Since such findings of cellular perturbation have been presented in the literature, further inquiry of the mechanisms of gene induction or suppression is necessary.

2.2 Methods

2.2.1. Quantum dot nanocrystal characterization

CdSe/ZnS-COOH crystalline quantum dots were purchased from Ocean Nanotech, LLC (Springdale, Arkansas). Characterization data is summarized in Table 2.1. Particle size and zeta potential were characterized in-house via Malvern ZetaSizer Nano ZS (Malvern Corp., Worchestershire, UK). Particle characterization was performed on the particles while in Milli-Q ultrapure water. Chemical composition was determined via inductively couple plasma-mass spectroscopy (Elan DRC II, Perkin Elmer SCIEX); no metal impurities were detected. Particle surface area was calculated

Table 2.1 Quantum dot particle characterization.

Property	**CdSe/ZnS-COOH**
Size (nm)	14.83 ± 0.07
Zeta potential (mV)	-54.00 ± 4.08
Surface area (nm^2)	690.93
Cd^{2+} ions/QD	562
Morphology	Crystalline
E_x/E_m (nm)	380/545

using the formula $SA=\pi d^2$ and total cadmium content was calculated from the formula utilizing the measured particle size, as follows:

$$\#\text{cadmium ions/QD} = \frac{vol\ sphere}{vol\ 1\ CdSe\ crystal} x\ 4 = \frac{\frac{4}{3}\pi r^3}{2.214 \times 10^{-28}} x\ 4 = 561.05$$

The QD samples were diluted into cell culture media, resulting in 1.25 µM stock solution, immediately prior to cell culture inoculation. A final 60 nM concentration contained 6.4×10^{16} QDs/mL. Suspensions were mixed thoroughly and added to cell cultures as described below.

2.2.2. Cell culture and experimental dosing

Human epidermal keratinocytes (CRL-2404, ATCC, Manassas, VA) were cultured in serum-free keratinocyte medium supplemented with 25 µg/mL bovine pituitary extract and 0.15 ng/mL recombinant epidermal growth factor. Human dermal fibroblasts (PCS-201-010, ATCC, Manassas, VA) were cultured in Dulbecco's Modified Eagle's Medium supplemented with 8% FBS (Gibco, Austria). HDFs were supplemented with an antibiotic cocktail consisting of penicillin, streptomycin, and amphotericin (Sigma-Aldrich, St. Louis, MO). HEKs were supplemented with streptomycin only. Incubation took place at 37°C with humidity and 5% CO_2. Cells were grown to 80% confluency in 6-well plates, then exposed to CdSe/ZnS-COOH quantum dots (Ocean Nanotech, LLC, AR) (30 nM and 60 nM final exposure concentrations) or held for a negative control. Each experiment was performed in triplicate.

2.2.3. Cell viability

HEK and HDF cells were cultured in 24-well plates as previously described, then exposed to QDs to give final well concentrations of 1, 30, 60, 90, and 120 nM. Cells were washed in plates treated for 8 and 48 hrs, and then phenol red-free media was added to wells. A resazurin dye (Sigma-Aldrich) was applied to cells (10% v/v final concentration) and mixed thoroughly on a rocker for 1 min. Plates were returned to the incubator for 2-1/2 hrs, then fluorescence was measured with a fluorescence plate reader (BioTek Synergy MX, Winooski, VT) using 560/590 nm excitation and emission wavelengths. Spectral compatibility data is presented in the appendix (Figure A-3); there was no interaction with the viability marker. Experiments were done in triplicate. A student's t-test was employed to calculate significant change in metabolic activity, as compared to the undosed control.

2.2.4. Fluorescence and brightfield microscopy

HEK and HDF cells were cultured and exposed to identically to the viability experiments. Washed cells were then covered with phenol red-free media and imaged at a total magnification of 100X (HDF) and 200X (HEK) with an Olympus IX71 inverted fluorescence microscope (Center Valley, PA). Images were processed with Olympus CellSens software.

2.2.5. Gene expression analysis

Cells were harvested at each QD concentration at time points of 8 and 48 hours.

An RNeasy® Mini Kit (Qiagen, Frederick, MD) was used in conjunction with an on-column genomic DNA digestion to lyse cells and extract total RNA. Thereafter, total RNA was prepared for a pathway-focused gene expression profiling PCR array system, specific for 84 genes of innate and adaptive immune responses (RT^2 Profiler™, SABiosciences, Frederick, MD), of which data from 50 passed quality control and are discussed here. An RT^2 First Strand Kit (C-03) from SABiosciences was utilized prior to qualitative real-time PCR (RT-PCR) to reverse transcribe messenger RNA into cDNA. After adding the cDNA to a mixture containing SYBR green, 25 µL of sample was loaded into all wells of 96-well plates pre-filled with primer sets including housekeeping genes, gDNA controls, reverse transcription controls, and positive PCR controls. Using a Roche LightCycler® 480 (Roche, Indianapolis, IN) for RT-PCR, a two-step thermal cycling program was followed: 1 cycle at 95°C for 10 min, then 45 cycles of 95°C for 15 s, then 60°C for 1 min. The Roche LightCycler® 480 software was utilized for raw data acquisition and calculation of C_t (threshold cycle) values.

2.2.6. Protein expression alteration

HDF cells cultured in the same conditions as above were washed in ice cold 1X PBS, then protease inhibitor cocktail (Sigma-Aldrich) and high salt lysis buffer were added to wells. Protein was isolated by collecting supernatant via centrifugation. Fractionated NF-κB samples were harvested without the use of lysis buffer. An NF-κB activation assay kit (FIVEphoton Biochemicals, San Diego, CA) was utilized to obtain nuclear and cytosolic NF-κB fractions from cells. Samples were loaded into 10 or 12%

SDS-PAGE gels, depending on protein of interest, and run at 120 mV. Gels were transferred to PVDF membranes, which were blocked in 5% milk/PBST and incubated in different primary antibody solutions overnight: HMOX-1, mouse, 1:400 (Santa Cruz Biotechnology, Santa Cruz, CA), IL-10, rabbit, 1:500 (Abcam Inc., Cambridge, MA), TNF-α, goat, 1:200 (Santa Cruz), IL-1B, mouse, (Abcam), or p65 NF-κB, rabbit, 1:1500 (Santa Cruz). Membranes were washed in PBST several times before secondary antibody (Goat, anti-mouse or anti-rabbit, or donkey, anti-goat 1:5,000, Santa Cruz) prepared in fresh 5% milk/PBST solution was added. Membranes were incubated in the secondary antibody at room temperature, then washed again in PBST. Immobilon™ Western Chemiluminescent HRP substrate (Millipore, Billerica, MA) was added to membranes and film exposures were taken. β-actin, 1:10,000 (Sigma) and lamin A/C 1:5,000 (Santa Cruz) were used as loading controls.

2.2.7. NF-κB transcriptional activity

A luciferase gene reporter assay was used to determine the state of NF-κB transcriptional activity in HDF cells exposed to QDs, as well as unexposed cells. Briefly, plasmid vectors containing either an NF-κB response element and a firefly luciferase gene or a *Renilla* luciferase control sequence (Promega, Madison, WI.) were amplified in competent cells, followed by plasmid DNA purification in endotoxin-free miniprep spin columns (Zymo Research Corp., Irvine, CA). Cells were seeded in triplicate wells 24 hrs prior to transfection in DMEM supplemented with 10% FBS and allowed to reach 80% confluency. Transfection of HDF cells was accomplished with Fugene HD

Transfection Reagent (Promega) in Opti-MEM media (Gibco, Austria) without serum, antibiotics, or phenol-red. Transfected cells were then exposed to 30 and 60 nM QDs for 8 or 48 hours. Wells of unexposed transfected and untransfected cells were included for comparison, as well as transfected cells treated with positive control, TNFα (20ng/mL). The Dual-Glo Luciferase Assay System (Promega) was utilized to separately measure luminescence of the NF-κB sequence-containing DNA and the normalization *Renilla* control vector in a Packard LumiCount luminometer. Background values from wells containing untransfected cells were subtracted from all measurements. Relative ratios for each well were calculated by dividing the ratio of unexposed well firefly luminescence/*Renilla* luminescence by the ratio of exposed well firefly luminescence/*Renilla* luminescence. The resultant data was graphed as a function of relative luminescence and length and type of exposure. A Student's t-test was utilized to determine significance of results at the $p<0.05$ level.

2.2.8. Calculations of gene expression changes

A total of five housekeeping (potential reference) genes were assayed on the plate and included those encoding β_2-microglobulin, hypoxanthine phosphoribosyltransferase 1, ribosomal protein L13a, glyceraldehyde-3-phosphate dehydrogenase, and β-actin. Analytical estimation of internal control gene stability indicated that the ribosomal protein gene (*RPL13A*) was most stable (*M* value = 0.013), and RPL13A was utilized for subsequent normalization (Vandesompele et al., 2002).

Changes in gene expression were estimated using the $2^{-\Delta\Delta Ct}$ method (Huang et al., 2010; Livak and Schmittgen, 2001), with *RPL13A* utilized as the stable reference gene for all experimental situations. The fold changes in gene expression were calculated with respect to the expression level of the genes in the respective control group. For example, 2-fold change of gene A indicates that expression of gene A was twice as large in the treatment group compared to its expression in the control group, while 0.5-fold change of gene A indicates that the expression of that gene was two times less in the treatment group compared to its expression in the control group. More detailed gene annotations, array layout, and gene tables regarding the array are available at http://www.sabiosciences.com/genetable.php?pcatn=PAHS-065A. Information regarding the manufacturer's estimates for array performance, sensitivity, specificity, and reproducibility are available at http://www.sabiosciences.com/rt_pcr_product/HTML/PAHS-052A.html#accessory.

2.3 Results

2.3.1. Cellular morphology

HDF and HEK cells were exposed to a range of CdSe/ZnS QDs from 1 nM to 120 nM for 8 and 48hrs (Figure 2.2). Phase and fluorescence images revealed an internal accumulation of QDs, which increased with both time and concentration. As a result of these exposures, HEK cell density decreased more severely than HDF cell density (Figures 2.3-2.4). The decreasing number of HEK cells corresponds to the amount of detectable fluorescence at the plane of the cells. Few detectable morphological changes

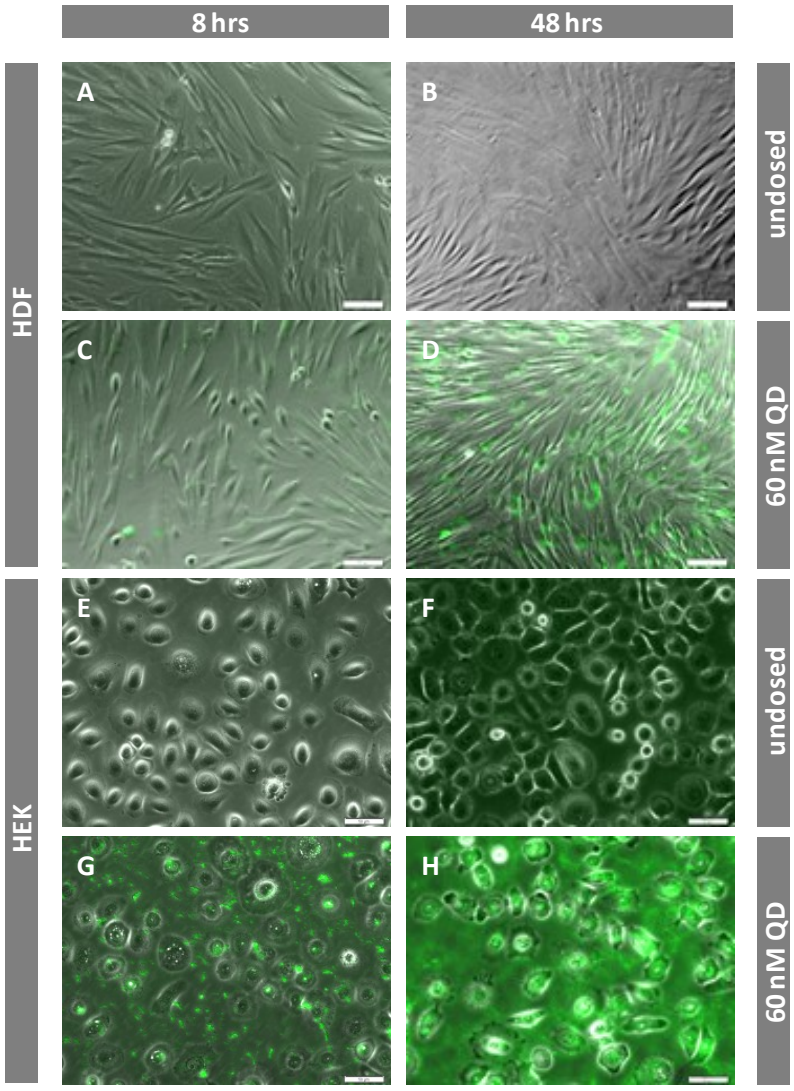

Fig. 2.2. Cellular morphology and QD uptake. Cellular morphology and intracellular QD fluorescence in HDF and HEK after exposure to 60 nM CdSe/ZnS QDs at 8 and 48 hrs. HDF (A-D) and HEK (E-H) cells were imaged at 8 hrs (left side) and 48 hrs (right side) and either treated with 60nM QDs (C,D,G,H) or left undosed (A,B,E,F).

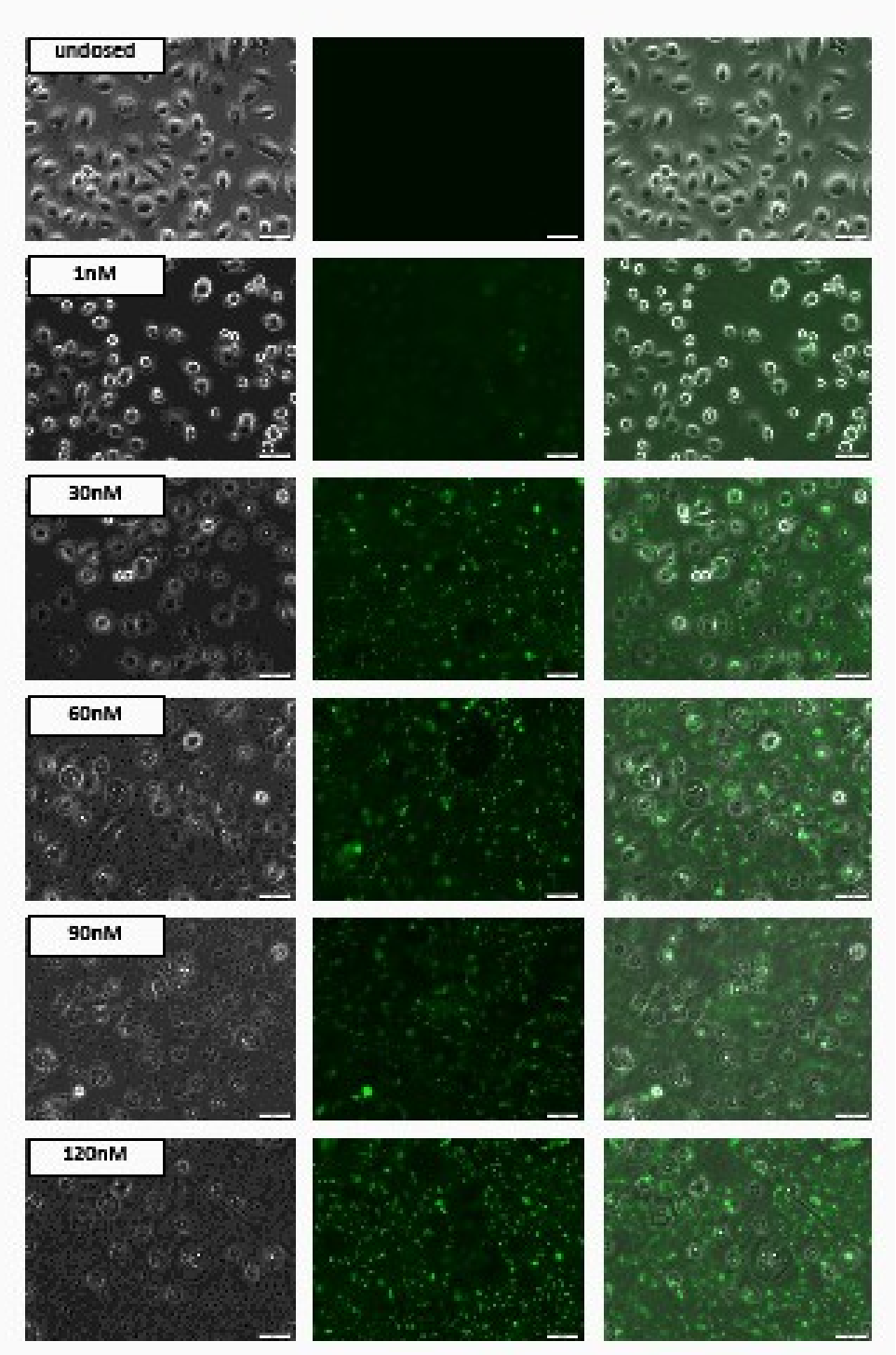

Figure 2.3. HEK morphology at 8 hrs exposure. Cellular morphology and intracellular QD fluorescence after exposure to HEK cells 8 hrs. Scale bar=50µm.

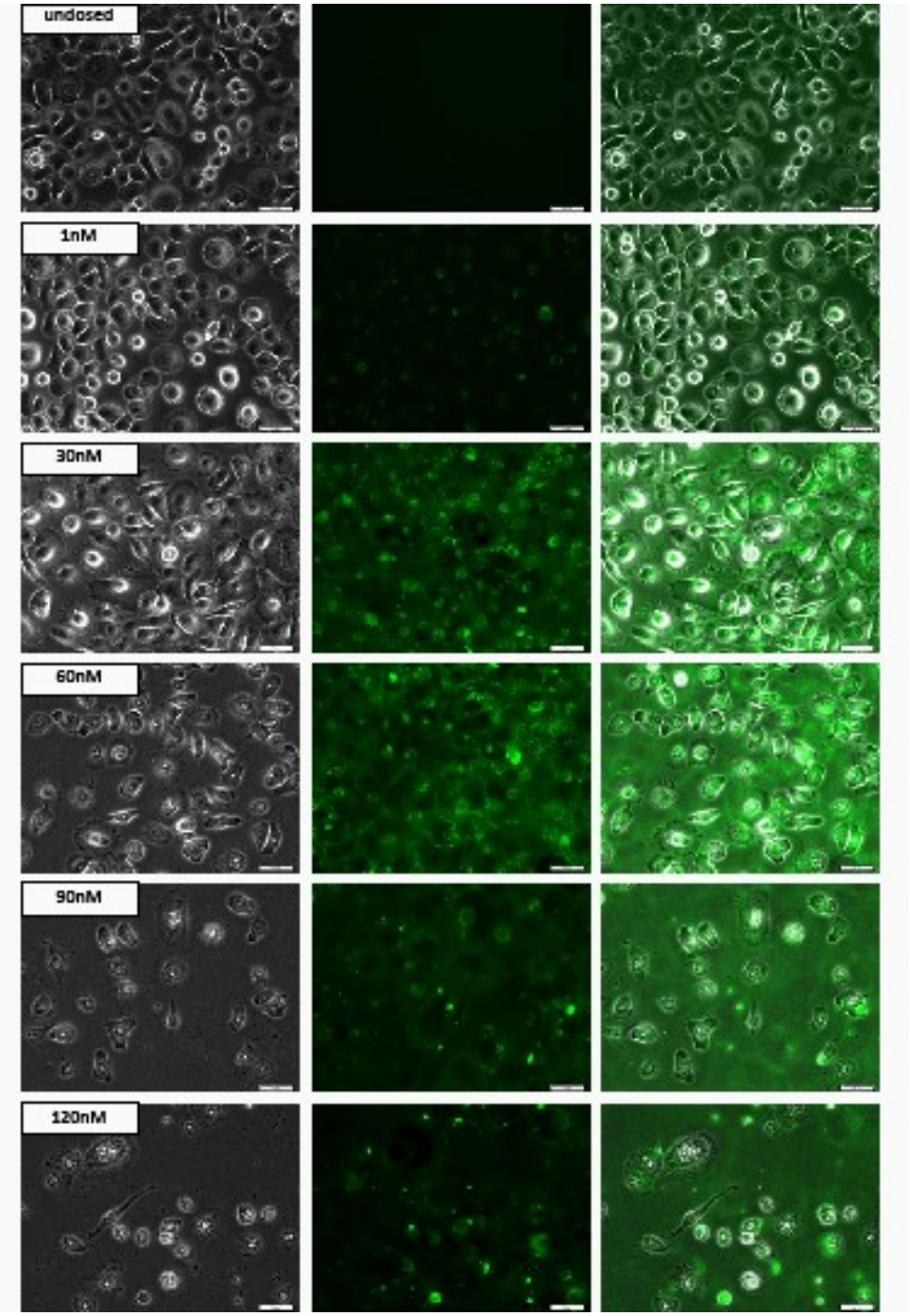

Figure 2.4. HEK morphology at 48 hrs exposure. Cellular morphology and intracellular QD fluorescence after exposure to HEK cells 8 hrs. Scale bar=50µm.

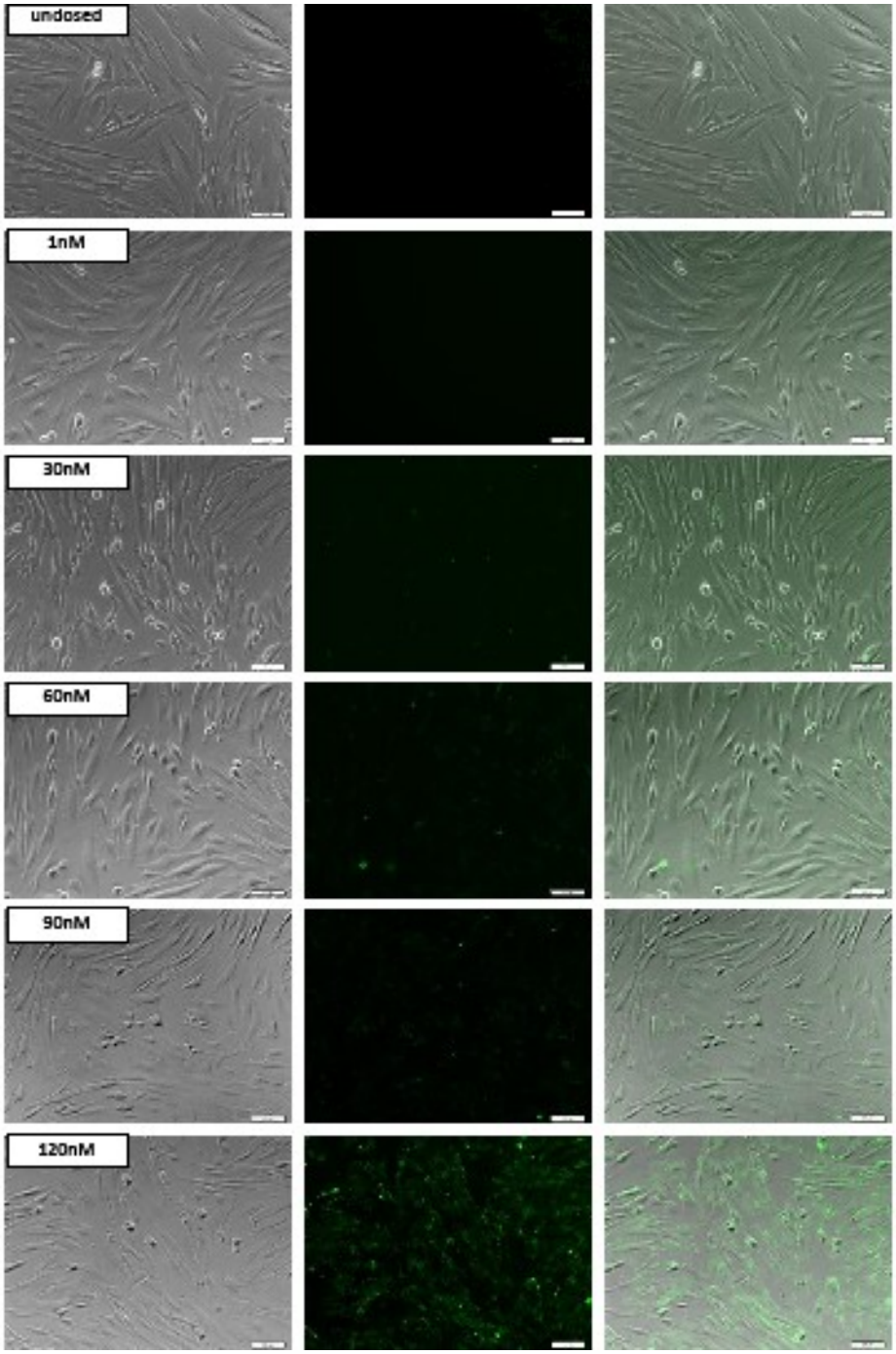

Figure 2.5. HDF morphology at 8 hrs exposure. Cellular morphology and intracellular QD fluorescence after exposure to HDF cells 8 hrs. Scale bar=100μm.

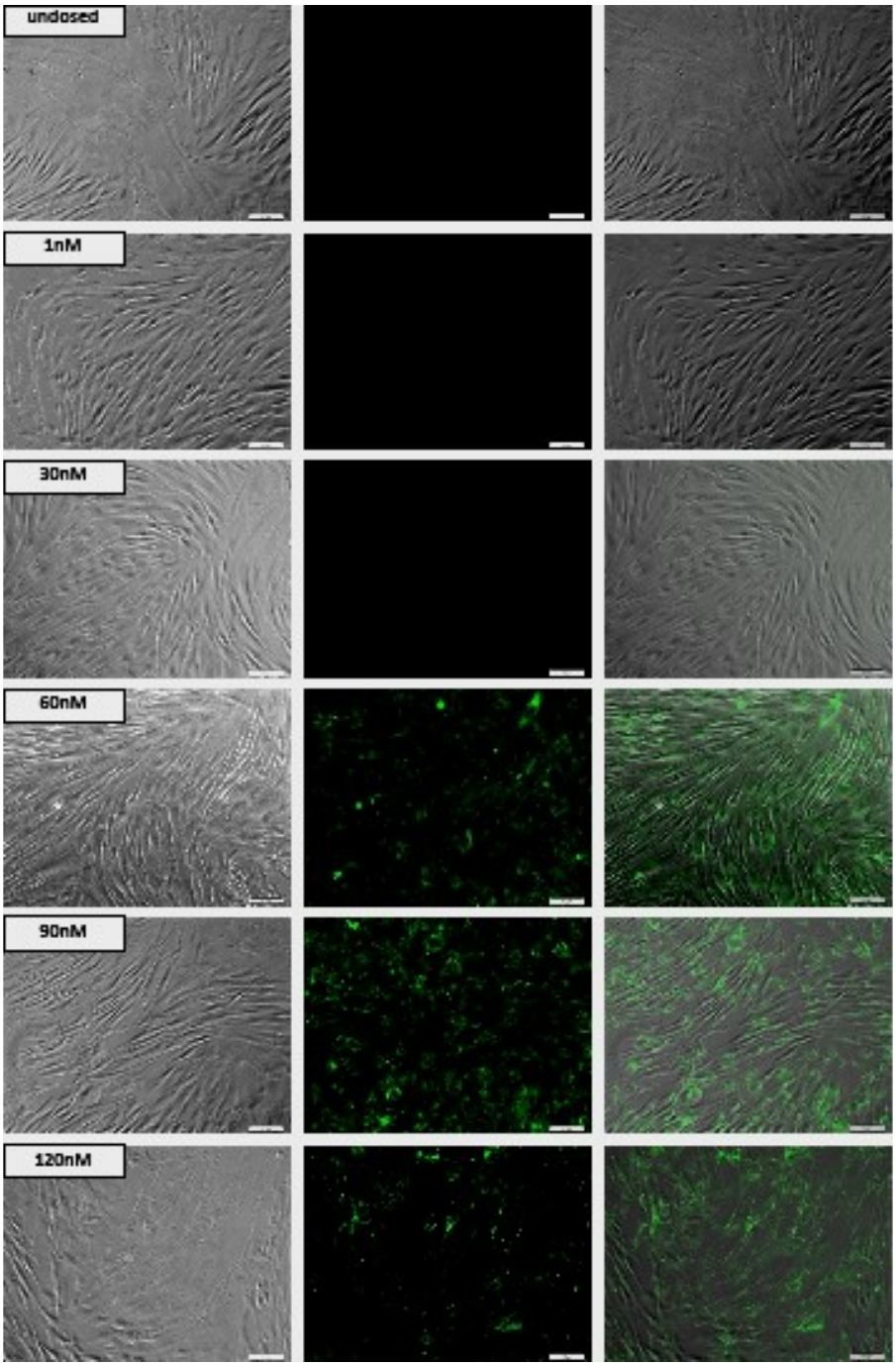

Figure 2.6. HDF morphology at 48 hrs exposure. Cellular morphology and intracellular QD fluorescence after exposure to HDF cells 48 hrs. Scale bar=100µm.

occurred in the HDF cells, which remained adhered through the 48 hr time point (Figures 2.5-2.6). The 120 nM concentration at 48 hrs did produce fluorescence images elucidating some deterioration in the HDF morphology, which suggests that 120 nM is no longer within the tolerable exposure concentration range.

2.3.2. Cellular viability

As a measure of cellular viability, changes in metabolic activity were measured in HDF and HEK cells exposed to a range of QD concentrations from 1 nM to 120 nM. These responses were compared to those of undosed cells (Figure 2.7). Results indicated a differential response between the two cell types, suggesting that the fibroblasts were less susceptible to death in these experiments. A strong dose-response relationship was found in both cell types, with HEKs and HDFs decreased to 66.5% and 90.0% viability at the highest QD exposure concentration at 8 hrs, respectively. By 48 hrs, viability was decreased to 12.6% and 57.1%, showing a consistent differential between cell types. These findings corroborate our cellular morphology microscopy data (Figure 2.2-2.6). There were no interactions between the QD particles and the viability marker (Appendix Figure A-3).

2.3.3. Gene expression alterations often involve the NFκB pathway

Gene expression changes in HDF cells were assayed after treatment with CdSe/ZnS-COOH QDs at exposure concentrations of 30 nM or 60 nM and at 8 or 48 hours after initial exposure. Figure 2.8 employs a heat map to summarize 50 genes with

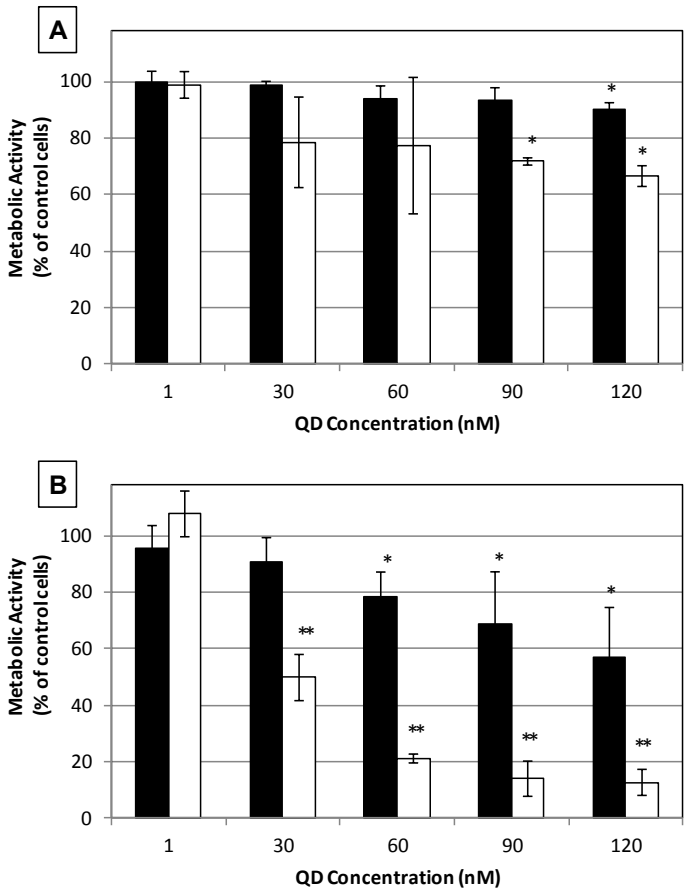

Fig. 2.7. Metabolic activity of HDF and HEK cells dosed with QDs. Metabolic activity of HDF (black) and HEK (white) cells dosed with QD over dose-response at (A) 8 hrs and (B) 48 hrs exposure time points. *p-val<0.05; **p-val<0.001.

8 hrs			48 hrs	
30 nM	60 nM		30 nM	60 nM
4.5315355	7.061624	***ADORA2A***	1.2141949	1.4439292
1.0792282	0.9075192	***C5***	0.8010699	0.8066418
0.8705506	1.2141949	***CASP1***	1.2570134	1.6817928
0.9265881	0.8705506	***CASP4***	0.9395227	1.2226403
4.0278222	6.6807034	***CCL2***	1.1328839	1.5691682
0.5904963	0.3609823	***CCR3***	0.8766057	1.0792282
0.2002675	0.5823668	***CD14***	1.0942937	0.6029039
0.8526349	0.9012505	***CD55***	1.3947437	1.6245048
0.8645372	0.8766057	***CHUK***	1.057018	1.4742692
0.8888427	0.6328783	***COLEC12***	0.4665165	0.5823668
0.9460576	0.9201877	***FN1***	1.1328839	1.0497167
0.0406669	0.0493776	***HMOX1***	1.6021398	2.3133764
0.0412346	0.231647	***IFNA1***	2.3294672	0.882703
0.5509526	1.3851095	***IFNB1***	2.1734697	1.9453099
1.1250585	1.3195079	***IFNGR1***	1.057018	1.0069556
1.3755418	1.4339552	***IFNGR2***	1.1250585	1.0424658
1.1728349	1.1728349	***IKBKB***	1.5157166	1.1328839
0.1842837	0.1258694	***IL10***	1.6701758	1.6934906
1.1892071	1.5583292	***IL1A***	2.4116157	0.4537596
7.621104	12.996038	***IL1B***	2.0139111	2.1885874
0.9012505	1.1407637	***IL1F7***	2.1435469	1.1728349
0.6973718	0.6783022	***IL1R1***	0.7474246	0.7791646
0.8888427	0.8585654	***IL1RAP***	1.2058078	0.9592641
0.2570285	0.2932087	***IL1RL2***	0.6070974	0.2932087
7.1602006	11.794154	***IL6***	2.0420243	2.1584565
1.2141949	0.9592641	***IRAK1***	0.7955365	0.8950251
2.8481004	4.2574807	***IRAK2***	1.0792282	1.9185282
1.5691682	1.6358041	***IRF1***	1.1328839	1.0210121
0.8645372	0.7845841	***LY96***	1.0069556	1.6586391
0.9395227	0.8645372	***MAPK14***	0.8766057	0.823591
1.1407637	1.1407637	***MAPK8***	1.2745606	1.2226403
1.0069556	0.9794203	***MIF***	1.0352649	1.4845236
1.2311444	1.3472336	***MYD88***	0.8467453	0.8010699
1.9318727	2.2191389	***NFκB1***	1.0497167	1.5052467
0.7526234	0.6877709	***NFκB2***	0.933033	0.6372803
2.2038102	2.6573716	***NFκBIA***	1.1407637	1.3660403
1.0424658	0.9930925	***NLRC4***	1.3013419	1.905276
1.7052698	0.7071068	***PGLYRP1***	1.3947437	0.9794203
2.1885874	2.9485384	***SERPINA1***	0.8293195	1.2570134
0.9201877	0.9138315	***SERPINE1***	1.0792282	1.0942937
0.9862327	0.5396141	***SFTPD***	0.6925547	0.7684376
0.9265881	0.882703	***TGFB1***	1	0.8179021
1.0139595	1.8531761	***TLR2***	0.8766057	1.4640857
0.9726549	1.3566043	***TLR3***	0.7631296	0.659754
0.6783022	0.7169776	***TLR4***	0.7737825	1.0867349
0.8888427	0.6736168	***TLR6***	0.6830201	0.6461764
0.5509526	1.1407637	***TNF***	1.591073	0.2812646
0.9460576	0.933033	***TNFRSF1A***	1.1647336	1.5800826
0.952638	1.0497167	***TOLLIP***	1.1892071	1.3851095
0.9460576	0.8122524	***TRAF6***	1.0497167	0.9930925

Fig. 2.8. Gene expression heat map. Heat map of pathway-specific gene expression changes in HDF. Central column shows genes in bold, columns to the left and right show fold change in expression levels in response to the treatment (labeled at top), compared to untreated controls assessed at the same time point. Fold suppressions of <0.5 are colored dark green and 0.5-0.8 light green. Fold inductions of 1.2-2.0 are pink and >2.0 red.

complete data for all of the samples (two experimental and one negative control for each time point). Fold upregulation or downregulation of mRNA levels is shown compared to that of untreated control cells, all normalized to the selected most stable housekeeping gene of the five analyzed, RPL13A. Scatter plots call attention to a smaller dataset that exceeded thresholds of 2-fold induction or 0.5-fold suppression shown individually for each experimental condition (Figure 2.9). Database curation information for all genes attempted in this study is included in Appendix Table A-1, along with a key that defines the four queried toxicological responses in which each gene is involved. Many of the genes have functions along several intertwined pathways. *IKBKB*, which spurs the release of NF-κB from the cytosol, is one such example, as it can be categorized as relating to oxidative stress, inflammatory response, and/or non-inflammatory immune response.

Since this can be one of the difficulties in assessing gene profiles, we chose a focused pathway array and searched for common relationships and downstream actions of these genes that were affected, finding that many genes modulated by QD treatments were linked to the NF-κB pathway. Specific results follow.

2.3.3.1. Inflammatory response

Inflammation is a sophisticated immune and homeostatic response by vascular tissue to irritants and damaged cells as well as pathogens. Many genes in the array tested for mediators of inflammation, and the expression of many genes was considerably altered in these exposures, including NF-κB pathway modulation. Transcripts regulating

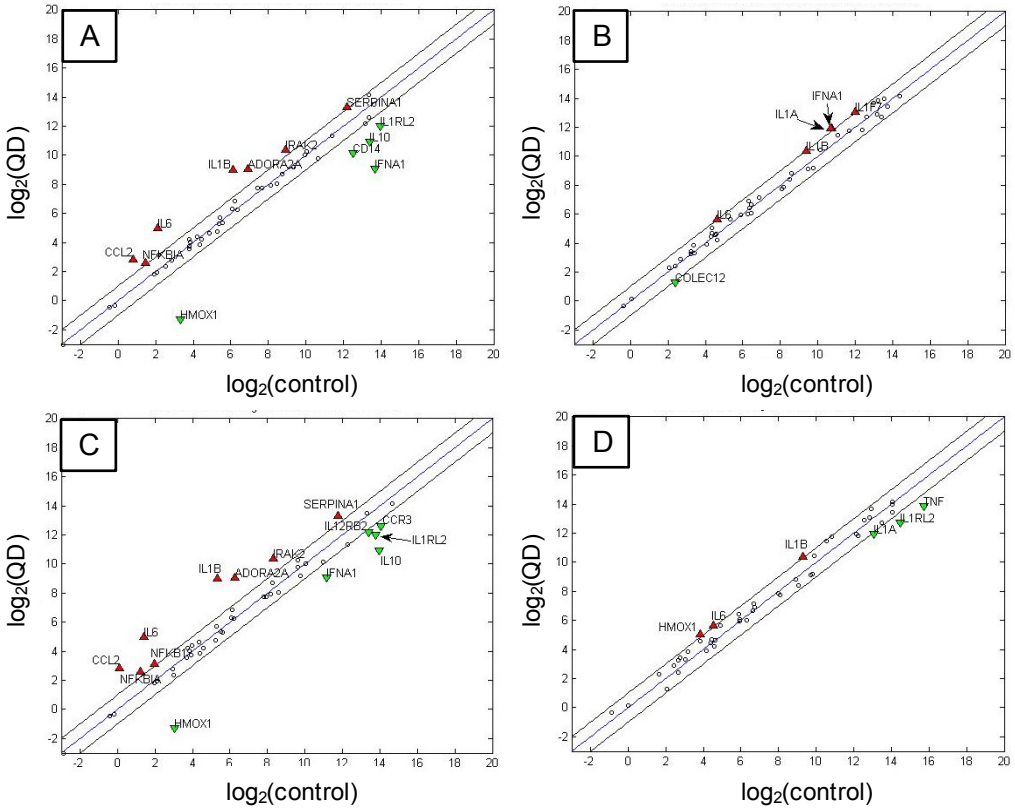

Fig. 2.9. Modulated gene scatterplots. Comparison of up and downregulated genes in HDF cells: (A) 30 nM QD-exposed cells vs. unexposed cells at 8 hrs exposure, (B) 30 nM QD-exposed cells vs. unexposed cells at 48 hrs exposure, (C) 60 nM QD-exposed cells vs. unexposed cells at 8 hrs exposure, and (D) 60 nM QD-exposed cells vs. unexposed cells at 48 hrs exposure. Red triangles indicate genes that were upregulated by at least 2.0-fold, green triangles represent genes downregulated at least 0.5-fold compared to the control.

inflammation produced a complex profile of induction and repression and were detected at the two day time point with QD exposure. Members of the *IL-1* and *IFNγ* families, as well as *CCR3*, *TLR4*, *TLR6*, *TNFα*, *IL-6*, and *IL-10* were all modulated in response to QDs. It is important to note that while pro-inflammatory *IL-6* was strongly upregulated early in the response at 8 hrs (11.94-fold with 60 nM), anti-inflammatory *IL-10* was simultaneously downregulated (0.13-fold with 60 nM).

2.3.3.2. Non-inflammatory immune response

This study extended to the regulation of innate immune genes not overtly involved with inflammation and mediators of adaptive immunity. Several genes perturbed in these experiments dictate that pattern recognition receptors are activating antigen presenting capabilities to be able to trigger T cell mediated immunity. These genes pleiotropically contribute to multiple physiological pathways, often via the NF-κB pathway and hint that inflammation is not the only effect QDs have on biological systems. A serine protease inhibitor (*SERPINA1*), which was upregulated nearly 3-fold at the 8 hr timepoint, and innate pattern recognition receptors, such as members of the collectin and *PGLYRP* families, showed that diverse responses were being initiated by the QDs. Message levels of *IFNA1* were transiently downregulated at 8 hrs in response to QD treatment, then later upregulated at 48 hrs. CD14 (along with TLR4) is a component of the classic LPS receptor. Its suppression by the lower concentration of QDs is particularly curious, suggesting unheralded physiology of this receptor for recognition of moieties other than conserved patterns in prokaryotic cell walls.

2.3.3.3. Apoptotic response

Mediators of the programmed cell death pathway were assayed to determine their level of induction or suppression in response to nanoparticle treatment. The gene for the adenosine receptor (*ADORA2A*) has been implicated in programmed cell death (Trincavelli et al., 2003) and was upregulated by CdSe/ZnS-COOH QDs. Tumor necrosis factor binds its receptor ligand to initiate the extrinsic apoptotic pathway. Upregulation (1.58-fold) of *TNFRSF1A* implicate this apoptotic pathway as a common result of exposure. Tumor necrosis factor receptor superfamily member 1A (CD120a) is a receptor for TNF-α. *NLRC4, CASP1,* and *CASP4* modulation suggest that apoptosis was induced at the 48 hr time point. The NLR family CARD (caspase recruitment domain) containing protein 4 (*NLRC4*) has been shown to interact with caspase 1 and *NOS2* (Damiano et al., 2004). NF-κB is necessary for the transcription of many key mediators in these apoptotic pathways (Graham and Gibson, 2005) and, although cytosolic levels of *NFKB1* mRNA were perturbed, message levels of *NFKB2* were down at both 8 and 48 hrs and inhibitory *NFKBIA* was up at both 8 and 48 hrs.

2.3.3.4. Stress caused by reactive oxygen intermediates and/or metals

Our results suggest that nanoparticle exposure may perturb the cytosolic reducing environment of exposed cells, causing toxic effects from macromolecular damage dealt by peroxides and free radicals. Heme oxygenase-1 is an essential enzyme in heme catabolism and protects against oxidative stress (Yachie et al., 1999). CdSe/ZnS-COOH QDs in low and high concentrations downregulated *HMOX1* mRNA expression at 8 hrs

(0.04-fold), but it was induced at 48 hrs (up to 2.3-fold), presumably to provide protection from oxidative stress. Analysis of other genes such as *IKBKB* (up 1.5-fold at 48 hrs) and nuclear factor κB p100 subunit, *NFκB2*, (downregulated 0.6-0.7-fold) also point to stress caused by QD treatment.

2.3.4. Protein expression alterations in the NF-κB pathway

While the changes in the mRNA levels are indicative of the activation of this pathway, additional evidence at the protein level strengthens support for such a hypothesis. Induction of various proteins involving oxidative stress, inflammatory response, apoptosis, and immunoregulation in HDF was assayed after treatment with QDs at exposure concentrations of 30 nM or 60 nM and at 8 or 48 hrs after initial exposure. Figure 2.10 displays the results acquired from western blotting. Induction of oxidative stress protein HMOX-1, inflammatory and apoptotic protein TNF-α, and inflammatory promoters and regulators IL-1B and IL-10 are shown after exposure to QDs at 8 and 48 hours. NF-κB subunit RelA protein analysis of total cell lysates revealed a decrease in expression in response to treatments, corroborating the modulation seen in NF-κB message after QD treatment. All protein expression data is compared to that of untreated control cells.

2.3.4.1. IL-1β and IL-10

Interleukin-1β (IL-1β) protein was induced at both time points and exposure concentrations, corroborating messenger RNA. IL-1β, a crucial mediator of

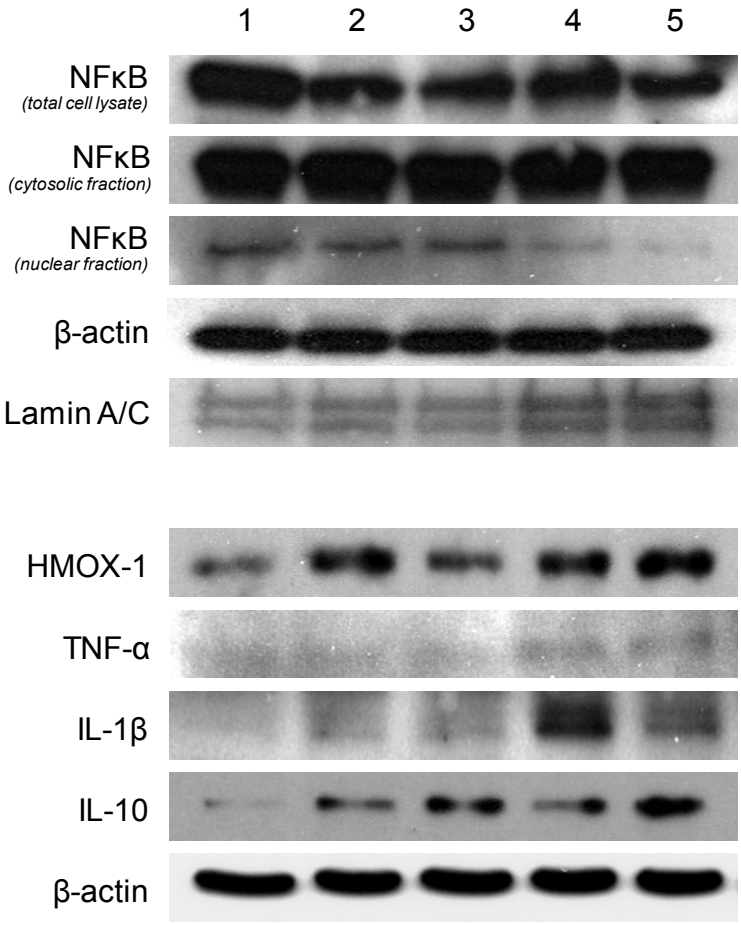

Fig. 2.10. HDF protein expression. Western blots of protein expression along pathway specific proteins. Lane 1: undosed control; 2: CdSe/ZnS-COOH 30 nM after 8 hrs exposure; 3: CdSe/ZnS-COOH 60 nM after 8 hrs exposure; 4: CdSe/ZnS-COOH 30 nM after 48 hrs exposure; 5: CdSe/ZnS-COOH 60 nM after 48 hrs exposure.

inflammatory, proliferation and apoptotic responses, is produced by fibroblasts, as well as other cell types and macrophages. Stronger upregulation was seen at the later time point, especially at the 30 nM concentration.

Interleukin-10 (IL-10) was probed as a bellwether of immunoregulatory protein up regulation following exposure to QDs (Saraiva and O'Garra, 2010). When compared to the unexposed control, both of the 48 hr time point sample sets were upregulated, in addition to a mild increase in expression of the 8 hr QD-treated samples. The increase in cytoplasmic levels of this cytokine are indicative of the diverse mRNA upregulation from immune genes observed by qPCR.

2.3.4.2. TNFα and HMOX1

Tumor necrosis factor-alpha (TNFα) expression was slightly induced at the later time point when compared to undosed cells. Although the primary role of TNFα is that of an acute phase mediator of inflammation, this protein also plays a role in immunoregulation, apoptosis, inhibition of replication and tumor surveillance (Kamohara et al., 2004; Waetzig et al., 2004).

Heme oxygenase-1 (HMOX-1) response from QD exposure proved to be neither solely related to time or concentration, although expression at both time points was consistently increased when compared to the undosed control cells and corroborated the qPCR data for *HMOX1*.

2.3.4.3. NF-κB

NF-κB is involved in regulating many aspects of cellular activity, including stress, injury and especially pathways of the complex immune response. NF-κB is a cytosolic transcription factor, which binds to nuclear DNA and activates transcription of target genes. NF-κB both responds to and induces IL-1β and pro-inflammatory TNFα. While the ultimate gene targets of NF-κB are diverse, its activation has been shown to block apoptosis (Antwerp et al., 1996; Beg and Baltimore, 1996; Liu et al., 1996; Wang and Ron, 1996). Western blot results indicated that while cytosolic NF-κB remained unchanged with QD exposure, nuclear levels decreased over time. Secondary blotting for lamin, a constitutive nuclear protein, revealed that the 48 hr samples exhibited a more concentrated nuclear constituent, suggesting an even stronger suppression than what is shown in the nuclear fraction blot. Probing for NF-κB (p65) in total cell lysates resulted in a fairly consistent degradation of NF-κB levels with QD treatments.

2.3.5. NF-κB transcriptional activity

To confirm the suppressive effect of QDs on transcriptionally active levels of NF-κB, an NF-κB-dependent luciferase gene reporter activity assay was employed. NF-κB and *Renilla* control vectors were transiently transfected into the HDF cells. As shown in Figure 2.11, constitutive NF-κB reporter activity was significantly modulated in transfected cells, agreeing with the western blot and RT-PCR results (Figures 2.8-2.10). Interestingly, the 30 nM QD exposure provoked more significant deviations from the undosed control cells. Luciferase data indicate an initial increase in NF-κB activity at the

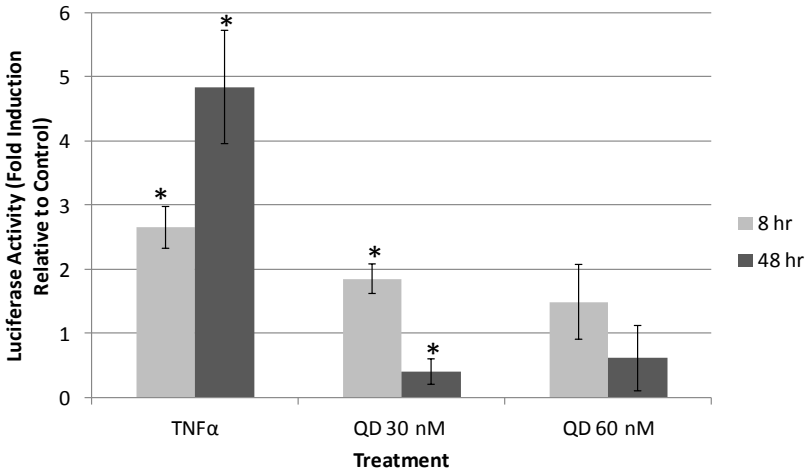

Fig. 2.11. NF-κB transcriptional activity. Changes in transcriptional activity were measured in a dual luciferase gene reporter assay. Luciferase reporters driven by either NF-κB firefly or *Renilla* luciferase response elements were transiently cotransfected into HDF cells. Luciferase activities were quantified using a dual-luciferase reporter assay system. Exposed wells were compared to unexposed transfected cells, which were assigned the value of 1. *$p < 0.05$

earlier timepoint (1.85 and 1.49 fold induction for 30 and 60 nM QDs), followed by suppressed levels (0.403 and 0.612 fold induction for 30 and 60 nM QDs) by 48 hrs.

2.4. Discussion

QD particles modulated gene and protein expression relating to oxidative stress, apoptosis, inflammation, and non-inflammatory immune response pathways, especially genes typically included in the NF-κB pathway. Similar to previously published high exposure concentration studies with nanoparticles, we found that the observed low exposure concentration effects were dependent on QD dosing concentration and exposure time (Delehanty et al., 2006; Hoshino et al., 2004; Kirchner et al., 2005b; Prasad et al., 2010; Su et al., 2009; Tang et al., 2008).

A schematic displaying many of the genes with modulated mRNA expression the NF-κB pathway is shown in Figure 2.12. From this figure, it can be deduced that although the message level of *NFKB1* was up at both 8 and 48 hrs, *NFKB2* message was down at both 8 and 48 hrs. This downregulation of *NFKB2* corresponds with the NF-κB protein analysis data in the western blots. Also, the inhibitory gene, *NFKBIA,* was upregulated, which likely assisted in the prevention of NF-κB translocation in this study. These findings help explain why pro-inflammatory and apoptotic TNFα is allowed to increase in expression over time, since the presence of activated NF-κB can restrict its actions in the cell. There also appears to be a feedback mechanism taking place between *IL-10*, *TNFα*, and *HMOX1*, as the message levels of each were all down at 8 hrs, but all upregulated at 48 hrs. IL-10 has also been shown to inhibit NF-κB (Sanjiv et al., 2009).

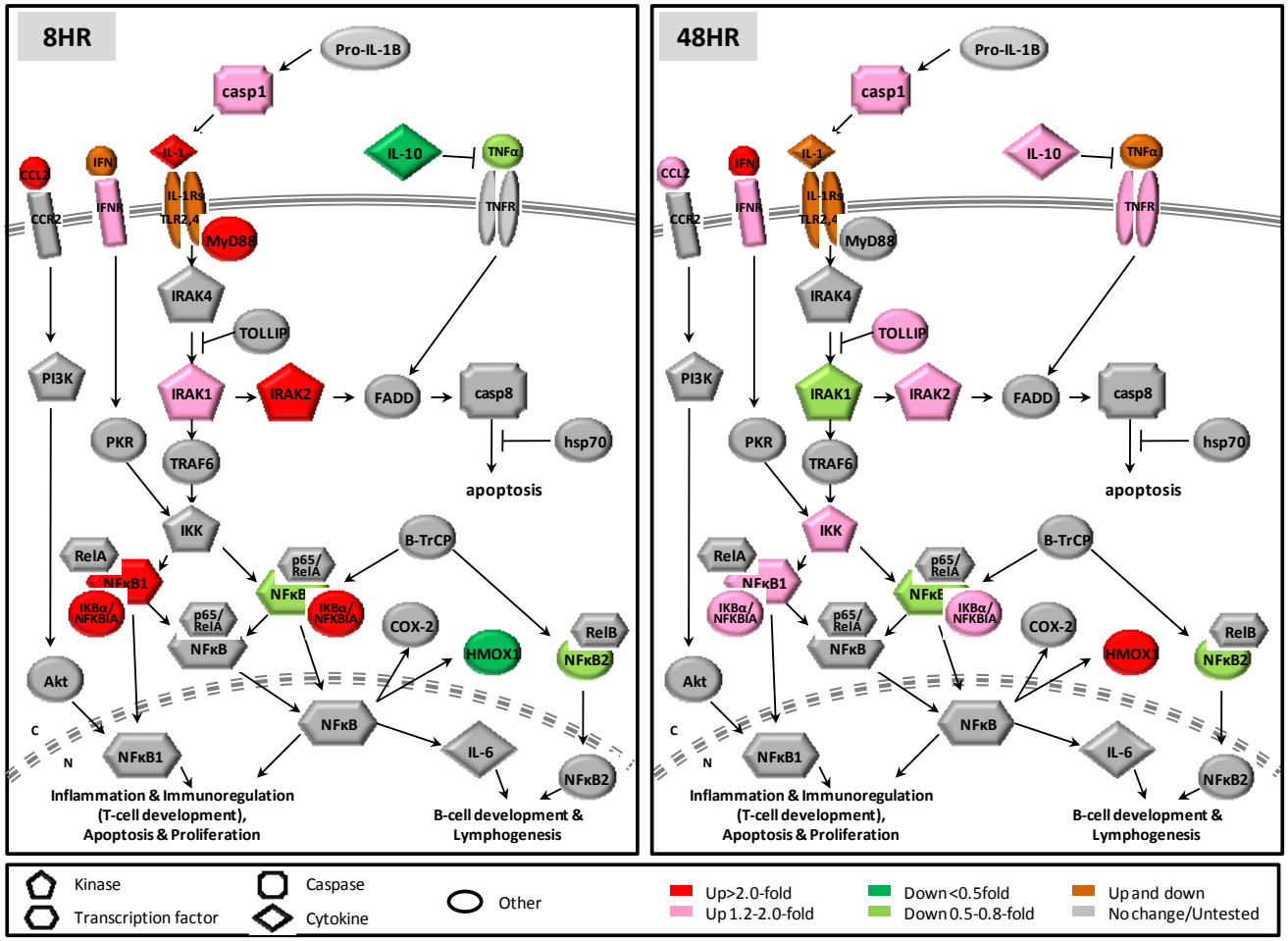

Fig. 2.12. Genes modulated along the NF-κB pathway in HDF exposed to QDs. Colored shapes correlate to modulated genes in HDF cells at 8 hrs (left) and 48 hrs (right).

The upregulation of *HMOX1*, caused by oxidative stress and inflammation has been found to be upregulated and mediated by the NF-κB pathway (Wijayanti et al., 2004). Its corresponding protein, HMOX-1, increased in expression also, as evidenced by western blot.

IL-1 was upregulated strongly at the early time point, but tapered off by 48 hrs after QD exposure. In response to this increase, as well as the presence of TNFα, pro-inflammatory cytokine *IL-6* was upregulated. IL-6 is a well known responder to cellular injury and helps to regulate the acute phase inflammatory response (Kopf et al., 1994; McFarland-Mancini et al., 2010). In a 2007 publication by Ryman-Rasmussen et al., similar increases in IL-1 and IL-6 were found when dermal cells were treated with CdSe/ZnS-COOH QDs (Ryman-Rasmussen et al., 2007). *CCL2*, which is responsible for recruiting T-cells, monocytes, and dendritic cells to the site of injury, was upregulated early (Fantuzzi et al., 2008; Wolter et al., 2008). *SERPINA1* was also upregulated early at both dosing concentrations to help protect tissues from inflammatory cell enzymatic activity. The ligands for the initially suppressed C-C type chemokine receptor CCR3 are cytokines including eotaxin, MCP-3, MCP-4 and RANTES, contributing to recruitment and activation of inflammatory cells by HDF (Huber et al., 2000). Platelet activating factor, the ligand of the *PTAFR* gene product, which was upregulated with exposure to QDs, is a potent phospholipid activator and mediator of inflammation, as well. The A_{2A} adenosine receptor (A_{2A}AR) is known to mediate anti-inflammatory actions in a variety of cell types, where upregulation of the receptor is part of a delayed feedback

mechanism initiated through NF-κB to terminate the activation of macrophages (Murphree et al., 2005).

Cellular decisions to resist apoptosis occurred early, as evidenced by induction of *NFκB1* and *NFKBIA*, as well as the gene for A_{2A}AR, *ADORA2A*, which also acts to block apoptosis by inhibiting TNFα (Ohta and Sitkovsky, 2001). However, pro-apoptotic genes were upregulated by 48 hrs post-exposure. For example, *casp1*, the gene coding for an enzyme known to cleave IL-1β into its mature form (Cerretti et al., 1992) and induce apoptosis when overexpressed (Miura et al., 1993) became upregulated at the later time point. *Casp4*, *NLRC4*, and *TNFα* also increased by 48 hrs. In regard to concentration, the higher 60 nM dose at 48 hrs provoked 75% of the apoptosis pathway genes analyzed to upregulate (Figure 2.13).

Interestingly, Ramage et al (2004) both found that ultrafine carbon black particles also modulate the NF-κB pathway. Ramage showed that exposure to carbon black particles caused an over expression of CRP in human long epithelial cell line (A549), which in turn is dependent on the NF-κB pathway. They found that CRP is synthesized and the NF-κB pathway is modulated in cells when IL6, TNFα, IFNγ, and IL1β are expressed (Ramage et al., 2004). Both ultrafine carbon black and engineered quantum dot particles modulate similar genes, thus both particle-types seem to operate under the same mode of action intracellularly.

In general, the cells exposed to QD nanocrystals induced a widespread modulation of genes and proteins, overall, when compared to unexposed control cell populations. Genes such as *ADORA2A*, *CCL2*, *IL1B*, *IL6*, *IRAK2*, *NFκBIA*, and

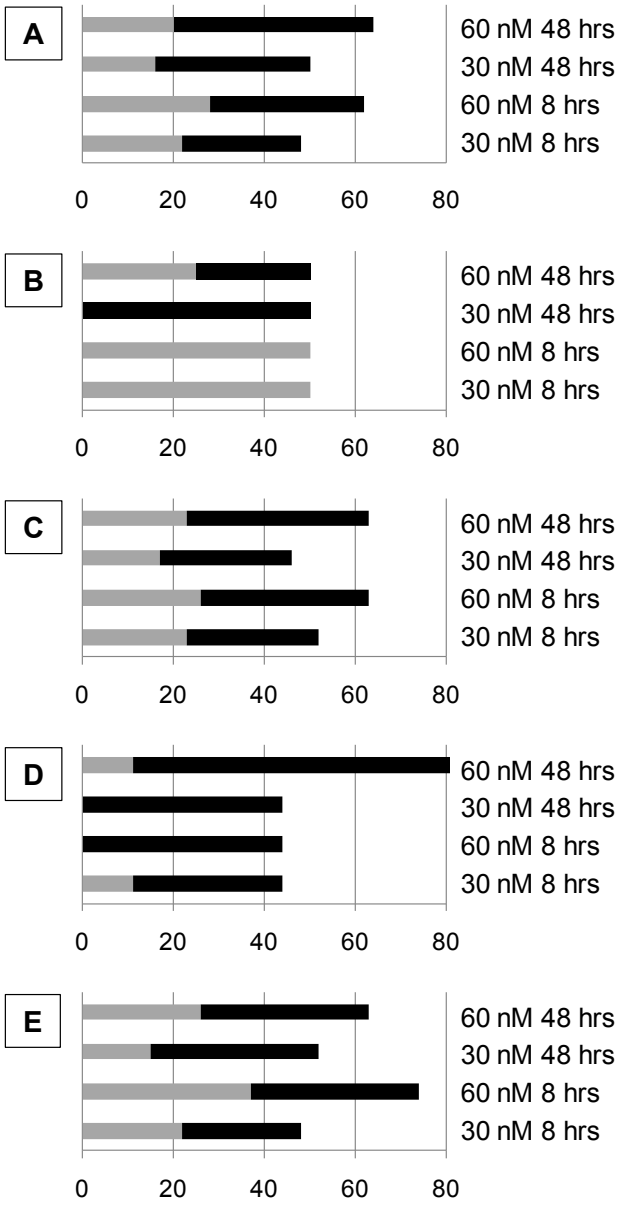

Figure 2.13. Gene modulation summary. A comparison of percent up and downregulation of genes in response to 30 and 60 nM CdSe/ZnS-COOH at 8 and 48 hrs time points. Data is categorized into the following 5 groups: All 50 genes (A), oxidative stress genes (B), inflammatory genes (C), apoptotic genes (D), and non-inflammatory immune genes (E). Graphs represent data from heat map, where values <0.8 were considered for downregulation (gray) and >1.2 (black) were considered for upregulation.

SERPINA1 for example, are upregulated after exposure to QDs, in addition to proteins, such as HMOX-1, IL-10, IL-1B, and TNF-α. Western blotting, however, indicated a decrease in NF-κB translocation, which likely played a role in the increase in apoptotic markers at the later time point. These modulated genes and proteins are indicators of oxidative stress, apoptosis, inflammation, and more general immune responses. Luciferase data revealed nearly a 2-fold induction in NF-κB levels at 8 hrs, followed by suppression at 48 hrs, as compared to control values, indicating transcriptional modulation. Immunocytochemistry demonstrating NF-κB nuclear translocation events revealed similar trends (Figure 2.14). This difference in levels mirrors the mRNA data, as well as protein levels at the 48 hr time point. While this work provides a more specific mechanistic analysis of fundamental toxicological pathways induced or suppressed after QD exposure, future studies require the use of animal models to validate these findings and bridge these data to human exposure scenarios.

The research presented herein offers an alternate methodology and increased understanding of low-concentration nanotoxicological immune research specific to CdSe/ZnS-COOH water-suspendable QD systems. Future *in vivo* work will attempt to corroborate these findings in the more complex cellular environment of animal exposures and assign temporal sequence to the NF-κB-mediated processes perturbed.

Salient points to be learned from this research:

- *The response to QDs is cell-type specific.*
- *NF-κB and associated inflammatory/oxidative stress pathway-related genes and proteins are perturbed after exposure to QD nanoparticles.*

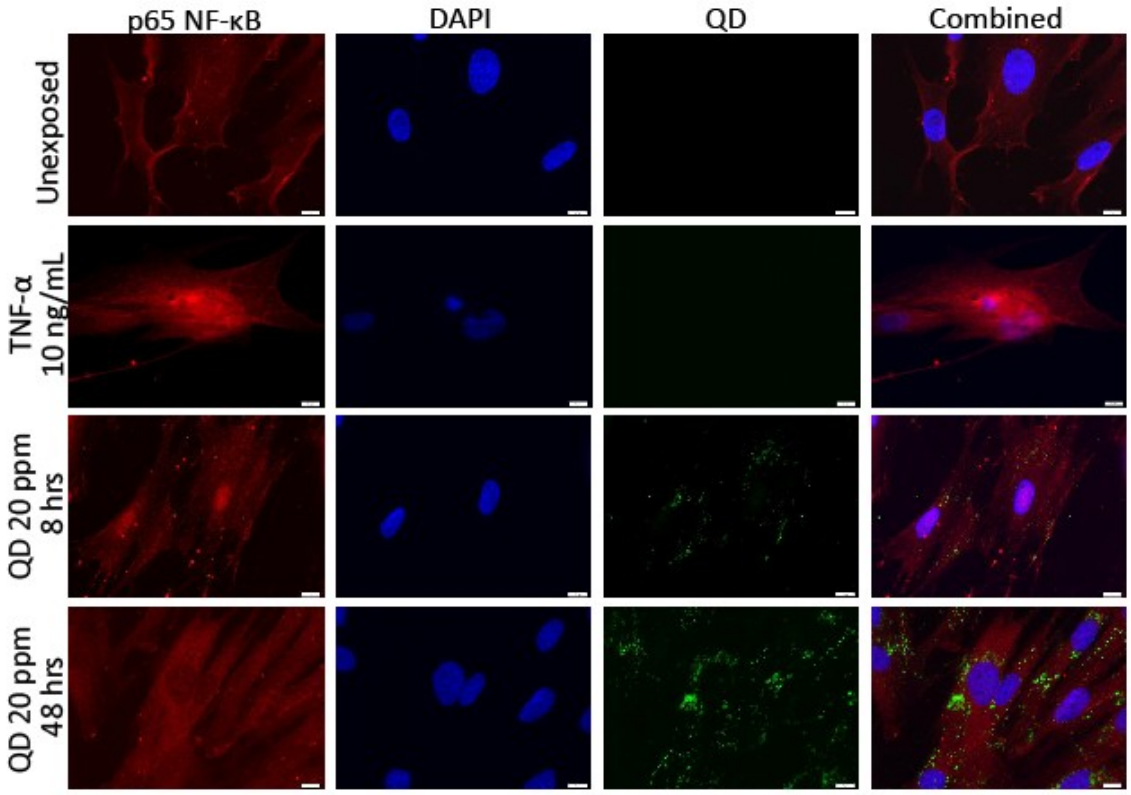

Figure 2.14. NF-κB translocation. Effects of nanoparticles on nuclear accumulation or suppression of NF-κB in HDF. Localization of the p65 subunit of NF-κB was assessed by using immunofluorescence. HDF were either A) untreated, treated with B) TNFα (20 ng/mL) as a positive control, or C) 20 ppm QD suspensions for 8 or 48 hrs. QDs induced nuclear translocation of NF-κB at the earlt time point, but NF-κB levels subsided by 48 hrs, even as QDs increased within the cytosol. Scale bar=10 μm.

Questions remaining unanswered:

- *What are the downstream effects of NF-κB on oxidative stress mechanisms?*
- *To what extent does NF-κB play a role in cells exposed to various nanoparticles?*

CHAPTER III

DISTINCT IMMUNOMODULATORY EFFECTS OF A PANEL OF NANOMATERIALS IN HUMAN DERMAL FIBROBLASTS*

3.1 Introduction

There has been rapid progress in the field of nanotoxicology in recent years; however, information regarding the potential for adverse health outcomes arising from nanoparticle exposures is still lacking. For example, the cellular immunoregulatory response to nanoparticles is not well understood. Materials on the nanometer size scale are thought to impose different types of chemical and/or biological effects on organisms compared to materials of the same chemical composition but on the micrometer size scale. This phenomenon is attributed to the finer size and corresponding larger surface area per unit mass that is characteristic of all engineered nanoparticles (Maynard and Kuempel, 2005; Monteiller et al., 2007; Oberdorster et al., 2005). However, it is largely unknown which specific pathways or subcellular mechanisms of action are triggered as a result of nanoparticle exposure. Some studies have shown that nanoparticles can be internalized into cells. Other studies have shown various uptake mechanisms for nanoparticles (Duan and Nie, 2007; Jaiswal et al., 2003; Zhang and Monteiro-Riviere, 2009). But few studies have investigated the subsequent mechanisms of injury, including key genes and proteins that participate on the molecular level. A key missing

---

*Reprinted with permission from "Distinct Immunomodulatory Effects of a Panel of Nanomaterials in Human Dermal Fibroblasts" by Romoser, et al., 2012. *Toxicology Letters*, *In Press*, Copyright [2012] by Elsevier Ltd.

component of most nanotoxicology studies is the query and determination of toxicological process development. We hypothesized that immune mediators of inflammation, such as the transcription factor, NF-κB, may be initiated in the exposed cell layers, and followed by upregulation of inflammatory response proteins. NF-κB may be partially affected by MAPKs, such as ERK1/2 and p38, which are known to phosphorylate the NF-κB inhibitor (Müller et al., 2002). We have found that these initiators are, at least in part, dependent on nanoparticle type and the cellular stress response ability of the cell.

We previously showed that quantum dot exposure modulates NF-κB in human dermal fibroblasts (HDFs) (Romoser et al., 2011b). NF-κB is a major transcription factor responsible for regulating genes of both the innate and adaptive immune response (Livolsi et al., 2001). NF-κB becomes activated through distinct signaling components: inactivated, cytosolic NF-κB is complexed with the inhibitory IκBα (NFKBIA) protein. A variety of extracellular signals can be recognized via integral membrane receptors, which can lead to the activation of the enzyme IκB kinase (IKK or IKBKB). The role of IKK is to phosphorylate the NF-κB-associated IκBα protein, resulting in ubiquination and dissociation of IκBα from NF-κB. IκBα is degraded by the proteosome and the liberated NF-κB is then translocated into the nucleus where it binds to specific DNA motifs in promoters, termed response elements. Here, it can upregulate genes involved in immune cell development, and maturation, as well as those dedicated to survival, inflammation, and lymphoproliferation (Zandi, 1997).

In an attempt to elucidate these immune response mechanisms, primary HDF cells were utilized to investigate the molecular toxicological mechanisms of a collection of similarly sized nanoparticles. Fibroblasts are the most common cell-type in the dermis, and their ubiquity makes them more appropriate for this study than the rare patrolling macrophages. Contact with the skin is one of the major routes of both intentional and accidental exposure to nanoparticles. Four dermally relevant nanoparticles, citrate-stabilized silver, hydroxylated fullerenes (fullerol), CdSe/ZnS-COOH quantum dots, and anatase titanium dioxide, were chosen to compare and contrast cellular responses.

Because of their unique characteristics, quantum dots are used at increasing rates for a wide variety of industrial and consumer-based applications, including biomedical imaging agents, inks, and solar panels (Alivisatos et al., 2005; Gao et al., 2004; Michalet et al., 2005; Roco, 2003). Zhang et al. (2008) and Mortensen et al. (2008) both concluded that quantum dots of similar or identical structure and composition to those used in this study could penetrate through the epidermis into the dermis, especially with flexing of the skin or by way of hair follicles (Mortensen et al., 2008; Zhang and Monteiro-Riviere, 2008). Microscopy from their publications revealed that a considerable portion of the dose penetrated to the dermis. Silver is currently being utilized as an antimicrobial agent in many dermal applications and has been found to penetrate intact and damaged skin (Larese et al., 2009; Samberg et al., 2010). Titanium dioxide, a common ingredient in sunscreens and cosmetics, is generally recognized as safe for dermal exposure. However, while most titanium dioxide studies involving healthy skin report an absence of penetration, this may not necessarily be the case with

damaged skin (Senzui et al., 2010) (L'Oreal unpublished study-2009-2011). We also examined the effects of fullerol exposure on dermal cells in this study. Fullerol has been reported to possess antioxidant abilities (Djordjevic et al., 2005; Mirkov et al., 2004; Wang et al., 1991) and has, for that reason, been added to cosmetic preparations with the intention of preventing oxidative damage to the skin due to aging and sun exposure. But there have also been reports of toxicity associated with exposure to fullerol and other carbonaceous cage nanostructures. For example, Xia et al. (2010) have recently reported that, depending on the vehicle composition, pristine fullerene nanoparticles can penetrate deeply into the stratum cornea in healthy skin, as tested both *in vitro* and *in vivo* (Xia et al., 2010). In another study, fullerol caused delayed cell death characteristic of apoptosis, including DNA damage in rodent and human glioma cells, which was determined to be caused in the absence of ROS (Isakovic et al., 2006). The dermal permeation capability or toxicity of fullerol, specifically, has not been assessed, although fullerene-based peptides were shown to penetrate intact skin, which was exaggerated with mechanical stress leading to infiltration into the dermis (Rouse et al., 2007).

In an effort to increase current knowledge regarding pathways of the human cellular response to aqueous silver, fullerol, quantum dots, and titanium dioxide, we have quantitatively investigated effects of exposure on the expression of 84 unique genes in HDF cell cultures. In this study, we compared the dose-response and time-course effects of four nanoparticles in dermal cells capable of exhibiting inflammatory response, immunoregulation, apoptosis, and cellular stress. Additionally, we tested whether NF-κB was modulated, as was found in our previously published study

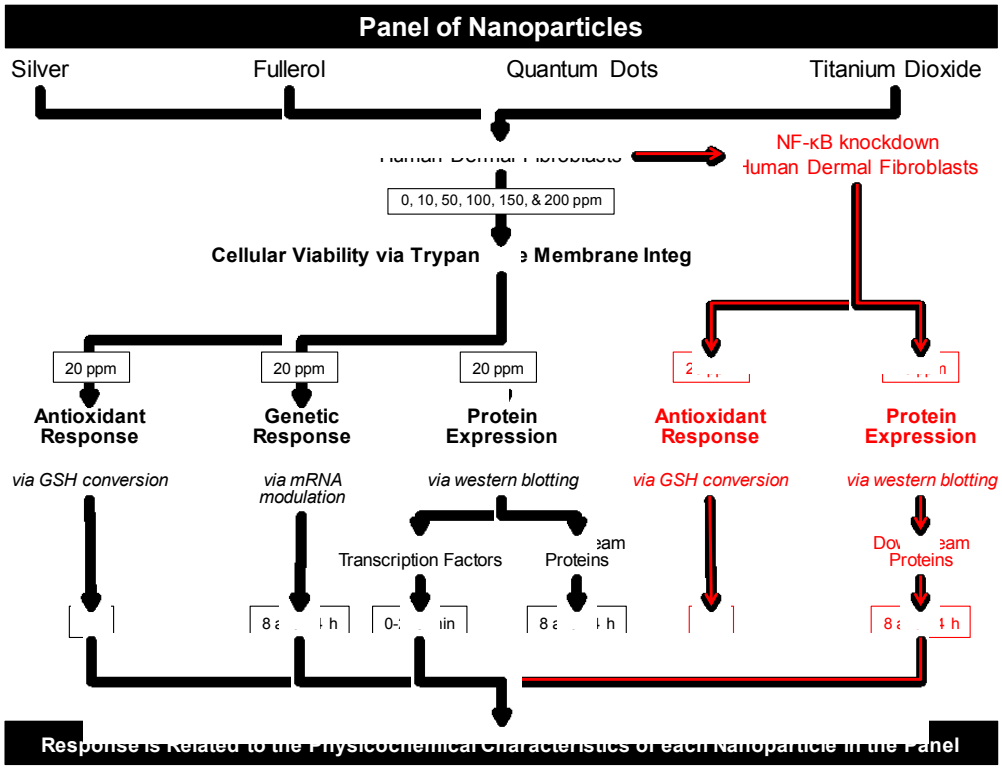

Fig. 3.1. Experimental design. Progression of experiments with four disparate nanoparticles tested in primary dermal fibroblasts with or without NF-κB signaling competency. Arrows relate viability, antioxidant, transcriptional and protein assays with nanoparticle concentrations cells and exposure times.

(Romoser et al., 2011b), in cells exposed to other nanoparticles and determined to what extent NF-κB played a role in the cellular response to NPs by overexpressing the inhibitor, IκBα. We have included an experimental design flowchart that outlines all experiments carried out (Figure 3.1).

3.2 Methods

3.2.1. Nanoparticle characterization

Aqueous citrate-stabilized silver particles (NanoComposix, San Diego, CA); hydroxylated fullerenes (MER Corp., Tucson, AZ); CdSe/ZnS-COOH crystalline quantum dots (Invitrogen Corp., Carlsbad, CA); and anatase titanium dioxide (NanoAmor, Houston, TX) characterization data is summarized in Table 3.1. The hydrodynamic diameter and zeta potential of all four nanoparticles were measured using a Zeta Sizer Nano Series ZEN 3600 Spectrometer (Malvern Instruments Ltd, Malvern, Worcestershire, UK). Particle characterization was performed on the particles suspended in Milli-Q ultrapure water (18.2 mΩ), as well as in DMEM supplemented with 10% FBS at 0, 24, and 48 h time points. Elemental analyses were determined via inductively coupled plasma-mass spectroscopy (Elan DRC II, Perkin Elmer SCIEX). Transmission electron microscopy (TEM) grids were glow discharged using PELCO easiGlow (Ted Pella, Inc., Redding, CA) in order to make the grid surface hydrophillic. Fifteen microliters of solution was applied to 200 lines/inch square mesh copper grids (Electron Microscopy Sciences, Hartfield, PA). Grids were analyzed on a FEI Tecnai G2

Table 3.1. Characterization table. Nanoparticle size as measured by manufacturer, transmission electron microscopy, and dynamic light scattering, zeta potential, and density of silver, fullerol, quantum dots, and titanium dioxide.

Characterization	Silver		Fullerol		QD		TiO_2	
Primary particle size reported by manufacturer (nm)	25		15		16		25	
Primary particle size measured by TEM (nm)	20		-		10		15	
Density (g/cm^3)	10.5		0.8 (fullerene)		4.95 (CdSe/ZnS)		3.90	
Size measured by DLS (nm)	**Water**	**Media**	**Water**	**Media**	**Water**	**Media**	**Water**	**Media**
0 hr	53.5 ± 2.3	169.1 ± 2.3	238.5 ± 9.0	101.6 ± 5.0	12.7 ± 0.3	27.3 ± 1.0	40.1 ± 2.7	313.9 ± 63
24 hr	354.2 ± 23	123.2 ± 4.1	30.6 ± 0.6	121.1 ± 4.7	23.1 ± 1.6	22.5 ± 0.6	155.8 ± 29	16.9 ± 0.6
48 hr	345.1 ± 3.0	166.3 ± 3.4	31.0 ± 0.4	194.8 ± 4.2	38.5 ± 7.8	25.1 ± 0.8	1331.9 ± 540	248.8 ± 150
Zeta potential (mV)	**Water**	**Media**	**Water**	**Media**	**Water**	**Media**	**Water**	**Media**
0 hr	-48.2 ± 8.5	-9.1 ± 2.0	-51.3 ± 6.9	-13.2 ± 1.1	-50.7 ± 5.9	-4.4 ± 1.0	+41.5 ± 8.4	-11.3 ± 1.0
24 hr	-54.8 ± 1.9	-10.3 ± 1.3	-10.4 ± 4.5	-14.5 ± 0.8	-7.9 ± 2.8	-1.1 ± 0.2	+10.9 ± 0.9	-11.8 ± 1.3
48 hr	-55.7 ± 3.0	-11.3 ± 1.4	-26.6 ± 3.0	-14.7 ± 0.3	-39.4 ± 6.5	-5.2 ± 0.8	-0.5 ± 0.4	-13.2 ± 0.4

F20 at an accelerating voltage of 200 kV. Images were recorded using a Gatan CCD camera.

3.2.2. Cell culture and experimental dosing

Human dermal fibroblasts. Cryopreserved primary HDF cells (PCS-201-010, ATCC, Manassas, VA) were cultured in Dulbecco's Modified Eagle's Medium supplemented with 10% FBS (Gibco, Austria). Media was supplemented with an antibiotic cocktail consisting of penicillin, streptomycin, and amphotericin (Sigma-Aldrich, St. Louis, MO). Incubation took place at 37°C with humidity and 5% CO_2. Cells were grown to 80% confluency in 6-well plates, then exposed to nanoparticles (20 ppm final exposure concentrations) or untreated for a negative control. Cells treated with nanoparticle suspensions were very briefly exposed to light in the cell culture hood at the points of exposure and harvesting. Cellular incubations with nanoparticles took place in the dark.

Stable transduction of HDF cells. An additional group of HDF cells was virally transduced to overexpress IKBα, the inhibitor of NF-κB, to assess differences in viability, antioxidant usage, and protein expression with and without NF-κB competency. HEK-293T Ampho-Phoenix packaging cells, capable of carrying plasmids for long-term stable production of lentivirus, were obtained with permission from Gary Nolan at Stanford University and maintained in DMEM containing 10% FBS at 37°C with 5% CO_2. HDF cells were maintained as aforementioned. This transduced HDF cell line is referred to as "NF-κB knockdown" cells throughout the manuscript.

Construction of plasmid. IκB-SR (Super Repressor) was amplified with primers 5′-ATG TTC CAG GCG GCC GAG-3′ and 5′-TCA TAA CGT CAG ACG CTG GC-3′, cloned onto pCR2.1 TOPO (Invitrogen) and subcloned onto pLPCX (Clontech) using *EcoRI* restriction sites.

Stable transduction in cell lines. HEK-293T amphotrophic Phoenix cells were transfected with 10 μg retroviral vectors (pLPCX) with or without insert. After 24 h, cells were placed at 32^{o}C. Viral media was harvested 48 and 72 h after transfection and used to infect cells. After 24 h of resting in nonselective media, cells were selected with 0.4 μg/ml puromycin for 48 h. Empty vector does not appreciably alter gene expression profile. Real time PCR compared expression of genes from cells treated with empty vector (no NF-κB construct) to the cells that received no nanoparticle and were harvested at 8 hours (data not shown).

3.2.3. Cell viability

HDF and NF-κB knockdown cells were cultured in 24-well plates as described above. Cells were then exposed to silver, fullerol, quantum dots, or titanium dioxide to give final well concentrations of 0, 10, 50, 100, 150 or 200 ppm. Cells treated for 24 or 48 h were washed, trypsinized, and resuspended in cell culture media. Percentages of viable cells were measured by mixing equal volumes of cell suspension and trypan blue stain, followed by membrane permeability-based counting in an automated cell counter (Countess, Invitrogen). Viability experiments were done in quadruplicate. A student's t-test was employed to calculate significant change in viability, as compared to the

untreated control samples. Statistical significance was also calculated for differences between normal and NF-κB knockdown cells.

3.2.4. GSH oxidation assay

A luminescence-based assay (V6611, Promega, Madison, WI) was utilized to detect and quantify levels of oxidized glutathione (GSSG) in both untreated and 20 ppm nanoparticle-treated HDF and NF-κB knockdown cells. GSSG determinations were based on a reaction scheme consisting of GSH-dependent conversion of a GSH probe to luciferin by a glutathione S-transferase enzyme. Both GSH and GSSG are present in cells. Therefore, in order to measure oxidized glutathione only, cells were lysed and GSH was blocked. The resulting GSSG was reduced to GSH to measure oxidized glutathione. Antioxidant experiments were done in triplicate.

3.2.5. Gene expression analysis

Cells cultured and exposed to 20 ppm nanoparticle suspensions were harvested at time points of 8 or 24 h. An RNeasy® Mini Kit (Qiagen, Frederick, MD) was used in conjunction with an on-column genomic DNA digestion to lyse cells and extract total RNA. An RT^2 First Strand Kit (C-03) from SABiosciences was utilized prior to quantitative real-time PCR (RT-PCR) to reverse transcribe messenger RNA into cDNA. This cDNA was prepared for a pathway-focused gene expression profiling PCR array system, specific for 84 genes of innate and adaptive immune responses (RT^2 Profiler™, SABiosciences, Frederick, MD), of which data from 42 passed quality control in all

conditions and are compared here. After adding the cDNA to a PCR reaction master mix containing SYBR green, 25 μL of sample was loaded into all wells of 96-well plates pre-filled with primer sets including housekeeping genes, gDNA controls, reverse transcription controls, and positive PCR controls. Using a Roche LightCycler® 480 (Roche, Indianapolis, IN) for RT-PCR, a two-step thermal cycling program was followed: 1 cycle at 95°C for 10 min, then 45 cycles of 95°C for 15 s, then 60°C for 1 min. The Roche LightCycler® 480 software was utilized for raw data acquisition and calculation of Ct (threshold cycle) values.

3.2.6. Protein expression alteration

HDF and HDF transduced with empty vectors (i.e. no IκBα overexpression capability) were cultured in the same conditions as above. Nanoparticle-treated and untreated cells were washed in ice cold 1X PBS, then protease inhibitor cocktail (Sigma-Aldrich) and high salt lysis buffer were added to wells. Protein was isolated by collecting supernatant via centrifugation. Fractionated NF-κB samples were harvested without the use of lysis buffer. An NF-κB activation assay kit (FIVEphoton Biochemicals, San Diego, CA) was utilized to obtain nuclear and cytosolic NF-κB fractions from cells. Samples were loaded into 10% SDS-PAGE gels and run at 120 mV. Gels were transferred to PVDF membranes, which were blocked in 5% milk or BSA/PBST and incubated in different primary antibody solutions overnight: p-IκBα, 1:1000 (Abcam Inc., Cambridge, MA), p-ERK1/2, 1:1000 (Cell Signaling Technology, Danvers, MA), HMOX-1, 1:1000 (Santa Cruz Biotechnology, Santa Cruz, CA), p-P38,

1:1000 (Cell Signaling Technology), IL-6, 1:500 (Santa Cruz) or p65 NF-κB, 1:1500 (Santa Cruz). Membranes were washed in PBST several times before secondary antibody (Goat, anti-mouse or anti-rabbit, 1:5000, Santa Cruz) prepared in fresh 5% milk or BSA/PBST solution was added. Membranes were incubated in the secondary antibody at room temperature, and then washed again in PBST. Immobilon™ Western Chemiluminescent HRP substrate (Millipore, Billerica, MA) was added to membranes and film exposures were taken. GAPDH, 1:10,000 (AM4300, Ambion, Austin, TX) and Lamin A/C 1:5000 (sc-6215, Santa Cruz) were used as loading controls. Blots are representative of duplicate or triplicate experiments.

3.2.7. Calculations of gene expression changes

A total of five housekeeping (potential reference) genes were assayed on the plate and included those encoding β_2-microglobulin, hypoxanthine phosphoribosyltransferase 1, ribosomal protein L13a, glyceraldehyde-3-phosphate dehydrogenase, and β-actin. Analytical estimation of internal control gene stability indicated that hypoxanthine phosphoribosyltransferase 1 (*HPRT1*) was most stable based upon lowest variance and standard deviation, and *HPRT1* was utilized for subsequent normalization (Vandesompele et al., 2002).

Changes in gene expression were estimated using the $2^{-\Delta\Delta Ct}$ method (Rouse et al., 2007; Rzigalinski and Strobl, 2009), with *HPRT1* utilized as the stable reference gene for all experimental situations. The fold changes in gene expression were calculated with respect to the expression level of the genes in the respective control group. For

example, 2-fold change of gene A indicates that expression of gene A was twice as large in the treatment group compared to its expression in the control group, while 0.5-fold change of gene A indicates that the expression of that gene was two times less in the treatment group compared to its expression in the control group. More detailed gene annotations and array layout are available at http://www.sabiosciences.com/genetable.php?pcatn=PAHS-065A. Information regarding the manufacturer's estimates for array performance, sensitivity, specificity, and reproducibility are available at http://www.sabiosciences.com/rt_pcr_product/HTML/PAHS-052A.html#accessory.

3.3 Results

3.3.1. Nanoparticle characterization

Nanoparticle characterization results can be found in Table 3.1 and Figures 3.2-3.3. Primary particle size and morphology for all nanoparticles were determined via transmission electron microscopy; dynamic light scattering was utilized to measure the hydrodynamic diameter of the particles when suspended in water and complete cell culture media. Specific results can be found in Table 3.1. Lastly, the densities of the particles are reported to be 3.90 g/cm^3 for titanium dioxide, 10.50 g/cm^3 for silver, 4.95 g/cm^3 for CdSe quantum dots, and 0.80 g/cm^3 for fullerols. No metal impurities were detected via inductively coupled plasma-mass spectroscopy elemental analysis.

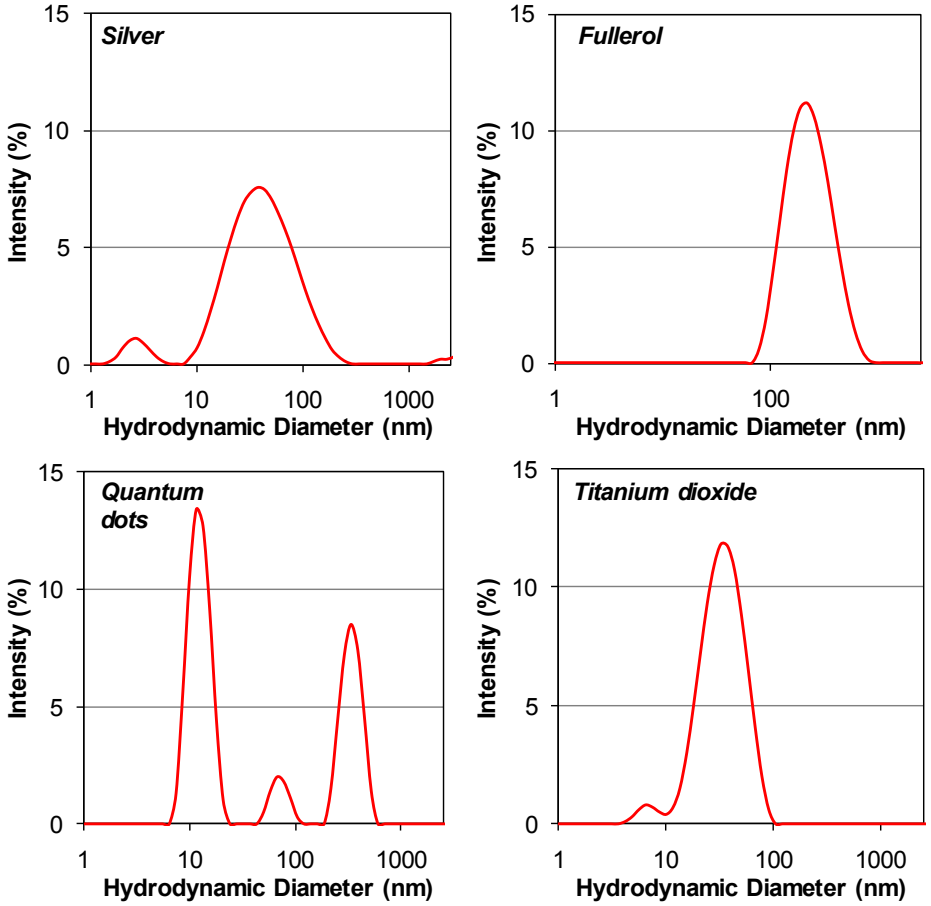

Figure 3.2. Sizing profiles of silver, fullerol, quantum dots, and titanium dioxide particles. Size was measured via dynamic light scattering spectroscopy at a particle concentration of 20 ppm. The size distribution of each particle was measured and graphed as percent intensity versus hydrodynamic diameter.

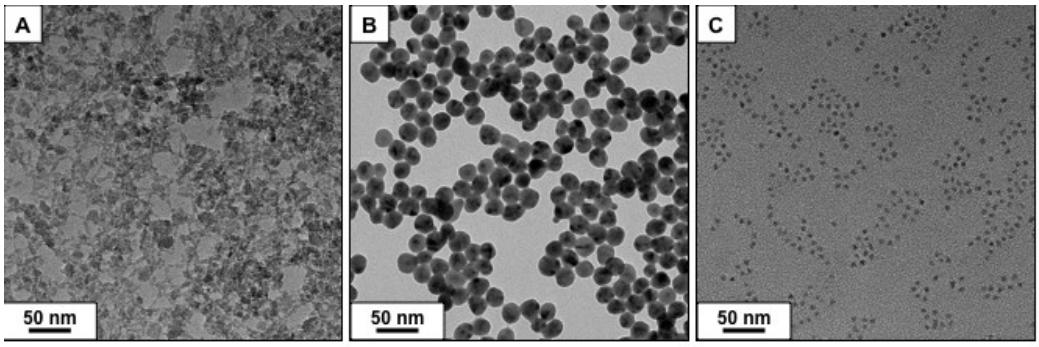

Fig. 3.3. Transmission electron microscopy. A) titanium dioxide, B) silver, and C) quantum dots. Samples were diluted to 20 ppm in Milli-Q water. Characterization was done in cell-free conditions.

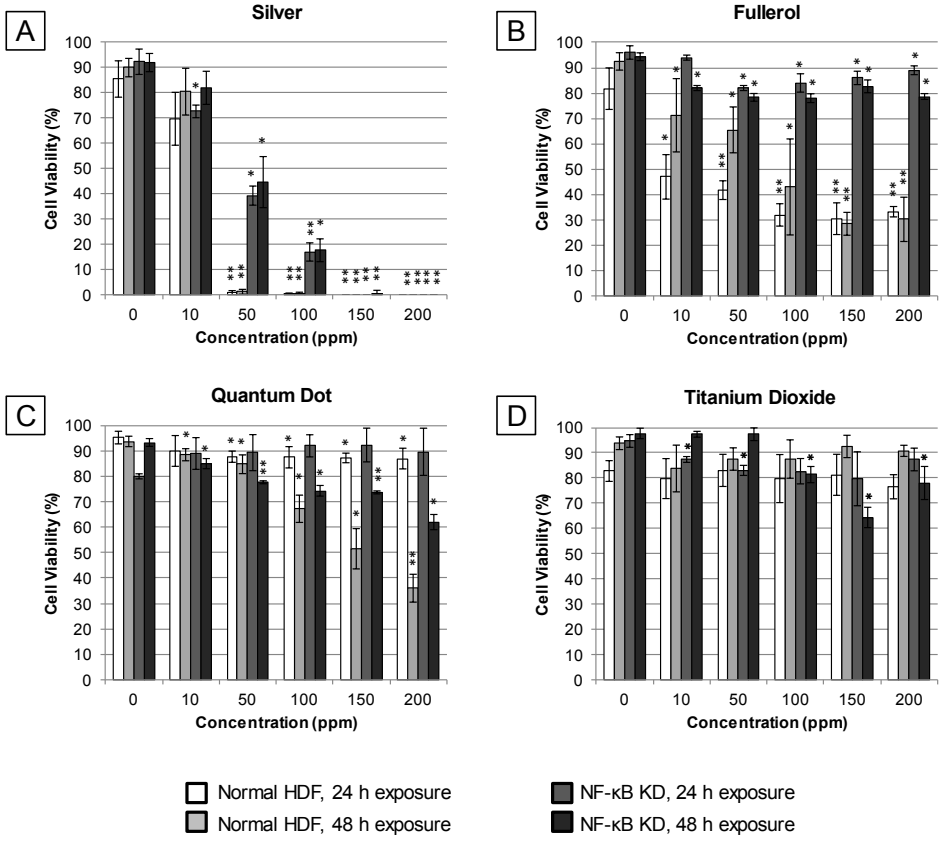

Fig. 3.4. Effects of nanoparticles on cellular viability. Comparison of normal and NF-κB knockdown HDF cellular viability, as measured with the trypan blue exclusion assay. Measurements were taken 24 and 48 h after exposure to 0-200 ppm A) silver, B) fullerol, C) quantum dots, or D) titanium dioxide. *Statistically significant ($p<0.05$) compared to untreated, cell-type matched cells. **Statistically significant ($p<0.001$) compared to untreated, cell-type matched cells.

3.3.2. Cell viability

Cellular viability was measured in HDF cells exposed to each nanoparticle over a dose-response ranging 0 to 200 ppm resulting in a differential cytotoxicity for each particle (Figure 3.4). The trypan blue assay revealed that cell viability decreased (increase in membrane permeability) with increasing concentration of nanoparticle exposures. In addition, the cellular response to particles was found to be different when NF-κB was inhibited in cells. Specifically, the knocked down cells were generally more robust after exposures than normal HDF cells. Conversely, NF-κB knockdown cells were more sensitive to titanium dioxide than normal cells. In normal HDF cells, viability was affected more severely compared to untreated HDF cells when treated with silver, fullerol, or quantum dots. Increasing exposure time to 48 h with quantum dots, fullerols, and titanium dioxide also negatively affected viability, when compared to cells exposed for 24 h.

Regarding the possibility of the citrate stabilizer in the silver material we used to generate additional cellular toxicity, Uboldi et al. (2009) recently concluded that sodium citrate concentrations as high as 0.7 mM resulted in only mild toxicity by 72 h continuous exposure (viability 70%) (Uboldi et al., 2009). They found their data to be consistent with other findings regarding the use of sodium citrate to stabilize nanoparticle suspensions (Connor et al., 2005; Shukla et al., 2005).

3.3.3. Glutathione oxidation assay

Glutathione (GSH) plays an important role in antioxidant defense in eukaryotic

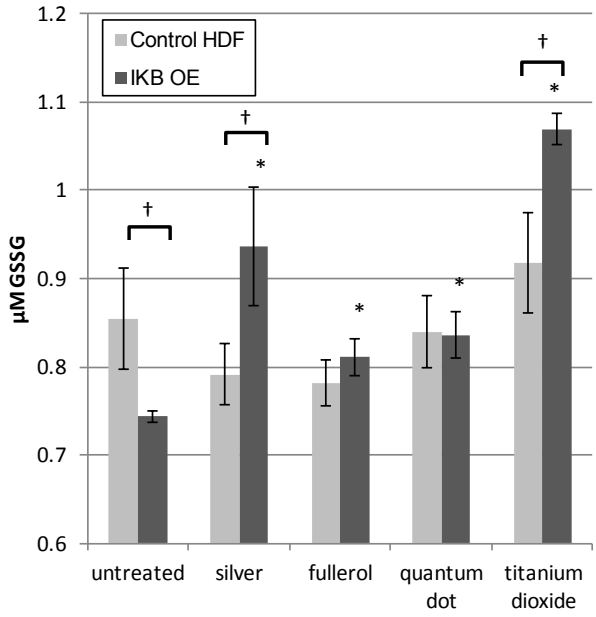

Fig. 3.5. GSH conversion in response to exposures. Oxidized GSH was measured in normal and NF-κB knockdown HDF cells after 20 ppm nanoparticle treatment for 1 h. Responses from untreated cells were also included for comparison purposes. The assay is based on a luciferin conversion reaction catalyzed by glutathione-S-transferase. *Statistically significant ($p<0.05$) compared to untreated, cell-type matched cells. †Statistically significant ($p<0.05$) compared to normal HDF, treatment-matched cells.

cells. To assess antioxidant response after nanoparticle exposures, oxidized GSH was measured in normal and NF-κB knockdown cells after 20 ppm nanoparticle treatment for 1 h (Figure 3.5). Responses from untreated cells were also included for comparison purposes. Knocked down cells exhibited a greater antioxidant response after 1 h than normal cells when exposed to nanoparticles. Silver and titanium dioxide caused more GSH oxidation compared to fullerol and quantum dot-treated cells. This finding indicates that NF-κB plays a substantial role in antioxidant generation after nanoparticle exposures. Oxidative stress leads to the accumulation of oxidized glutathione (GSSG), thus GSSG measurements can be used as an indicator of cellular antioxidant protection effort. GSH experiments were done in quadruplicate.

3.3.4. Gene expression analysis

In general, the 24 h time point revealed much higher upregulation of immune response related genes after nanoparticle exposures (Figure 3.6). This trend was opposite for HMOX1 and TLR3, however. Upregulation of genes was similar between particle types, except for HMOX-1, which was only significantly upregulated with silver exposures. IL-1 family proteins were influenced most. Upregulation of IL-1 family and other genes in normal cells exposed to nanoparticles occurred at 24 h, with the exception of HMOX-1, which was induced at 24 h, but even more so at the earlier 8 h time point.

Analyzing this data by gene function reveals more trends. Many of the genes assayed belong to the IL-1/TLR families and are involved in pathways of inflammation

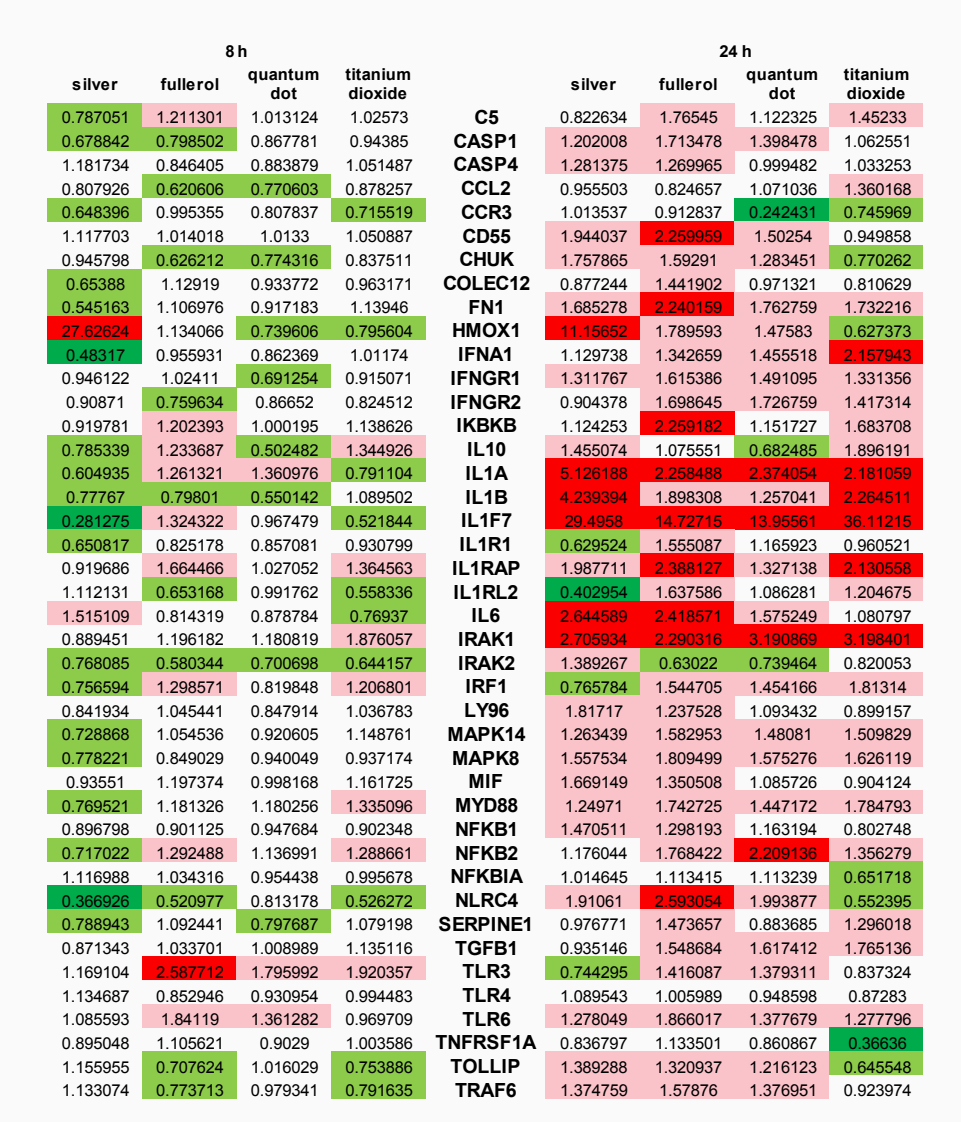

8 h					24 h			
silver	fullerol	quantum dot	titanium dioxide		silver	fullerol	quantum dot	titanium dioxide
0.787051	1.211301	1.013124	1.02573	**C5**	0.822634	1.76545	1.122325	1.45233
0.678842	0.798502	0.867781	0.94385	**CASP1**	1.202008	1.713478	1.398478	1.062551
1.181734	0.846405	0.883879	1.051487	**CASP4**	1.281375	1.269965	0.999482	1.033253
0.807926	0.620606	0.770603	0.878257	**CCL2**	0.955503	0.824657	1.071036	1.360168
0.648396	0.995355	0.807837	0.715519	**CCR3**	1.013537	0.912837	0.242431	0.745969
1.117703	1.014018	1.0133	1.050887	**CD55**	1.944037	2.259959	1.50254	0.949858
0.945798	0.626212	0.774316	0.837511	**CHUK**	1.757865	1.59291	1.283451	0.770262
0.65388	1.12919	0.933772	0.963171	**COLEC12**	0.877244	1.441902	0.971321	0.810629
0.545163	1.106976	0.917183	1.13946	**FN1**	1.685278	2.240159	1.762759	1.732216
27.62624	1.134066	0.739606	0.795604	**HMOX1**	11.15652	1.789593	1.47583	0.627373
0.48317	0.955931	0.862369	1.01174	**IFNA1**	1.129738	1.342659	1.455518	2.157943
0.946122	1.02411	0.691254	0.915071	**IFNGR1**	1.311767	1.615386	1.491095	1.331356
0.90871	0.759634	0.86652	0.824512	**IFNGR2**	0.904378	1.698645	1.726759	1.417314
0.919781	1.202393	1.000195	1.138626	**IKBKB**	1.124253	2.259182	1.151727	1.683708
0.785339	1.233687	0.502482	1.344926	**IL10**	1.455074	1.075551	0.682485	1.896191
0.604935	1.261321	1.360976	0.791104	**IL1A**	5.126188	2.258488	2.374054	2.181059
0.77767	0.79801	0.550142	1.089502	**IL1B**	4.239394	1.898308	1.257041	2.264511
0.281275	1.324322	0.967479	0.521844	**IL1F7**	29.4958	14.72715	13.95561	36.11215
0.650817	0.825178	0.857081	0.930799	**IL1R1**	0.629524	1.555087	1.165923	0.960521
0.919686	1.664466	1.027052	1.364563	**IL1RAP**	1.987711	2.388127	1.327138	2.130558
1.112131	0.653168	0.991762	0.558336	**IL1RL2**	0.402954	1.637586	1.086281	1.204675
1.515109	0.814319	0.878784	0.76937	**IL6**	2.644589	2.418571	1.575249	1.080797
0.889451	1.196182	1.180819	1.876057	**IRAK1**	2.705934	2.290316	3.190869	3.198401
0.768085	0.580344	0.700698	0.644157	**IRAK2**	1.389267	0.63022	0.739464	0.820053
0.756594	1.298571	0.819848	1.206801	**IRF1**	0.765784	1.544705	1.454166	1.81314
0.841934	1.045441	0.847914	1.036783	**LY96**	1.81717	1.237528	1.093432	0.899157
0.728868	1.054536	0.920605	1.148761	**MAPK14**	1.263439	1.582953	1.48081	1.509829
0.778221	0.849029	0.940049	0.937174	**MAPK8**	1.557534	1.809499	1.575276	1.626119
0.93551	1.197374	0.998168	1.161725	**MIF**	1.669149	1.350508	1.085726	0.904124
0.769521	1.181326	1.180256	1.335096	**MYD88**	1.24971	1.742725	1.447172	1.784793
0.896798	0.901125	0.947684	0.902348	**NFKB1**	1.470511	1.298193	1.163194	0.802748
0.717022	1.292488	1.136991	1.288661	**NFKB2**	1.176044	1.768422	2.209136	1.356279
1.116988	1.034316	0.954438	0.995678	**NFKBIA**	1.014645	1.113415	1.113239	0.651718
0.366926	0.520977	0.813178	0.526272	**NLRC4**	1.91061	2.593054	1.993877	0.552395
0.788943	1.092441	0.797687	1.079198	**SERPINE1**	0.976771	1.473657	0.883685	1.296018
0.871343	1.033701	1.008989	1.135116	**TGFB1**	0.935146	1.548684	1.617412	1.765136
1.169104	2.587712	1.795992	1.920357	**TLR3**	0.744295	1.416087	1.379311	0.837324
1.134687	0.852946	0.930954	0.994483	**TLR4**	1.089543	1.005989	0.948598	0.87283
1.085593	1.84119	1.361282	0.969709	**TLR6**	1.278049	1.866017	1.377679	1.277796
0.895048	1.105621	0.9029	1.003586	**TNFRSF1A**	0.836797	1.133501	0.860867	0.36636
1.155955	0.707624	1.016029	0.753886	**TOLLIP**	1.389288	1.320937	1.216123	0.645548
1.133074	0.773713	0.979341	0.791635	**TRAF6**	1.374759	1.57876	1.376951	0.923974

Fig. 3.6. Immune gene expression. Heat map of pathway-specific gene expression changes in normal HDF. Central column shows genes in bold, columns to the left and right show fold change in expression levels in response to the 20 ppm treatment (labeled at top), compared to untreated controls assessed at the same time point (8 or 24 h). Fold suppressions of <0.5 are colored dark green and 0.5-0.8 light green. Fold inductions of 1.2-2.0 are pink and >2.0 red.

and innate pattern recognition. TLR-6 message is upregulated at the later time point for all particles. The TLR-6 protein heterodimerizes with TLR-2 for surveillance of microbial moieties, primarily diacyl lipopeptides. The robust response of IL-1α and IL-1 family member 7 messages after prolonged exposure shows preparation for inflammation. Targeted recruitment of monocytes through CCL2 is not strong, however. Neither the early nor the later time point recorded upregulation of the NF-κB inhibitor, *NFKBIA*, in fact it was downregulated in the 24 h titanium dioxide experiment.

3.3.5. Protein expression alteration

As determined via western blot, NF-κB knockdown cells inhibit NF-κB nuclear translocation, preventing subsequent DNA binding and genetic upregulation; therefore, these cells were determined to be appropriate to assess the role of NF-κB after nanoparticle exposures (Figure 3.7). Real time PCR analysis of immune gene mRNA levels of cells treated with the empty pLPCX retroviral vectors confirmed that the gene knockdown system was not altering genes itself (data not shown).

In assessing early transcription factor involvement, the severity of the NF-κB/ERK response in nanoparticle-treated cells is as follows: silver>fullerol>quantum dot>titanium dioxide. ERK1/2 upregulation either precedes or is nearly concurrent with phosphorylation of the NF-κB inhibitor, IκBα, in silver, fullerol, and titanium dioxide-treated cells, but not quantum dot-treated cells (Figure 3.8). Suppression of IκB phosphorylation suggests that NF-κB inhibition occurs. Induction of phosphorylated p38 is seen at both time points after exposure to all four nanoparticle-types.

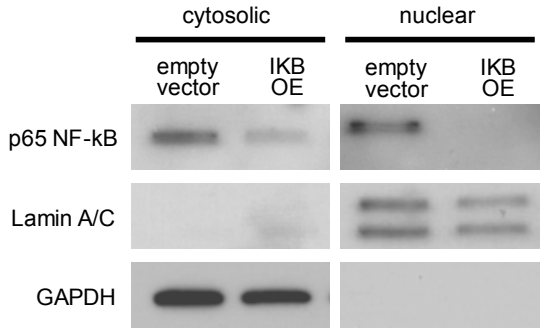

Figure 3.7. Differential NF-κB expression before and after NF-κB inhibition in HDF. Insertion of NF-κB inhibitor, IκB, or empty vector, which exerts antibiotic resistance, but absence of protein overexpression capability, were all probed for p65 NF-κB expression. While both cell types show the presence of NF-κB in cytosolic fractions, IκB overexpressed cells reveal no detectable NF-κB within the nucleus.

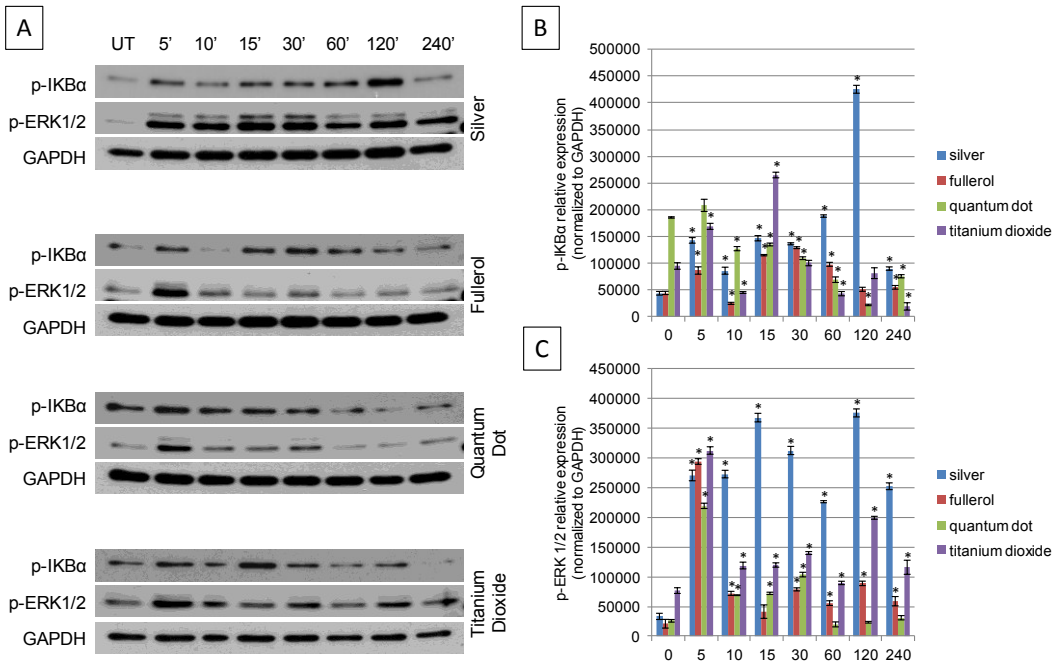

Fig. 3.8. Early transcription factor stimulation. To determine nanoparticle-specific differences in early transcription factor modulation, NF-κB inhibitor, IKBα, and ERK1/2 MAP kinase modulation in normal HDF was assessed after 20 ppm nanoparticle exposure over 5-240 min (A). Blots are grouped by nanoparticle type. GAPDH assured equal protein loading. Blots are representative of three identical experiments. Densitometric analysis was carried out to determine significance of p-IKBα (B) and p-ERK1/2 (C) expression differences in western blot results. Graphed results were normalized to GAPDH loading control and significance was compared between zero and all other exposure time points (zero equals untreated). *Statistically significant (p-val < 0.05).

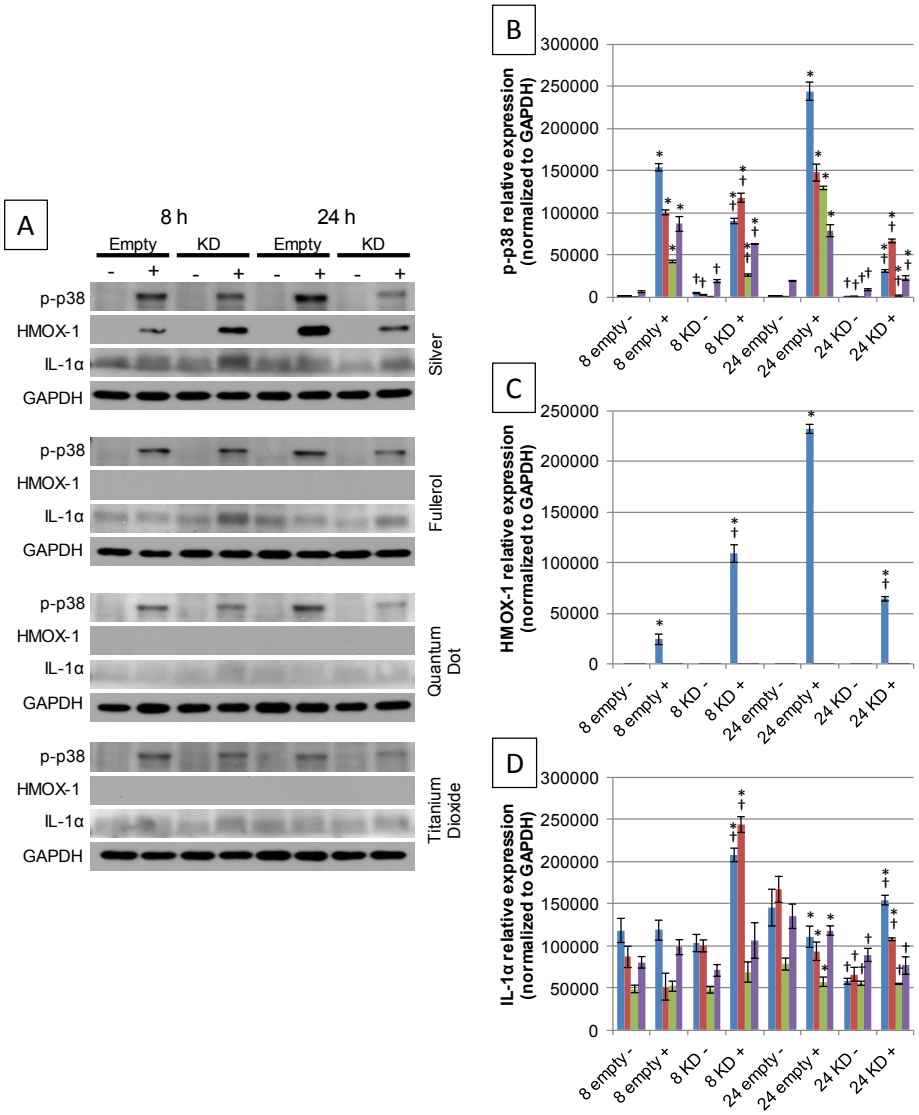

Fig. 3.9. Downstream protein expression. Western blot analysis of NF-κB pathway-related protein expression after 8 and 24 h exposure to 20 ppm silver, fullerol, quantum dot, and titanium dioxide. Phosphorylated p38, HMOX-1, and IL-1α protein levels were assessed in both normal and NF-κB knockdown HDF cells (A). GAPDH assured equal protein loading. Blots are representative of three identical experiments. Densitometric analysis was carried out to determine significance of p-p38 (B), HMOX-1 (C), and IL-1α (D) expression differences in western blot results. Graphed results were normalized to GAPDH loading control. Significance between untreated and treated samples within same time point and cell type is denoted with "*" and significance between samples at same time point and treatment, but differing cell type is denoted with "†". *,† Statistically significant (p-val<0.05).

To analyze downstream protein response arising from perturbation of earlier transcription factor modulation, we probed for induction of phosphorylated p38, HMOX-1, and IL-1α (Figure 3.9). Phosphorylated p38 expression was evident after exposure to all four nanoparticle-types, but was notably less severe with NF-κB knockdown. HMOX-1 expression was limited to silver-treated cells, indicating ROS generation and resistance to protein damage. By 24 h, knockdown cells reveal less HMOX-1 induction. P38 and HMOX-1 results indicate that 24 h exposure with silver and quantum dots causes partial dependency upon NF-κB for oxidative stress-related signaling. IL-1α blots suggest that NF-κB is responsible for controlling much of the inflammatory response in the dermal cells tested.

3.4 Discussion

Specific, pathway-driven cellular responses to nanoparticle exposures need to be further elucidated for improved drug delivery, immune/inflammatory response mechanism elucidation, and gathering of basic toxicological response data. Studies comparing multiple nanoparticle types and probing for specific uptake mechanisms and distinct signaling pathway responses are needed to assess the effects of altering unique physicochemical characteristics of particles, such as chemical composition, size, and surface charge on appropriately dosed cell and tissues in culture.

This research describes a unique systematic investigation designed to assess the impact of a key inflammatory response mediator, namely NF-κB, after exposure to a panel of nanoparticle-types in human skin cells. It is important to note that the cell type

used in the assays was primary in nature, thus the results reported in this study are a better representation of an *in vivo* hazard assessment when compared to results obtained from an immortalized cell line. Lastly, these studies were conducted using very low doses and, thus, may be more physiologically relevant than results from studies that use higher dosing concentrations.

A summary of experiments is outlined in an experimental flowchart (Figure 3.1). The left side (black text) of the chart represents experiments with normal, primary HDF cells, whereas the right side (red text) explains experiments carried out with virally transduced NF-κB knockdown HDF cells. We utilized a step-wise approach, beginning with coarse analyses of viability and antioxidant depletion. Then, we examined the finer analyses of gene and protein modulation. Investigations with knockdown cells were critical to determine the amount of NF-κB contribution after treatments, therefore helping to elucidate one of the primary immune and inflammatory response mechanisms in nanoparticle exposures. By analyzing resultant response data, we were able to make several speculations regarding the relationship between nanoparticle characteristics and cellular stress or inflammatory response outcomes.

The characteristics of every particle-type used in these studies were measured for size and agglomeration state, surface charge, purity, density, and crystallinity. These particles were selected because they were (1) produced in the liquid-phase with specific surface modifications to remain as suspensions in the aqueous phase for longer than 30 days on the shelf and (2) engineered to be of equivalent primary particle size. The silver particles were citrate stabilized, the fullerols were fully hydroxylated, the quantum dots

were modified with carboxyl acid groups, and the titanium dioxide particles were functionalized with acetic acid groups. While these particles were designed to be water-suspendable and intended to remain at a primary size of ~20 nm, the physiologic fluid (i.e. cell culture media) significantly changed the zeta potential of the particles. The change in zeta potential influenced a change in the suspension iso-electric point, which is defined as the pH at which a particle has no net charge. Changes in iso-electric point cause particles that, under ultrapure water conditions, are normally monodisperse to agglomerate and fall out of suspension at differential rates. Here, we observed the silver particles to settle at a much faster rate than any of the other particles. Therefore, the direct interaction between these nanoparticles and the HDF cells took place over a longer time period and with a greater concentration of particles when compared to the other particle-types used in the study. These observations (combined with the increased propensity to produce ROS) led to the heightened NF-κB/ERK response in the cells after exposure to silver. Interestingly, even though titanium dioxide also induced high levels of GSSG, the NF-κB/ERK response in these cells was not elevated. This result further emphasizes that ROS production is not the only physicochemical property of nanoparticles responsible for toxicological response; instead, multiple physicochemical properties often act synergistically or antagonistically to produce a range of biological responses.

Each of the four particles exhibits different physicochemical properties, either in size, charge, or density, that correlate to other results found in this study. For example, the density of silver is much greater than that of the other particles; Quantum dots

acquire a relatively neutral surface charge in media, but remain very small compared to the other three particles; Fullerols agglomerate similarly in water compared to silver, but exhibit a highly negative surface charge early, which could cause an increase in interaction with biological components, such as cell membranes.

We previously reported that quantum dots modulated the transcription factor NF-κB in HDF cells (Romoser et al., 2011b). Lee et al. found that upregulation of ERK1/2 occurred in monocytes, THC-1 cells, and BALB/c mice after exposures to CdSe/ZnS quantum dots (Lee et al., 2009). There are conflicting data in the literature reporting both pro- and anti-oxidant properties after fullerol exposures. C60 fullerenes have been shown to be toxic to HDF cells, but hydroxylated fullerenes have not been tested in dermal cells (Sayes et al., 2004; Sayes et al., 2005). As for silver, Rolla et al. found in a multi-nanoparticle study assessing possible modulation of many cellular signaling pathways that silver significantly downregulated the SMAD/TGF-β pathways, but upregulated the HIF-1α pathway (Rallo et al., 2011). Titanium dioxide has been shown to modulate the NF-κB pathway in both NIH-3T3 and BAES-2B cells exposed to 10 ng/mL and 10 μg/mL, respectively (Chen et al., 2011; Ge et al., 2011). These studies tested aggregated P25 Degussa particles however, unlike the present study.

To evaluate the response to nanoparticles in normal cells, we assayed transcriptional response via a RT-PCR gene array, as well as translational activity by way of protein analysis. A theme that emerges in the immune-transcriptional profile of cells treated with any of the assayed nanoparticles is a preparation for inflammation. Those that were upregulated were pattern recognition receptors (PRRs), their signal

transduction machinery, inflammatory cytokines, and their receptors. Not only was inflammation induced, but transcripts were prepared to put the cell on a hair-trigger to escalate this response. TLR messages were upregulated to survey for pathogen-associated molecular patterns (PAMPs). NF-κB message levels were up and its inhibitors levels were down. MYD88 was prepared to convey recognition of a threat by a PRR. The MAP kinase cascade was primed. The complement cascade was attenuated (via CD55/Decay-accelerating factor) in favor of general inflammation. Additionally, IL-1 message levels increased, initiating the inflammatory cascade.

In evaluating early transcription factor activity, it was evident that the MAP kinase protein ERK1/2 was upregulated very early (within a few minutes of exposure) in the case of each type of nanoparticle exposure. Phosphorylation of IκB seemed to either be concurrent with or immediately followed ERK1/2 activation. Guma et al has recently reported that in mice NF-κB does not trigger destructive inflammation unless MAPKs (ERK and p38) are concurrently expressed (Guma et al., 2011). Silver-treated cells continued to cause upregulation of this signal transduction protein, which was possibly due to its relatively dense nature (see Table 3.1) and ability to settle out faster than the other particles. This density-dependent property of silver potentially exposed the cells to a greater concentration of particles over time.

To assess the extent of NF-κB dependency in cells exposed to a variety of nanoparticles, we analyzed differences in viability, antioxidant depletion, and downstream protein upregulation between knockdown and normal dermal cells. To avoid confounding toxicological effects that can occur with the use of pathway inhibitors

as a method to silence a particular cellular pathway, we virally transduced our cells to specifically overexpress IκBα. In the viability assay, NF-κB knockdown cells were more resistant to death when treated with silver, fullerol, or quantum dots, however, when exposed to titanium dioxide exhibited an opposite trend. NF-κB is known to play a role in apoptosis and may be delaying or preventing apoptosis in these nanoparticle-treated cells. Decreased cell death in knockdown cells may also be partially due to decreased nanoparticle uptake, as compared to normal HDF (data not shown). Our antioxidant data suggests that NF-κB knockdown cells are hypersensitive to insult, compared to normal cells, and allow more antioxidant involvement (increase in GSSH) to occur, possibly protecting cells from ROS generated from nanoparticles and nanoparticle-cell interaction. In other words, NF-κB may be acting to suppress some of the antioxidant response in cells exposed to NPs. We observed that silver was more dense and precipitated out of the media, possibly resulting in higher exposures. That, combined with the fact that titanium dioxide was the only positively charged particle in the study, may be reasons for the exaggerated GSH responses with silver and titanium dioxide exposures. As for differences in downstream protein expression, phosphorylation of p38 was evident after exposure to all four NP types, but was notably less severe with NF-κB knockdown. This finding coincides with earlier studies, which have shown *in vivo* that NF-κB inhibition can lead to anti-inflammatory effects (Broide et al., 2005; Greten et al., 2004). P38 is phosphorylated in response to IL-1 upregulation and further aids in activation of IL-6 (see Figure 3.10). Phosphorylation of p38 and JNK leads to activation

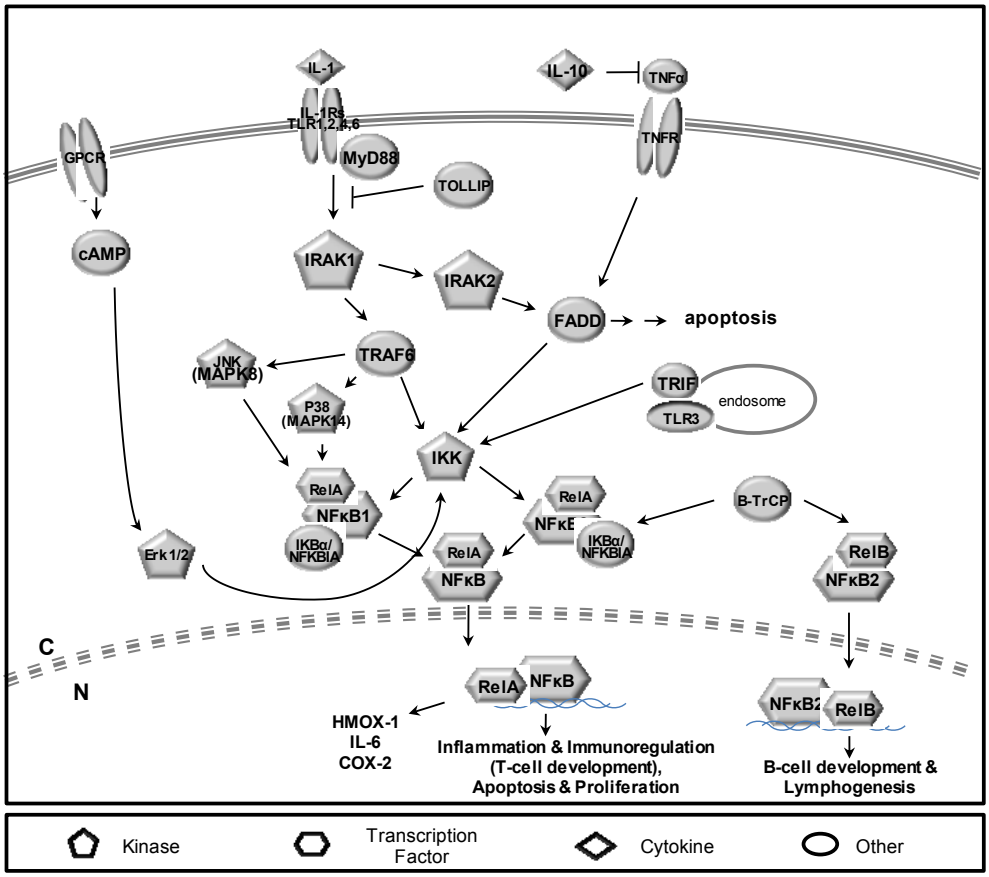

Fig. 3.10. NF-κB pathway schematic. Proposed schematic of HDF NF-κB pathway and related protein involvement after nanoparticle exposures. Protein classification is denoted as such: kinase=pentagon; transcription factor=hexagon; cytokine=diamond; and other proteins=oval.

of NF-κB and inflammatory response. This cascade is driven by ROS and results in downstream upregulation of inflammatory cytokines, such as IL-6, which was upregulated in the gene expression analysis at the later time point with all nanoparticles except titanium dioxide. P38 and HMOX-1 results indicate that 24 h exposure with silver and quantum dot causes partial dependency upon NF-κB for oxidative stress-related signaling. These findings, along with the IL-1α protein levels, suggest that NF-κB is responsible for controlling the majority of the inflammatory response in the dermal cells tested.

The HDF system employed here allowed for the cellular and molecular analysis of potential immunotoxicological pathways triggered by relevant exposures to chemically and physically disparate nanoparticles (Benn et al., 2011; Gopee et al., 2009). Such carefully chosen *in vitro* approaches should expedite and direct subsequent *in vivo* studies to evaluate the safety of these materials.

Salient points to be learned from this research:

- *All nanoparticle types caused transient NF-κB and ERK1/2 responses, with the exception of silver, which caused prolonged expression of these proteins.*
- *NF-κB functions in the oxidative stress response of normal cells by allowing less antioxidant response, thus increased induction of oxidative stress proteins.*

Questions remaining unanswered:

- *What other mechanisms of toxicity develop as a result of nanoparticle exposure?*
- *Does nanoparticle-induced oxidative stress lead to DNA damage?*

CHAPTER IV

LOW DOSE EXPOSURES WITH ROS-PRODUCING METAL OXIDE NANOPARTICLES CAUSE DNA DAMAGE IN PRIMARY HUMAN DERMAL FIBROBLASTS

4.1 Introduction

Nanomaterials are defined as materials that have at least one dimension between 1-100 nm (1 nm = 10^{-9} m) and typically exhibit physicochemical properties not shared by coarser particles of the same chemical composition (2004; Hansen et al., 2007; Nanoscale Science Engineering and Technology Subcommittee, 2004; 2004). The actual size threshold whereby these new properties can be seen is still a matter of debate and one study has reported that 30 nm and less for metal and metal-oxide particles is nearer to the point at which this phenomenon actually occurs (Auffan et al., 2009a). At this scale, the much larger particle surface-to-volume ratio plays a significant role in interaction at the biological interface. Due to the 'non-bulk' properties of nanoparticles, including their atypical surface structure and surface reactivity, processes such as dissolution, redox reactions and the generation of reactive oxygen species may be enhanced. Such properties may elicit biological responses that would not be produced by larger particles of the same chemical composition. Nanotechnology is among the fastest growing areas of scientific research and has important applications in a wide variety of fields. The nanotechnology industry is expected to generate revenues between $2.6

trillion and $3.1 trillion by the years 2014 and 2015, respectively (Dai, 2010; Schmidt, 2009).

Nanoparticles are present in many products that come into contact with human skin. Relevant to this research, titanium dioxide (TiO_2) and zinc oxide (ZnO) are present in many sunscreens to protect against UV-induced skin damage. Metal oxides do not undergo any chemical decomposition as organic compounds do when exposed to UV radiation, which makes them an attractive alternative (Damiani et al., 1999; Knowland et al., 1993). Additionally, they offer a more complete range of protection compared to other products of organic nature (Mitchnick et al., 1999; Serpone et al., 2007). Recently, more products for dermal application utilize finer, nano-sized TiO_2 and ZnO since they are transparent and more esthetically pleasing to consumers at this size. TiO_2 nanoparticles are also used in other products that present dermal contact exposures, such as clothing and surface cleaning agents. CeO_2 nanoparticles have proposed and current uses in the areas of biomedicine, cosmetic products, polishing materials, and automotive fuel additives (Hochino et al., 2001; Jung et al., 2004; Masui et al., 2003; Yabe and Sato, 2003). Opportunities for these types of nanoparticle exposures are increasing on a daily basis (Crosera et al., 2009), as the products containing these materials are quite common and society is increasingly aware of the importance of UV protection, in general, and the use of improved materials. Since little is known regarding the mechanisms of toxicity for these materials, more research is necessary. The data that has been presented up to now in the literature is sparse and contradictory regarding the effects of nanoparticle exposure in dermal models.

Only a handful of studies in the literature have investigated the ability of nanoparticles to penetrate skin (Baroli et al., 2007; Chen and Schluesener, 2008; EPA, 2007; Filon et al., 2006; Gopee et al., 2009; Isakovic et al., 2006; Kielhorn et al., 2006; Mortensen et al., 2008; Oberdorster et al., 2005; Rouse et al., 2007; Samberg et al., 2010; Senzui et al., 2010; Xia et al., 2010; Zhang and Monteiro-Riviere, 2008) The skin is often considered less permeable and the risk perception by this route is generally less than that of respiratory exposure (Donaldson et al., 2006; Limbach et al., 2007; Nel et al., 2006; Oberdorster et al., 2005; Shimada et al., 2006). However, in the literature there are studies which suggest that the skin is an important route of entry for nanoparticles both in occupational and consumer settings (Gopee et al., 2009; Mortensen et al., 2008; Ryman-Rasmussen et al., 2006; Sonavane et al., 2008; Vogt et al., 2006) and it has been specifically shown that certain particles are more prone to dermal penetration based upon their physicochemical properties or the nature of the vehicle they are suspended in (Xia et al., 2010). Bennat and Müller-Goymann (2000) found that different formulations had different penetration abilities: according to their experiments, microfine TiO2 penetrated deeper into human skin from an oily dispersion than from an aqueous one, and encapsulation of the pigments into liposomes caused a higher penetration into the skin (Bennat and Muller-Goymann, 2000). Furthermore, penetration was greater when applied to hairy skin, suggesting a surface penetration through hair follicles or pores. Recently, studies have emerged that have actually quantified the percentage of nanomaterial that breached the stratum corneum and migrated further into the dermis or traveled to distal organ sites (Benn et al., 2011; Gopee et al., 2009; Wu et al., 2009). The

fate of these NPs, when applied to human skin, is still not completely understood, however. In particular, the damage to resident fibroblasts that are numerous and most capable of immune excitation is poorly understood.

Other specific cases of dermal nanoparticle penetration have been documented. For example, it has been concluded that quantum dots can penetrate through the epidermis into the dermis, especially with flexing of the skin or by way of hair follicle (Mortensen et al., 2008; Zhang and Monteiro-Riviere, 2008). Microscopy from these publications revealed that a considerable portion of the dose penetrated to the dermis. Silver is currently being utilized as an antimicrobial agent in many dermal applications and has been found to penetrate both intact and damaged skin (Filon et al., 2009; Samberg et al., 2010). Titanium dioxide, a common ingredient in sunscreens and cosmetics, is generally recognized as safe for dermal exposure. However, while most titanium dioxide studies involving healthy skin report an absence of penetration, this may not necessarily be the case with damaged skin (Mortensen et al., 2008; Senzui et al., 2010) and the realistic exposure may be perpetuated by mechanical flexing, irritant detergents, and chemicals (Filon et al., 2006; Nielsen et al., 2007) or repetitive application (Wu et al., 2009).

Imbalances resulting from the production or presence of excess reactive oxygen species (ROS) plays an important role in numerous pathologies, such as cancer and aging (Droge, 2002; Halliwell, 2007; Halliwell, 2009; Toyokuni and Akatsuka, 2007). It is widely accepted that an excess of ROS is damaging to cellular components, including nucleic acids, proteins and lipids, thereby increasing the likelihood of apoptosis or

necrosis (Dean et al., 1997; Finkel and Holbrook, 2000). Moreover, ROS causes DNA damage, specifically DNA double strand breaks (DSBs), which are considered the most severe type of nuclear lesion (Droge, 2002; Halliwell, 2009; Thannickal and Fanburg, 2000).

Many proteins are involved in maintaining the cellular genomic integrity. Although maintaining this integrity is essential to avoid cancer initiation, limited DNA damage may be tolerated by the cell through a system of repair mechanisms. Should repair pathways fail, replication of damaged DNA may induce changes in the genetic sequence inherited by the daughter cells. Inability to maintain the genomic material may lead to accumulation of DNA damage. Loss of genome integrity further leads to changes in gene expression, resulting from deletions or duplications. Several different repair pathways, equipped with precisely-tuned sensing mechanisms, are present in eukaryotic cells and specific to the type of damage that is present.

Induction of DNA damage or replicative stress triggers a complex network of proteins known collectively as the DNA damage response (DDR). DNA damage is recognized by sensor proteins that recruit and activate transducer and effector or mediator proteins, inducing those which control cell cycle progression (Petrini and Stracker, 2003). This signaling cascade may induce cell cycle arrest to allow time for DNA repair or cell death via apoptotic mechanisms.

DSBs can lead to phosphorylation of H2AX as part of the DNA damage response (Hanasoge and Ljungman, 2007). Histone H2AX, a variant histone that represents approximately 10% of the total H2A histone proteins in normal human fibroblasts, is

required for checkpoint-mediated cell cycle arrest and DNA repair following double-stranded DNA breaks (Yuan et al, 2010) The phosphorylation signal on histone H2AX functions as a scaffold for the recruitment of repair factors to the site of the strand break (Elvers, 2011). The phosphorylated form of H2AX is denoted as γ-H2AX.

Both ATM and ATR are known to phosphorylate BRCA1, as well as p53 (Cortez et al., 1999; Siliciano et al., 1997; Tibbetts et al., 1999), allowing for nucleotide excision repair (NER) to occur (Ford and Hanawalt, 1995, 1997). But the DDR pathway can also function independently of p53. The p38 MAPK pathway is activated in response to a variety of environmental stressors (UV, ionizing radiation, and oxidative stress), as well as inflammatory cytokines (e.g. TNFα) (Zarubin and Han, 2005). Interestingly, although activation of the p38 MAPK pathway by cytokines and receptor ligands normally leads to cell differentiation, activation of p38 MAPK through environmental stress can mediate cell death. In response to DNA damage stimuli that induce DSBs, it has been shown only within the last decade that activation of p38 MAPK can lead to the induction of a G2/M cell cycle checkpoint through p53-dependent and independent mechanisms (Bulavin et al., 2001; Kurosu et al., 2005; Mikhailov et al., 2005; She et al., 2001; She et al., 2000; Thornton and Rincon, 2009). Specifically, p38 phosphorylates CDC25B and CDC25C via MK2, which induces cell cycle arrest after UV exposures (Manke et al., 2005) and other DNA damaging agents (Reinhardt et al., 2007). Involvement of p38 in the DDR has been shown with both single-walled carbon nanotubes (Pacurari et al., 2008) and silver nanoparticles (Eom and Choi, 2010). This is the first body of work,

however, that outlines the DDR pathway mechanism in such detail for CeO_2, TiO_2, and ZnO.

Few studies have been published which investigate the ability of CeO_2, TiO_2, or ZnO to cause DNA damage (Auffan et al., 2009b; Prasad et al., 2009; Sharma et al., 2011; Trouiller et al., 2009). As mentioned before, this data is fairly inconsistent and needs further investigation. More specifically, additional information is needed regarding the mechanism by which these particles exert DNA damage, if at all. Trouiller et al reported that mice given Degussa P25 TiO_2 in drinking water gave rise to γ-H2AX-positive cells, but at high doses of 50-500 ppm, among which micronuclei formed at the highest 500 ppm concentration (Trouiller et al., 2009). Another study using TiO_2 and ZnO in a dermal context found that their particles could catalyze oxidative damage to DNA (determined via the comet assay) in cultured human fibroblasts (Dunford et al., 1997). Sharma et al also reported significant DNA damage from comet assay results in primary human keratinocytes with 14 ppm ZnO (Sharma et al., 2011). Auffan et al found that, in human dermal fibroblasts, a concentration as low as 6 ppm could induce significant SSBs and binucleate cells (Auffan et al., 2009b). Furthermore, a study of the mechanistic effects of DNA damage response is needed on a more detailed level, while considering the nanoparticle physicochemical property influences.

Several studies have shown recently that some nanoparticles can cause cell cycle arrest in response to DNA damage. For example, G1 arrest was observed in mouse lung epithelial cells exposed to C60 and SWCNT (Jacobsen et al., 2008), and carbon black coated with benzo(a)pyrene gave rise to S-phase arrest in human lung epithelial cells

(Mroz et al., 2007). Additionally, AshaRani et al. reported that starch-coated silver NPs induced concentration-dependent G2/M phase arrest and DNA damage in human glioblastoma cells and fibroblasts (AshaRani et al., 2009). Silver NPs were also found to induce S and G2/M phase arrest in Jurkat T cells (Eom and Choi, 2010), but G1 arrest in RAW264.7 macrophages (Park et al., 2010) using similar concentrations of nanomaterials. Additionally, SiO_2 NPs induced G2/M arrest in human embryonic embryo cells (Wang et al., 2009). A perturbation of the cell cycle associated with an accumulation of cells in S-phase leading to cell death, is typical of compounds inhibiting DNA synthesis (Binková et al., 2000; Black et al., 1989). Eukaryotic cells enter mitosis via cdc2 kinase activation, a process which includes cyclin binding and phosphorylation of cdc2 at Thr161 (Atherton-Fessler et al., 1994). However, activation of cdc2 during progression into mitosis requires the critical regulatory step of *dephosphorylation* of cdc2 at Tyr15 and Thr14 (Norbury et al., 1991). Therefore, cells arrested or partially arrested in the S-phase leading up to the G2/M phase will express higher levels of p-cdc2 (Tyr15).

This work is an effort to elucidate the DDR mechanism potential in a dermal model exposed to three metal oxide nanomaterials, while considering the influence of physicochemical characteristics of the nanoparticles. We hypothesize that smaller particle agglomerates and their corresponding large zeta potentials will generate more ROS-driven DNA damage, as compared to nanoparticles which have agglomerated more severely. In this study, changes in viability and protein expression are measured, as well as differences in ROS generation, resulting DNA damage and cell cycle arrest. These

studies examining the toxicological effects stemming from nanoparticle exposure are examined utilizing an *in vitro* system to model human health effects.

4.2 Methods

4.2.1. Nanoparticle characterization

Cerium oxide (Sigma Aldrich, St. Louis, MO), titanium dioxide (Evonik, Parsippany, NJ), and zinc oxide (Sigma Aldrich) hydrodynamic diameter and zeta potential were measured using a Zeta Sizer Nano Series ZEN 3600 Spectrometer (Malvern Instruments Ltd, Malvern, Worcestershire, UK). Particle characterization was performed on the particles suspended in Milli-Q ultrapure water (18.2 mΩ), as well as in DMEM supplemented with 10% FBS at 0, 24, and 48 h time points. Manufacturer's reported primary particle size was <25 nm, 21 nm, and <100 nm for CeO_2, TiO_2, and ZnO, respectively. TEM analysis was done to determine the primary particle size of the three particle types. BET analysis using an accelerated surface area and porosimetry analyzer was employed to determine the surface area of the three particle types (Micromeretics Instrument Corporation, ASAP202, Norcross, GA). Prior to analysis, samples were degassed at 110°C for 2 h.

4.2.2. Cell culture and experimental dosing

Cryopreserved primary human dermal fibroblasts (HDF) cells (PCS-201-010, ATCC, Manassas, VA) were cultured in Dulbecco's Modified Eagle's Medium supplemented with 10% FBS (Gibco, Austria). Media was supplemented with an

antibiotic cocktail consisting of penicillin, streptomycin, and amphotericin (Sigma-Aldrich). Incubation took place at 37°C with humidity and 5% CO_2. Cells were grown to 80% confluency in well plates, then exposed to nanoparticles (20 ppm final exposure concentrations) or untreated for a negative control. Cells treated with nanoparticle suspensions were very briefly exposed to light in the cell culture hood at the points of exposure and harvesting. Cellular incubations with nanoparticles took place in the dark.

4.2.3. Cell viability

HDF cells were cultured in 24-well plates, as described above. Cells were then exposed to CeO_2, TiO_2, or ZnO to give final well concentrations of 0, 10, 50, 150, 200 or 500 ppm to generate dose-response data. Cells treated for 24 or 48 h were rinsed three times, trypsinized, and resuspended in cell culture media. Percentages of viable cells were measured by mixing equal volumes of cell suspension and trypan blue stain, followed by membrane permeability-based counting in an automated cell counter (Countess, Invitrogen). Viability experiments were done in quadruplicate. A student's t-test was employed to calculate significant change in viability, as compared to the untreated control samples.

4.2.4. ROS generation

Intracellular oxidant production was measured after incubation with 20 ppm cerium oxide, titanium dioxide, or zinc oxide nanoparticles at 1, 6, and 24 hrs. Briefly, cells in 96-well plates were incubated with 200 μM non-fluorescent DCFH-DA (2',7'-

dichlorfluorescein-diacetate) in DMEM with 10% FBS for 30 min, then rinsed. Freshly prepared nanoparticle suspensions in new media were added to the cells. The cells were rinsed twice in PBS before reading in DPBS. Hydrogen peroxide was utilized as a positive control at a concentration of 200 μM. Relative fluorescence of the enzyme-cleaved DCFH molecule was determined in a fluorescence microplate reader (BioTek Synergy MX, Winooski, VT) utilizing an excitation/emission spectra of 480/530 nm. All responses were reported as a percentage of untreated control cells. Experiments were carried out with eight replicates per nanoparticle type. Additionally, separate plates of cultured and treated cells were imaged after 1 h exposures. Cells were imaged at a total magnification of 200X with an Olympus IX71 inverted fluorescence microscope (Center Valley, PA). Images were processed with Olympus CellSens software.

4.2.5. Protein expression alteration

HDF were cultured in the same conditions as above. Nanoparticle-treated and untreated cells were washed in ice cold 1X PBS, then protease inhibitor cocktail (Sigma-Aldrich) and high salt lysis buffer were added to wells. Protein was isolated by collecting supernatant via centrifugation. Samples were loaded into 6-12% SDS-PAGE gels and run at 120 mV. Gels were transferred to PVDF membranes, which were blocked in 5% milk or BSA/PBST and incubated in primary antibody solutions overnight at a concentration of 1:1000: p-p38, (Cell Signaling Technology Danvers, MA), HMOX-1, (Santa Cruz Biotechnology, Santa Cruz, CA), superoxide dismutase-1 (SOD1), (Cell Signaling Technology), p-p53, (Cell Signaling Technology), p-cdc2, (Cell

Signaling Technology), or H2AX, (Cell Signaling Technology). Secondary antibody (Goat, anti-mouse or anti-rabbit, 1:5000, Santa Cruz) was prepared in fresh 5% milk or BSA/PBST solution and incubated at room temperature. Immobilon™ Western Chemiluminescent HRP substrate (Millipore, Billerica, MA) was added to membranes and film exposures were taken. β-actin, 1:10,000 (Sigma, St. Louis, MO) was used as a loading control. Blots shown are representative of several independent experiments.

4.2.6. Comet assay

Primary HDF were cultured as explained above and exposed to 20 ppm cerium oxide, titanium dioxide, or zinc oxide nanoparticles for 24 h. The Comet assay was then conducted under alkaline conditions. Briefly, treated cells were washed, trypsinized, and suspended in agarose before being placed onto comet assay slides. Slides were then immersed in pre-chilled lysis solution for 30 min, then placed in alkaline unwinding solution consisting of 200 mM NaOH and 1 mM EDTA. Slides were then drained and electrophoresed for 40 min at 220 mA. Slides were rinsed thoroughly in water, followed by a wash in 70% ethanol. Slides were allowed to dry, then SYBR green was directly applied to wells. SlowFade Gold (Invitrogen, Calsbad, CA) was also applied and allowed to cure in the dark for 24 h to stabilize fluorescence for imaging. Seventy images from each sample type were selected for the experiment, which was carried out in duplicate. Cells were imaged at 200X total magnification with an inverted fluorescence microscope (Olympus IX71, Center Valley, PA). DNA damage was expressed as the tail moment using an image analysis computerized method

(CometScore, TriTek Corporation, Sumerduck, VA). A student's t-test was employed to calculate significant changes in DNA damage, as compared to the untreated control samples.

4.2.7. Immunocytochemistry

HDF cells were cultured on sterile coverslips in 6-well plates and exposed identically to the viability experiments described in 2.3. Double strand break inducer, etoposide, was utilized as a positive control (10 μM) for comparison purposes. Rinsed cells were then fixed in 4% paraformaldehyde. Cell membranes were permeabilized with a 0.25% (v/v) Triton X-100/PBS solution. Cells were blocked in 1% BSA/PBST with 0.3M glycine for 30 minutes, then incubated in a 1:500 primary antibody dilution (gamma-H2AX, CellBiolabs) with 1% BSA/PBST for 1 hr. Goat anti-rabbit 647 AlexaFluor labeled secondary antibody (Invitrogen, A21244) in 1% BSA/PBST was used at a 1:4000 dilution for 1 hr with all samples. Cells were rinsed several times and counterstained with 400nM DAPI for 1 min. Coverslips were mounted onto glass slides with a drop of ProLong SlowFade (P36934, Invitrogen). Slides were imaged at a total magnification of 600X with an Olympus IX71 inverted fluorescence microscope (Center Valley, PA). Images were processed with Olympus CellSens software.

4.2.8. Cell cycle alteration

To determine the potential presence and location of cell cycle perturbation after nanoparticle exposures, HDF cultured to 80% confluency in 6-well plates were treated

with 20 ppm nanoparticle suspensions for 6 h or 24 h. Both nanoparticle-treated cells and control cells treated with an equal volume of Milli-Q water were collected via trypsinization, centrifuged, and suspended in PBS. Cells (1×10^6) were fixed in 70% ethanol for two hours on ice, then held at -20°C overnight before suspension in a propidium iodide/Triton X-100 staining solution with RNase A. Flow cytometry was performed using excitation and emission spectra of 488 nm and 585 nm with a FACS instrument (Becton Dickinson FACSCalibur, Franklin Lakes, NJ) for DNA content evaluation. Data was analyzed utilizing DNA content frequency histogram deconvolution software (ModFit LT). Dead cells and aggregates were excluded from analysis by gating cells in a FL2-A versus FL2-W scatter plot.

4.3 Results

4.3.1. Determination of nanoparticle size, agglomeration state, surface charge, and surface area

Dynamic light scattering (DLS) and zeta potential measurements were taken at 0, 24, and 48 h in both water and cell culture media (Table 4.1). Changes in DLS and zeta potential readings over time reveal trends. As zeta potential migrates further from zero (neutral), agglomeration state decreases. The decrease in zeta potential for TiO_2 is not significant enough to prevent agglomeration, however. A sharp drop in ZnO zeta potential (-9.24, -11.05, and -34.00 at 0, 24, and 48 hrs respectively) correlates with decreasing particle size (249.5, 51.57, and 37.89 nm at 0, 24, and 48 hrs respectively), which is represented in Figure 4.1. The significantly negative zeta potential at 48 hrs is

Table 4.1 Nanoparticle characterization reveals trends in toxic capability. Transmission electron microscopy (A-C), dynamic light scattering (D), and zeta potential measurements (E) of 20 ppm CeO_2, TiO_2, and ZnO in water and complete media at 0, 24 and 48 h.

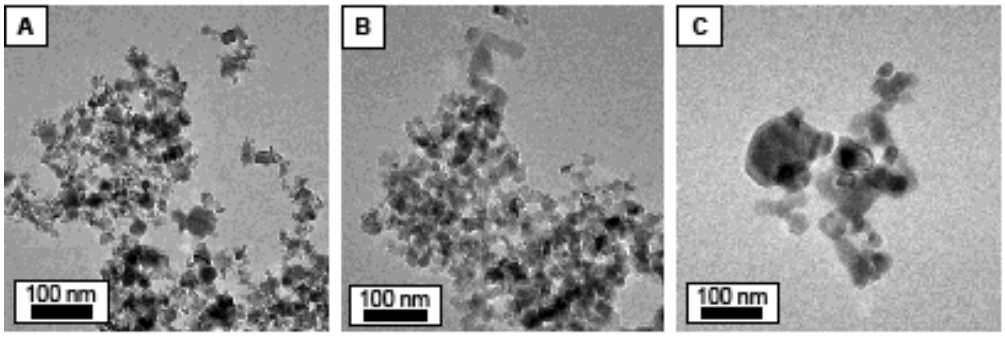

D) Hydrodynamic size as measured by dynamic light scattering

	0 h		24 h		48 h	
	water	*media*	*water*	*media*	*water*	*media*
CeO_2	143.83 ± 5.08	324.53 ± 4.68	890.87 ± 175.75	225.27 ± 7.59	1248.5 ± 577.58	329.43 ± 9.00
TiO_2	767.80 ± 48.25	850.63 ± 50.35	919.47 ± 267.99	321.30 ± 19.14	1118.93 ± 298.74	1130.97 ± 165.71
ZnO	1155.00 ± 163.80	249.50 ± 123.90	118.73 ± 73.19	51.57 ± 3.26	25.77 ± 6.45	37.89 ±15.83

E) Surface charge as measured by zeta potential

	0 h		24 h		48 h	
	water	*media*	*water*	*media*	*water*	*media*
CeO_2	8.64 ± 3.36	-10.80 ± 0.70	-9.89 ± 1.89	-10.83 ± 0.12	-7.37 ± 0.43	-11.10 ± 0.66
TiO_2	0.03 ± 0.03	0.02 ± 0.04	-11.23 ± 0.60	-10.83 ± 0.67	-2.45 ± 8.40	-9.98 ± 0.92
ZnO	-10.18 ± 1.18	-9.24 ± 0.39	-22.97 ± 4.28	-11.05 ± 1.64	-10.23 ± 0.42	-34.00 ± 0.00

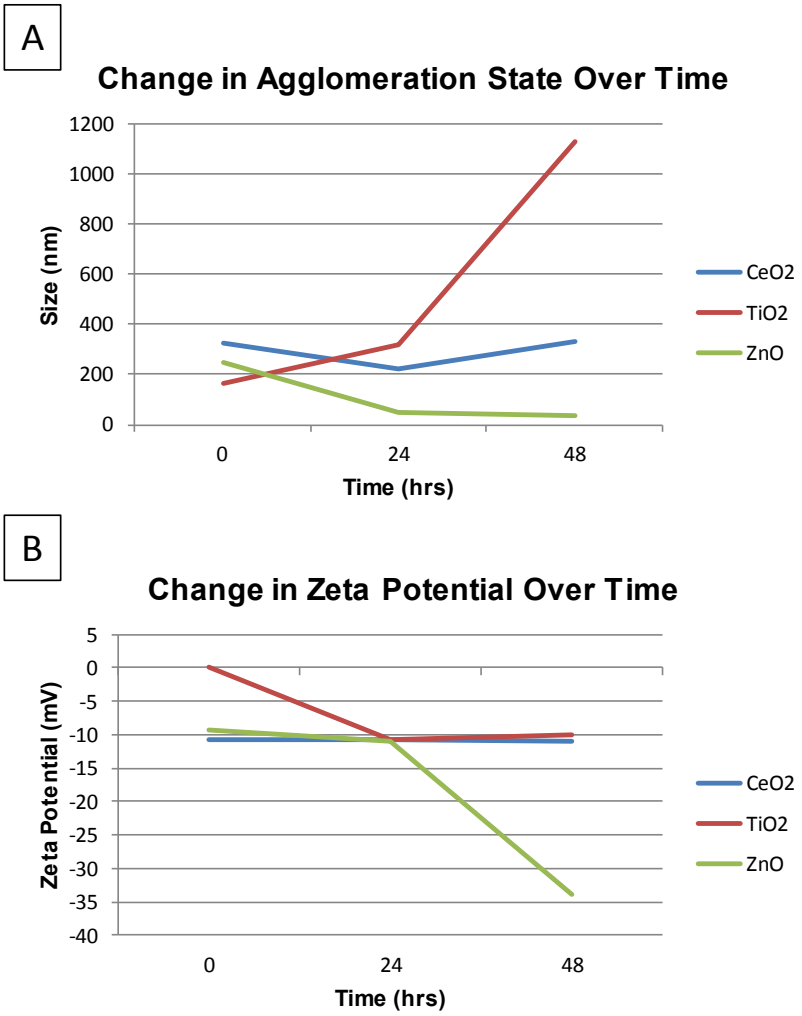

Figure 4.1. Nanoparticle agglomeration state and zeta potential changes over time. Changes in zeta potential (A) and size (B) of 20 ppm CeO_2, TiO_2, and ZnO in media at 0, 24 and 48 hrs. The sharp decrease in ZnO zeta potential (-9.24, -11.05, -34.00 at 0, 24, and 48 hrs respectively) correlates with decreasing particle size (249.5, 51.57, and 37.89 nm at 0, 24, and 48 hrs respectively). The strongly negative zeta potential at 48 hrs is deviated far enough from zero to maintain smaller particle agglomerates.

deviated far enough from zero to maintain smaller particle agglomerates. BET analysis yielded surface area values of 50.441, 59.138, and 11.625 m^2/g for CeO_2, TiO_2, and ZnO, respectively. These values correspond with particle size measured by TEM analysis. Perhaps the most important finding was that CeO_2 and TiO_2 remained severely aggregated over time in complete media, whereas ZnO aggregated initially, but decreased in agglomeration state over time. By 48 h, the hydrodynamic size of ZnO decreased nearly to its primary particle size.

4.3.2. Concentration-dependent cell death

HDF cells treated with CeO_2, TiO_2, and ZnO exhibited dose-dependent (10-500 ppm) cell death, as determined via the trypan blue assay (Figure 4.2). Cell death was most significant with ZnO exposures, followed by TiO_2 and CeO_2 exposures at both 24 and 48 h. For all particle-types, cell viability decreased significantly as a function of nanoparticle dose. Brightfield images, which display the differential results after exposure to these three materials are also provided to show changes in morphology at 6 and 24 h (Figure 4.3).

4.3.3. ROS generation and resulting oxidative stress

To investigate the potential role of oxidative stress as a mechanism of metal oxide toxicity, intracellular oxidant production was measured after incubation with 20 ppm CeO_2, TiO_2, or ZnO nanoparticles. Separate plates of cells were treated and analyzed individually after 1 h exposures (Figure 4.4A). Differences in intracellular

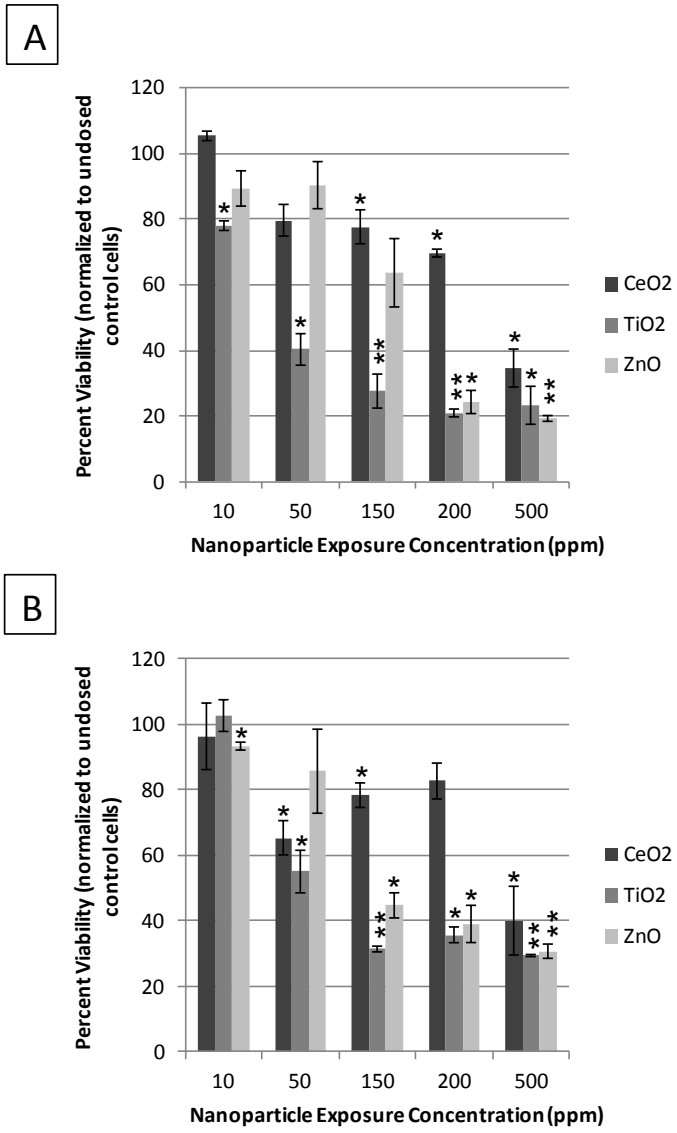

Fig. 4.2. Cell death correlates with increasing nanoparticle exposure. Percent viability after 10, 50, 150, 200, and 500 ppm CeO_2, TiO_2, and ZnO, as determined via a trypan-blue exclusion assay. Measurements were taken at both 24 (A) and 48 h (B) and are normalized to untreated cells. *Statistically significant ($p<0.05$) compared to untreated cells. **Statistically significant ($p<0.001$) compared to untreated cells.

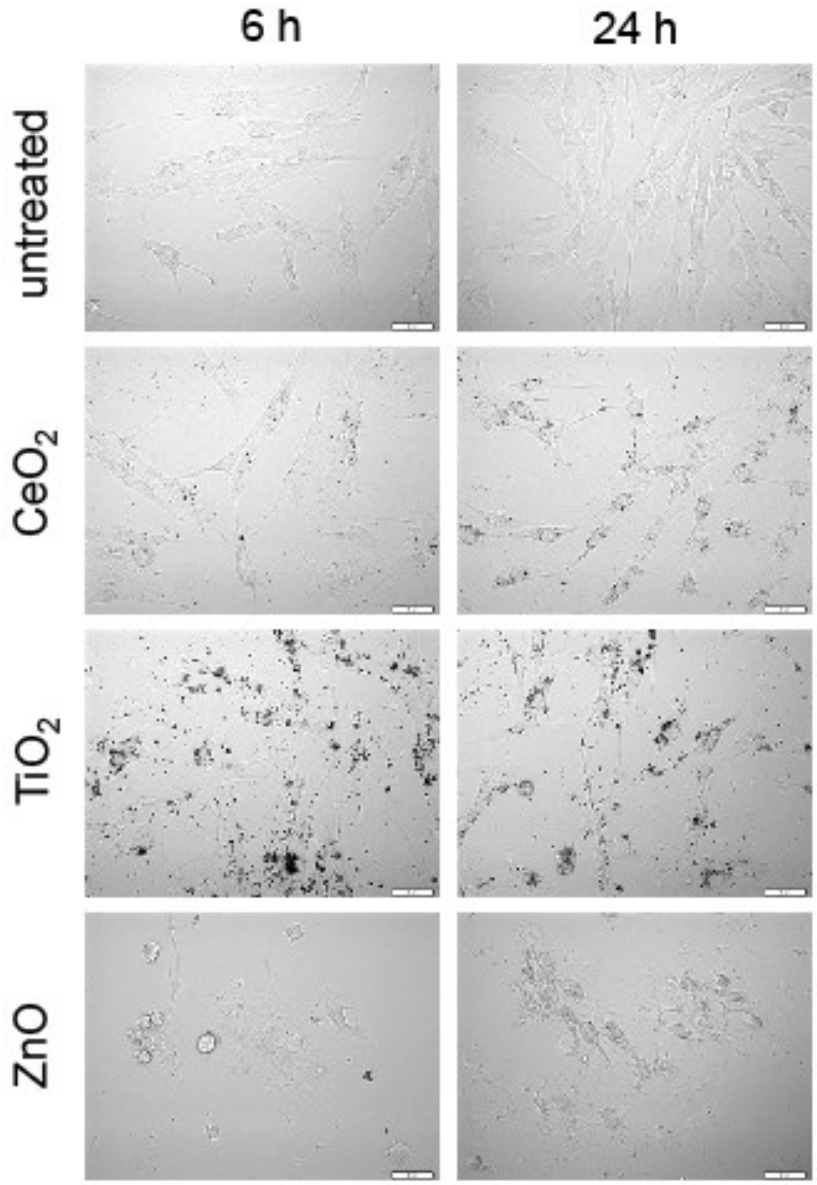

Figure 4.3. HDF morphology differences after nanoparticle treatments. HDF treated for either 6 or 24 h with 20 ppm cerium oxide, titanium dioxide, or zinc oxide reveal differential morphological responses. Scale bar=50µm.

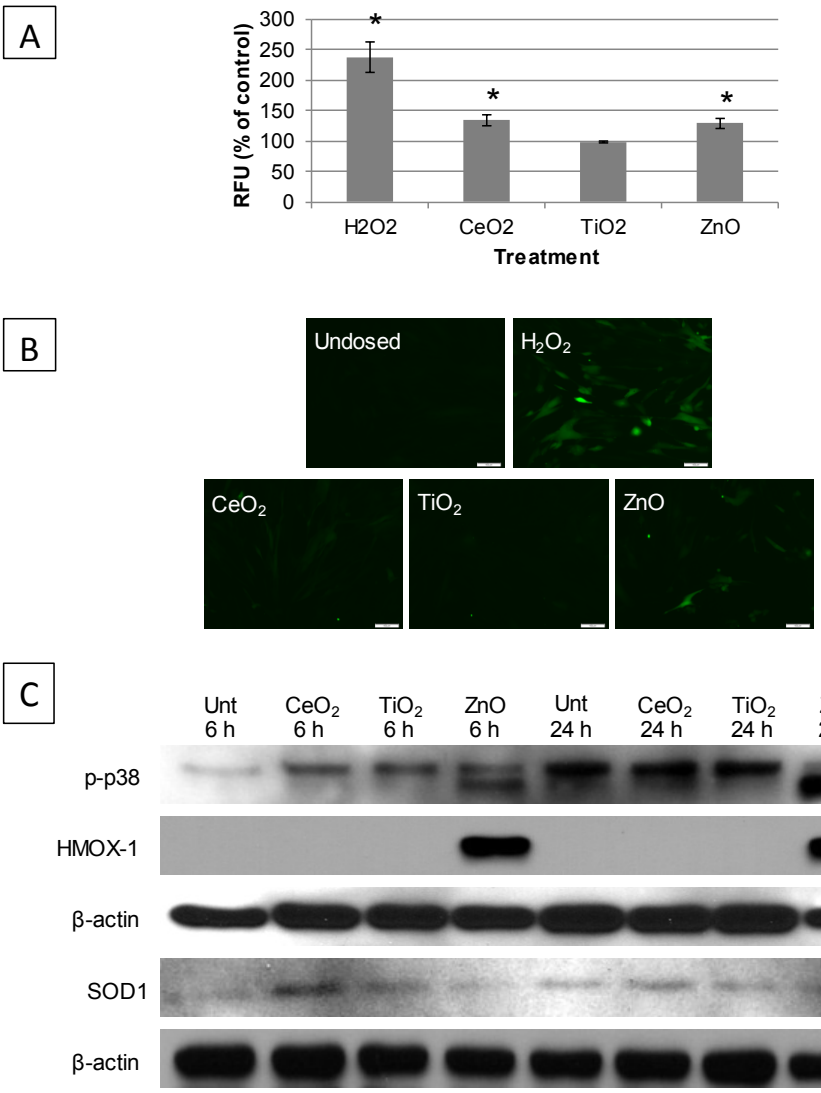

Fig. 4.4. Nanoparticle-driven ROS generation and oxidative stress. Intracellular oxidant production was measured after incubation with 20 ppm cerium oxide, titanium dioxide, or zinc oxide nanoparticles at 1 h (A). Fluorescence images correspond to graph (B). Hydrogen peroxide was utilized as a positive control at a concentration of 200 μM. All responses were reported as a percentage of untreated control cells. *Statistically significant ($p<0.05$) compared to untreated cells. Upregulation of oxidative stress proteins was measured via western blot after 6 and 24 h exposure to 20 ppm CeO_2, TiO_2, and ZnO (C). Phosphorylated p38, HMOX-1, and SOD1 protein levels were assessed in primary HDF cells following these exposures. β-actin served as a loading control. Blots are representative of three identical experiments.

oxidant production were observed with CeO_2 and ZnO exposures, which caused increases in ROS generation, as compared to untreated cells. H_2O_2 (200 μM) was also utilized as a positive control. All treated samples were normalized to untreated cells. Fluorescence was also measured at 6 and 24 h (data not shown), but fluorescence intensity was slightly higher at the 1 h time point. Representative images of cells processed identically to those read photospectrometrically are provided (Figure 4.4B).

Western blot analysis was performed to assess specific perturbation of oxidative stress proteins (Figure 4.4C). HDF were exposed for 6 and 24 h to CeO_2, TiO_2, and ZnO. Oxidative stress, as indicated by an increase in HMOX-1, is upregulated at 6 and 24 h with exposure to ZnO. A similar trend was evident with the phosphorylation of oxidative stress and DNA damage protein, p38, where ZnO induced a distinct isoform of the protein. Induction in lysates at 24 h was similar to untreated cells, except in ZnO-treated cells. SOD1 was upregulated with CeO_2 exposure, as compared to untreated control cells. This finding was most obvious at 6 h.

4.3.4. Nanoparticle induced DNA damage

A combination of single and double stand break DNA damage was measured in a comet assay (Figure 4.5A). HDF cells were exposed to 20 ppm CeO_2, TiO_2, and ZnO. Damage was measured after 24 hrs and is reported as tail moment. An untreated control was included for comparison. ZnO caused the most significant amount of strand breaks. Representative images are included for comparison (Figure 4.5B).

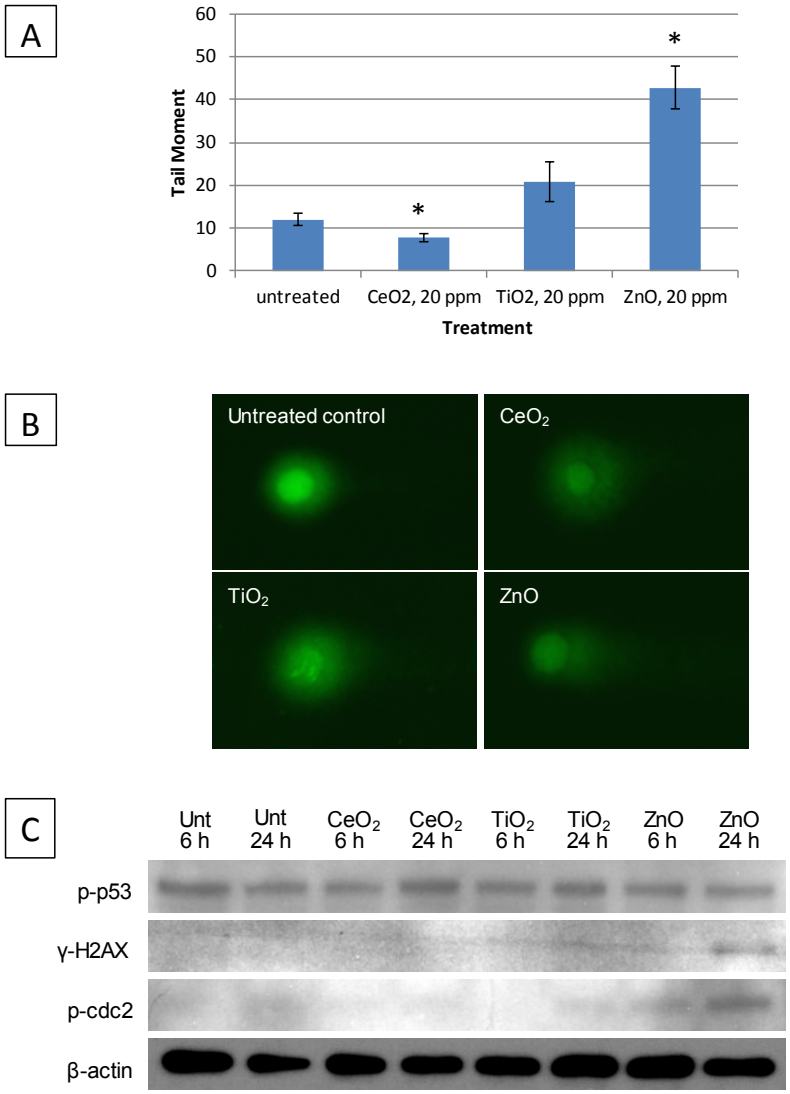

Fig. 4.5. Calculation of DNA strand break damage. Single and double stand break DNA damage was assayed after HDF cells were exposed to 20 ppm CeO_2, TiO_2, or ZnO (A). Cells were analyzed after 24 h exposure in a comet assay. Undosed control cells were included for normalization purposes. Seventy cells were imaged per treatment group. Representative images from each treatment group are included (B). *Statistically significant ($p<0.05$) compared to untreated cells. **Statistically significant ($p<0.001$) compared to untreated cells. Western blot analysis of DDR pathway-related protein expression after 6 and 24 h exposure to 20 ppm CeO_2, TiO_2, and ZnO was performed (C). Activation of γ-H2AX histone variant, as well as phosphorylation levels of p53 and cdc2 were investigated and compared to untreated control cells. β-actin served as a loading control. Blots are representative of three identical experiments.

Western blot analysis was performed to assess specific perturbation of DDR pathway proteins (Figure 4.5C). Cdc2, a marker of cell cycle progression to mitosis is also phosphorylated in both ZnO-treated samples and slightly with TiO_2 treatment at the later time point. The cell cycle is allowed to progress to mitosis when cdc2 becomes dephosphoylated at Tyr15. Therefore, an accumulation of p-cdc2 indicates halting in the S-phase. Specific double strand break repair protein γ-H2AX is only induced with 24 h ZnO treatment. A lack of expression of activated H2AX with the other nanoparticles suggests that ZnO is the only particle type that induces DSBs. This damage pathway is p53-independent, as notable changes in band intensity were absent for this protein at 6 and 24 h. Phosphorylation of p53 was also absent at multiple time points from 0-4 h (data not shown).

Immunocytochemistry in ZnO-treated cells revealed notable DNA double strand breaks, as evidenced by a marked increase in the presence of gamma-H2AX foci in HDF exposed to 20 ppm concentrations at 24 hrs (Figure 4.6). Moreover, foci in ZnO-treated cells were visibly more punctuate, indicating increased condensation of chromatin. Compared to untreated control cells, a slight increase in the number of foci are also present in CeO_2 and TiO_2-treated samples (Figure 4.7).

4.3.5. Cell cycle perturbation

Cell cycle arrest is a critical component of the DDR, as it allows sufficient time for DNA damage repair to occur before progression into mitosis, thereby protecting genome integrity. We examined the effect of three metal oxides on the cell cycle using

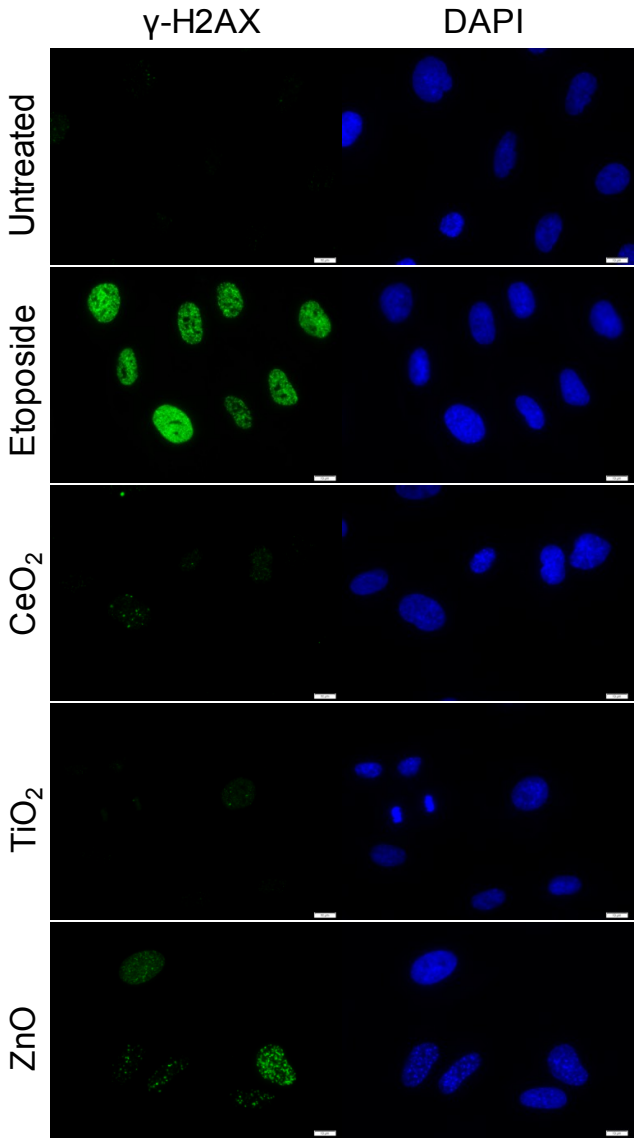

Fig. 4.6. DNA strand break damage, as determined by immunocytochemistry. Differential γ-H2AX expression in HDF treated with 20 ppm nanoparticles for 24 h. DAPI was used as a nuclear control. Etoposide was utilized at a concentration of 100 μM for 1 hr as a positive control. Untreated cells were also included for comparison purposes. ZnO-treated cell images indicate the most significant double strand break damage compared to untreated control cells. *Statistically significant ($p<0.05$) compared to untreated cells. **Statistically significant ($p<0.001$) compared to untreated cells. Scale bar = 10 μm.

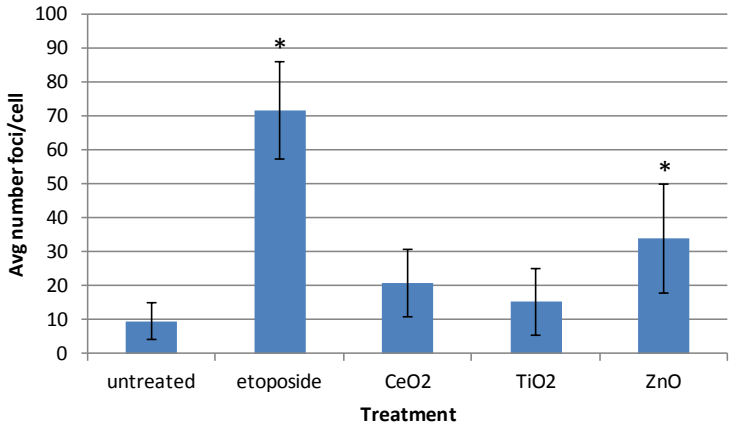

Figure 4.7. Average number of gamma-H2AX foci per cell. Differential γ-H2AX expression in HDF treated with 20 ppm nanoparticles for 24 h are compared here to untreated and positive control-treated cells. Etoposide was utilized at a concentration of 100 μM for 1 hr as a positive control. Of the three nanoparticle types tested, ZnO-treated cells indicated the most significant double strand break damage compared to untreated control cells. *Statistically significant ($p<0.05$) compared to untreated cells.

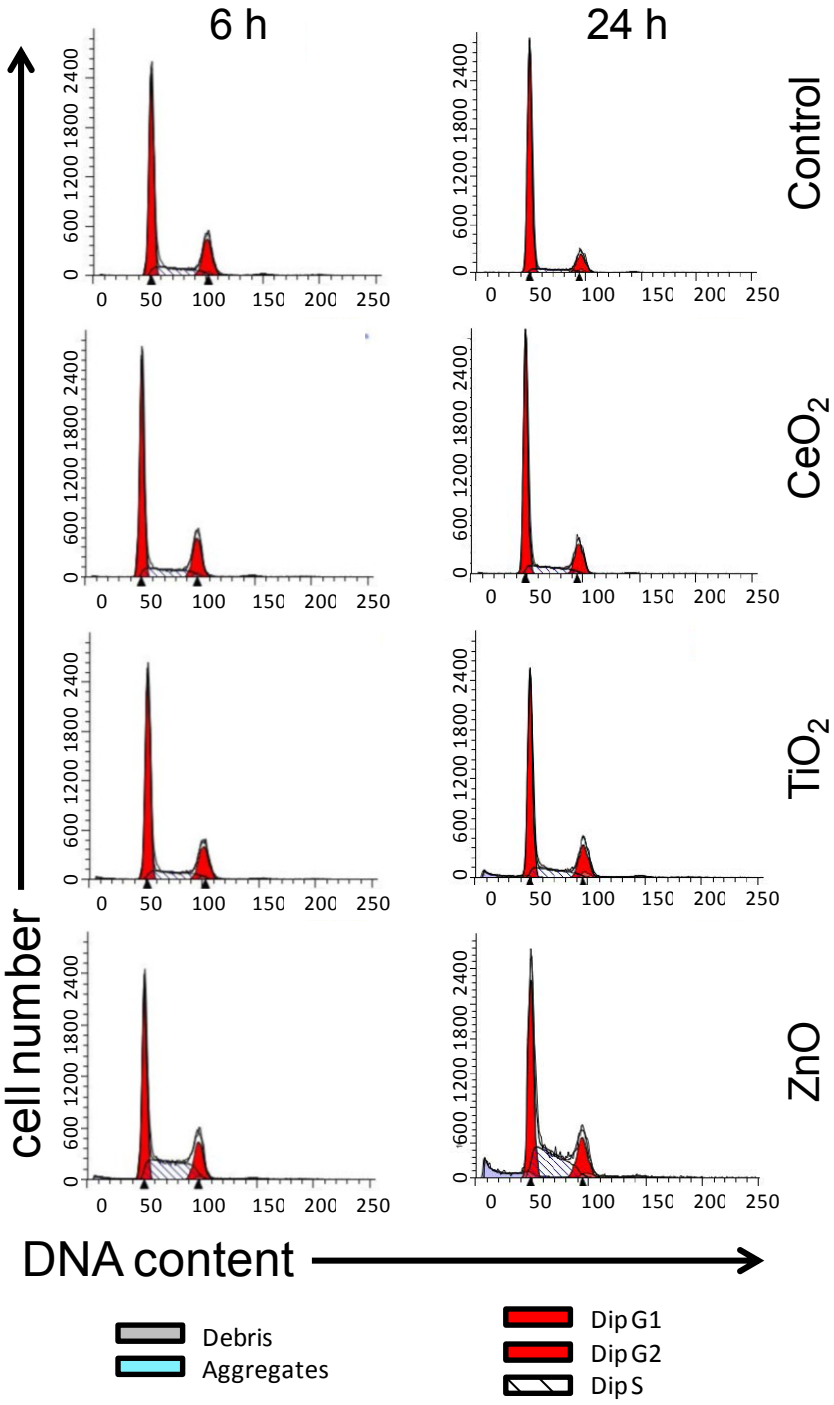

Fig. 4.8. Cell cycle perturbation histograms. Number of cells counted in each phase of the cell cycle is represented above for HDF dosed at 6 and 24 hrs with 20 ppm CeO_2, TiO_2, or ZnO. Untreated control samples are included for comparison.

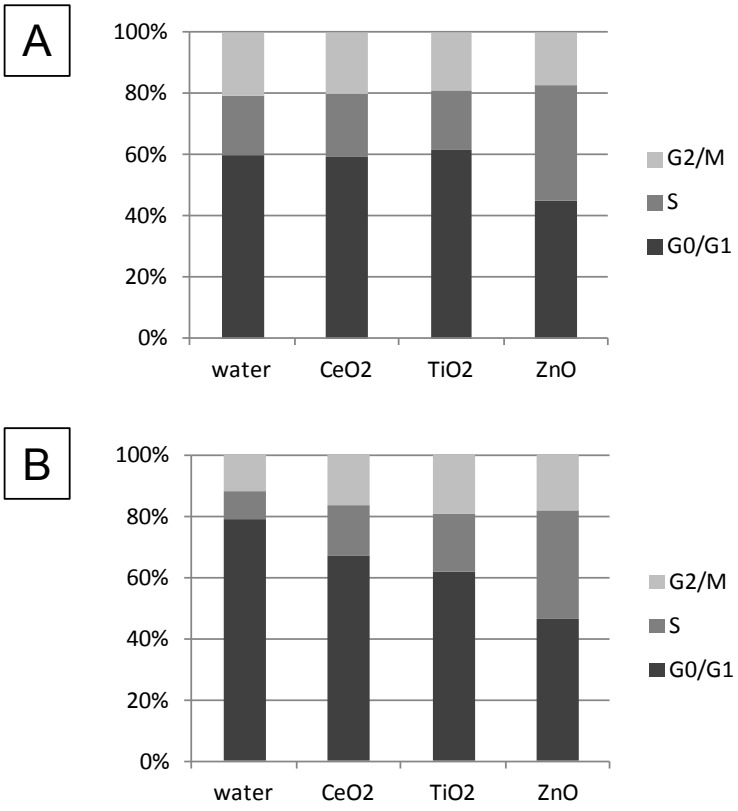

Fig. 4.9. ZnO induces S-phase arrest. Changes in cell cycle were assayed via FACS after exposure to 20 ppm CeO_2, TiO_2, or ZnO for 6 (A) and 24 (B) h. Following nanoparticle treatments, cells were ethanol-fixed and stained with propidium iodide for analysis.

propidium iodide coupled with flow cytometry (Figure 4.8). At 6 h exposure, ZnO induced S-phase arrest in HDF, whereas no changes were observed in CeO_2 and TiO_2-treated cells, in comparison with water-treated cells (Figure 4.9A). After 24 h exposure, ZnO continued to cause S-phase arrest (Figure 4.9B). When compared to untreated cells at this time point, CeO_2 and TiO_2 caused less severe arrest. At the later time point, percentages of cells in G0/G1, S, and G2/M phases were 78.9, 9.3, and 11.9 respectively for water-treated cells, 67.3, 16.1, and 16.6 for CeO_2-treated cells, 61.8, 18.9, and 19.3 for TiO_2-treated cells, and 46.4, 35.8, and 17.9 for ZnO-treated cells. S-phase arrest is indicative of DNA damage and consistent with repair taking place.

4.4 Discussion

While nanomaterials possess many desirable characteristics, the possibility of DNA damage response in dermal cells exposed to nanoparticles needs further evaluation due to the fact that humans are increasingly exposed to products containing metal oxide particles on the nanoscale. Differences in the potential responses between particle types also need to be investigated since the physicochemical properties of each nanomaterial differ greatly, which may influence the resulting biological response upon exposure. Most needed is a mechanism by which researchers can correlate biological damage with specific properties of the materials in question. This is the first study to analyze the DDR in dermal cells exposed to these three metal oxides, while considering the role of nanoparticle physicochemical characteristics in the postulating of nanoparticle-induced genotoxic capability.

Our nanoparticle characterization revealed distinct differences between particle types, which assist in explaining the differential toxicity that was seen throughout the experiments carried out. ZnO remained close to its primary particle size in media over time, while CeO_2 and TiO_2 became severely aggregated over time. Aggregation state of these materials closely correlated with the zeta potential exhibited at each time point. ZnO became increasingly negative, compared to the other two particle types, decreasing particle-particle interaction and possibly increasing the likelihood of biological interactions. Additionally, Zn^{2+} ions are known to dissociate from ZnO in dermal exposure scenarios and this fact is noteworthy since zinc is an essential trace element capable of competing for cell surface receptors and initiating cell death pathways when in excess . In fact, the presence of "free" zinc ions may be the cause of ROS-driven cytotoxicity, rather than the presence of zinc-containing nanoparticles (Song et al., 2010).

Interestingly, cellular zinc depletion induces apoptosis due to increased oxidative damage and activity of pro-apoptotic enzymes (Truong-Tran et al., 2001; Zalewski et al., 1993), which is thought to be caused by decreased PARP-1 catalyzed base excision DNA repair (Mocchegiani et al., 2000). However, it has also been shown that an excess of zinc causes toxic free radicals and apoptosis or necrotic cell death (Fraker and Telford, 1997; Kim et al., 1999; Watjen et al., 2002).

CeO_2 caused oxidative stress, as the DCFH-DA assay and SOD1 protein results suggest, but significant DNA damage did not occur at this concentration. This may be due to the fact that CeO_2 did not remain in its primary particle size and likely did not

break down into ions within the cell, as ZnO has been reported to do (Miao et al., 2010; Xia et al., 2008). TiO_2 also induced some level of oxidative stress, as indicated by a slight increase in DCF fluorescence detection, but no significant DDR occurred at the concentration and time point we assessed. It has been documented that the increased surface area of nanoparticles generates increased levels of ROS, as compared to their compositionally identical bulk counterparts (Nel et al., 2006).

Figure 4.10 outlines the DDR after exposure to nanoparticles. DNA strand breaks activate ATM and/or ATR, which initiate the DDR cascade. We have found that p38 is activated with ZnO exposures, leading to an accumulation of phosphorylated cdc (Tyr15), which further indicates cell cycle arrest. Our finding that S-phase arrest was induced by ZnO is consistent with the remainder of our results indicating significantly increased levels of ROS production, decrease in viability, protein expression, and DNA damage levels. Interestingly, none of the materials tested induced the better-studied p53 pathway, which is known to play a role in the DDR and apoptosis. P21 was also unaffected at time points from 0-4 h, 6 h, or 24 h (data not shown). As previously stated, p38 has been shown to act independently of p53 in inducing cell cycle arrest. Here, we elucidate a mechanism behind the DDR in primary HDF exposed to low concentrations of CeO_2, TiO_2, and ZnO nanoparticles.

Eom and Choi recently published results of studies in Beas-2B human bronchial epithelial cells treated with nano-sized silver, where they found activation of the p38 pathway leading to S and G2/M phase cell cycle arrest with H2AX phosphorylation at 12 and 24 h in silver (Eom and Choi, 2010). The same group also published findings in

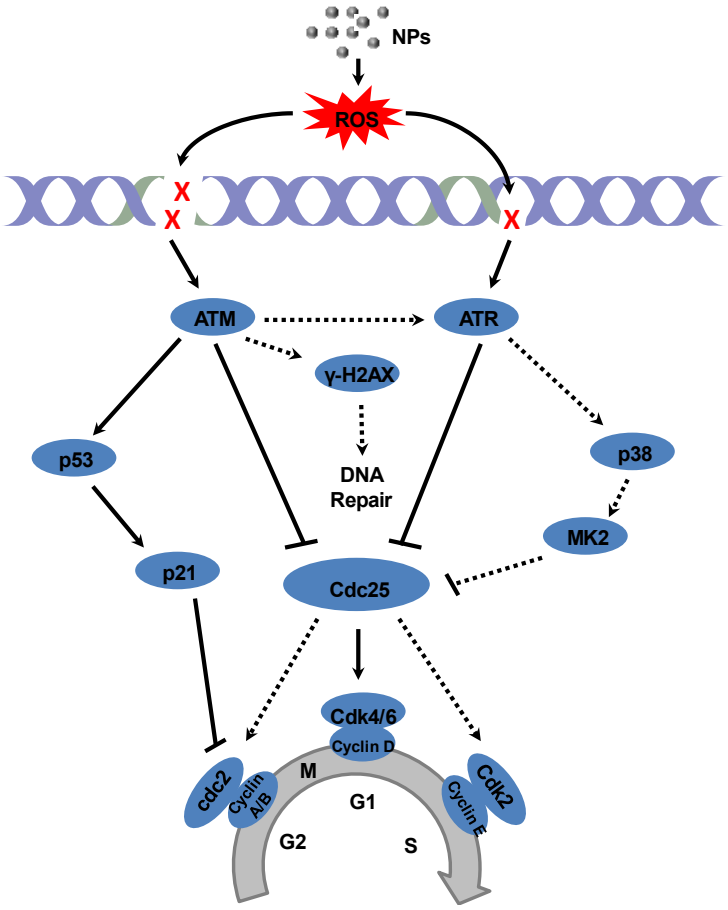

Fig. 4.10. Proposed DNA damage response schematic. Proposed schematic of HDF DDR pathway and related protein involvement after nanoparticle exposures.

2009 of ROS-induced p38 phosphorylation in Beas-2B cells after CeO2 exposures, but did not investigate DNA damage potential (Eom and Choi, 2009a). Here, we have assessed ROS generation and stress, as well as DNA damage potential in primary human cells resulting from exposure to three metal oxides found in commercially available products.

Although ZnO has been found to be superior to TiO_2 as a sunscreen and cosmetic ingredient since it is more protective against long-wave UVA and is less opaque upon application (Pinnell et al., 2001), it may be more damaging to DNA in the underlying dermal tissue than TiO_2 or CeO_2 at the concentration tested. While many have found penetration of similar nanoparticles to be limited to the stratum corneum or only occasionally reaching the viable epidermis (Baroli et al., 2007; Cross et al., 2007; Zvyagin and Zhao, 2008), others have found that exposures over time or factors such as flexing of the skin before application of such particles dramatically increases the depth and amount of translocation (Gopee et al., 2009; Rouse et al., 2007; Tinkle et al., 2003; Wu et al., 2009). It is quite common for metal oxide nanomaterials to be applied daily in the form of cosmetics or sunscreens, which fill the hair follicle and are then less likely to be removed during skin cleansing. It is critical that *in vivo* studies considering such realistic, confounding exposure scenarios continue, keeping in mind the potential for ROS-driven DNA damage with metal oxide exposures.

Salient points to be learned from this research:

- *NP characterization suggests toxicity can be at least partially predicted by trends in zeta potential and agglomeration state.*

- *ROS generation did not always lead to significant DNA damage.*
- *ZnO induced the most serious DDR with halting of the cell cycle in S-phase.*
- *DDR was p53-independent, but involved p38 in altering the cell cycle in primary HDF.*

Questions remaining unanswered:

- *Does nanoscale ZnO penetrate through the stratum corneum?*
- *Can properties of potentially toxic nanoparticles, such as surface charge or surface composition, be altered to allow for their safe use in dermal applications?*

CHAPTER V

MITIGATION OF QUANTUM DOT CYTOTOXICITY BY MICROENCAPSULATION*

5.1 Introduction

Nanoscale materials are promising contenders for diagnostics, therapeutics, and imaging agents due to their size, functionality, and unique optical properties. Many of the proposed biomedical applications for nanomaterials revolve around their employment as targeted drug delivery vehicles in the circulatory system (Emerich and Thanos, 2006; West, 2009). Another potential biomedical application of nanomaterials includes their incorporation into medical implants, such as devices placed in the subcutaneous tissue or even as functional elements of "smart" tattoo-like biosensors (McNichols and Cote, 2000; McShane, 2002; McShane, 2006). Such concepts require engineered structures and materials with the desired function (e.g., optical sensing) within a fully biocompatible and/or biodegradable platform (McShane, 2006). As an example, many biosensors require mobility of sensing reagents—the sensors/reagents must be able to freely associate and dissociate, while being physically constrained to enable continuous use in one location (McShane and Ritter, 2010; McShane, 2006). Inorganic nanoparticles offer unique properties that enable innovative biosensing

---

*Reprinted with permission from "Mitigation of Quantum Dot Cytotoxicity by Microencapsulation" by Romoser, et al., 2011. *PLoS ONE*, 6, e22079, Copyright [2011] by Romoser et al.

techniques. However, it is difficult to localize the nanoparticles for long periods of time. Additionally, the prospective use of nano-enabled biosensors for such *in vivo* applications has raised concerns regarding the possible localized and systemic toxicological effects in humans. Mechanistic analyses of these effects in humans are needed when assessing the risks due to the use of nanomaterials in medicine and biological imaging.

QDs with a cadmium selenide core (CdSe) and a zinc sulfide (ZnS) shell remain the most studied, produced, and proposed luminescent nanomaterial. Offering significant advantages for energy transfer-based biosensors, QDs are photobleaching resistant, have high quantum yield, and possess broad absorption/narrow emission bands that are size tunable (Ipe et al., 2005). However, since CdSe/ZnS QDs have been shown to enter living cells (Chang et al., 2006; Duan and Nie, 2007; Jaiswal et al., 2003; Ryman-Rasmussen et al., 2007; Ryman-Rasmussen et al., 2007b; Zhang et al., 2008), their toxicological characterization and mitigation is extremely relevant to nanobiotechnology. It has been shown that the addition of a ZnS outer shell can minimize damage to the cell (Su et al., 2009); however, the potential for substantial damage from leaching cadmium, selenium, and/or excess zinc still exists (Das et al., 2009; Mahendra et al., 2008). In addition, because QDs are intrinsically redox-active, a portion of their toxic potential may also arise from such native properties without regard to their composition, surface properties, or cellular internalization potential. Quantum dots can transfer absorbed optical energy to adjacent oxygen molecules, thus spontaneously generating reactive oxygen species (ROS) such as hydroxyl radical ($^{\bullet}OH$),

superoxide (O^{2-}), and singlet oxygen ($^1O_2$) (Ipe et al., 2005; Przybytkowski et al., 2009; Yu et al., 2006). Further modification of the QD surface with silanes (Gerion et al., 2001), oligomeric phosphines (Kim and Bawendi, 2003), phospholipids (Dubertret et al., 2002), and amphiphilic triblock copolymers (Gao et al., 2004) has been demonstrated as an effective means to further mitigate toxicity by protecting the QD surface from deterioration in biological media. However, these capping agents increase overall QD size enough to preclude efficient energy transfer to an acceptor (Medintz et al., 2005). Therefore, although these bulky capping agents protect the QD from degradation, biosensing schemes requiring intimate contact between QDs and analytes/reagents (e.g., transduction via energy transfer) can incur a loss in biosensor functionality.

As an alternative to protecting individual QDs, microencapsulation provides a means to modulate interfacial interactions between the cells and QDs without the need to deposit bulky surface coatings on the QDs. Our work is separate from a large body of work focused on encapsulating individual QDs, as we are microencapsulating an ensemble of QDs within each polyelectrolyte microcapsule (2.05e10 QDs/microcapsule). It is also noteworthy that the QDs used in this study are microencapsulated within the hollow interior (i.e., void) volume of the polyelectrolyte microcapsule, which should be distinguished from QD entrapment within the polyelectrolyte film itself (Kirchner et al., 2005a) and results in an interaction among the QDs, the solvent, and other molecules that permeate the film. Although the two seem similar superficially, important differences exist with respect to interactions with surroundings and apparently toxicity, as evidenced by our data.

Microcapsules and nanoparticle surface coatings can function as protective layers to prevent or inhibit erosion, oxidation, and leaching of core components; however, the leaching of core components is a central challenge for the microencapsulation field (Parthasarathy and Martin, 1994). Numerous studies have shown that microcapsules synthesized via the layer-by-layer (LbL) process inhibit the release of core components and show promise for the development of new types of nano-enabled biosensors (Almeida et al., 1993; Marchesiello and Genies, 1993; Parthasarathy and Martin, 1994). Even one of the smallest enzymes, trypsin (M_w = 23.3 kDa; corresponding to an average diameter of ~1-3 nm) does not leach from an LbL microcapsule (Parthasarathy and Martin, 1998). The PEI-coated QD materials (termed CdSe/ZnS-PEI) used in this study are ~15 nm in all dimensions and are thus well contained within the microcapsule (Figure 5.1). However, it is important to note that the permeability of the microcapsules to ions, small molecules, and even macromolecules can be tailored in a number of ways, including modulation of the pH (during and post-construction), ionic strength (during and post-construction), solvent (during and post-construction), polymer composition, and shell thickness (Antipov and Sukhorukov, 2004). Therefore, given a sufficiently large disparity in molecular weight/size between the analyte and the QD (or other assay components), a number of strategies can be employed to entrap the sensing assay, while maintaining permeability of ions and small molecules (e.g., the analyte). Again, because the polyelectrolyte microcapsules are hollow, the QDs retain their responsiveness to the environment. Therefore, the purpose of this study was to examine the protective effects

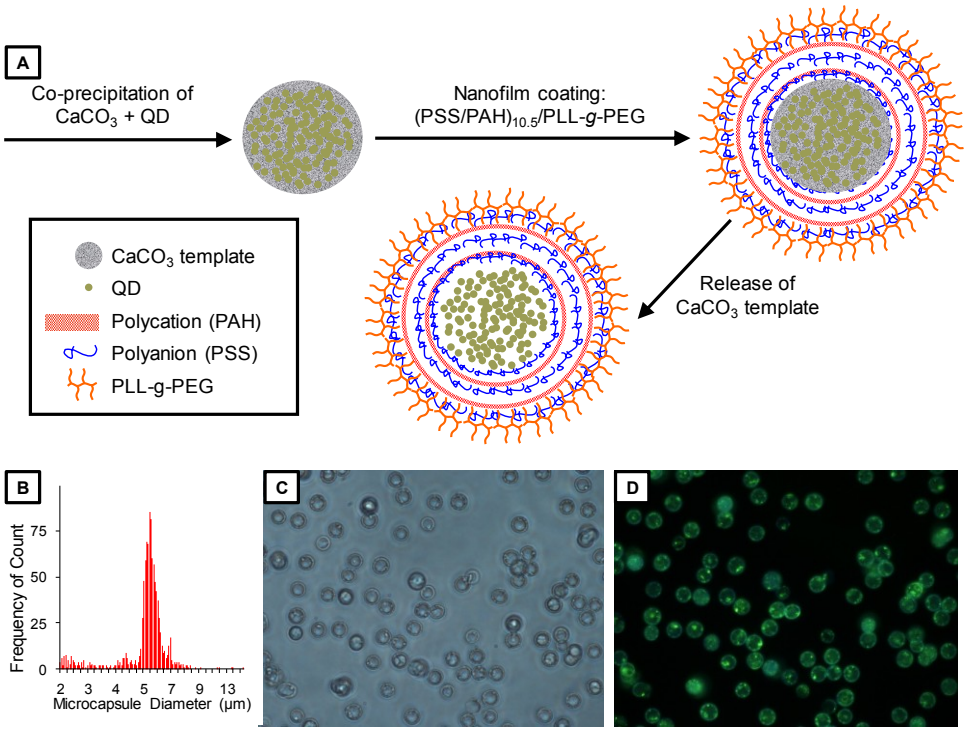

Fig. 5.1. Quantum dot-loaded microcapsule characterization. (A) Schematic representation of the formation of QD-loaded microcapsules. (B) Histogram of the size distribution of QDMCs. (C) Brightfield and (D) fluorescence images of the QDMCs, showing that the microcapsules are monodisperse and contain QDs (ex/em 380/545).

of additional surface constructs, namely polymer microcapsules, in comparison with the toxicological effects of free CdSe/ZnS-PEI QDs.

To more thoroughly mitigate the potential cellular toxicity caused by reported dissociated metal ions (Derfus et al., 2004) or ROS generation from the QDs, we set out to microencapsulate CdSe/ZnS-PEI in an effort to nullify the adverse effects of free QDs on cellular morphology and metabolism, cytotoxicity, and apoptotic or necrotic response (Figure 5.2). Specific to the case of implantable biosensors under epidermal layers of skin, we have developed a model that investigates the potential cytotoxicity, uptake, and apoptotic response of QD-loaded microcapsules (QDMC). Human dermal fibroblasts (HDF), the cells that compose the majority of the viable dermal layer, were exposed to CdSe/ZnS-PEI QDs microencapsulated within PEG-terminated microcapsules comprised of poly(styrene sulfonate) (PSS) and poly(allylamine hydrochloride) (PAH). The near-neutral surface charge of PEG-terminated microcapsules results in minimized contact with cells, providing an excellent biomedical tool, while retaining desirable QD qualities. However, it is important to note that microencapsulating other types of nanoparticles is not only possible, but potentially advantageous. For example, noble metal nanoparticles that possess antioxidative effects (e.g., reactive oxygen species scavengers) might benefit from microencapsulation to prevent cellular internalization, while simultaneously preserving surface-dependent biomimetic properties. Another potential application is the controlled release of a drug from polymeric nanoparticles, wherein the drug to be delivered acts on cell surface receptors and must be delivered extracellularly (e.g., vascular endothelial growth factor).

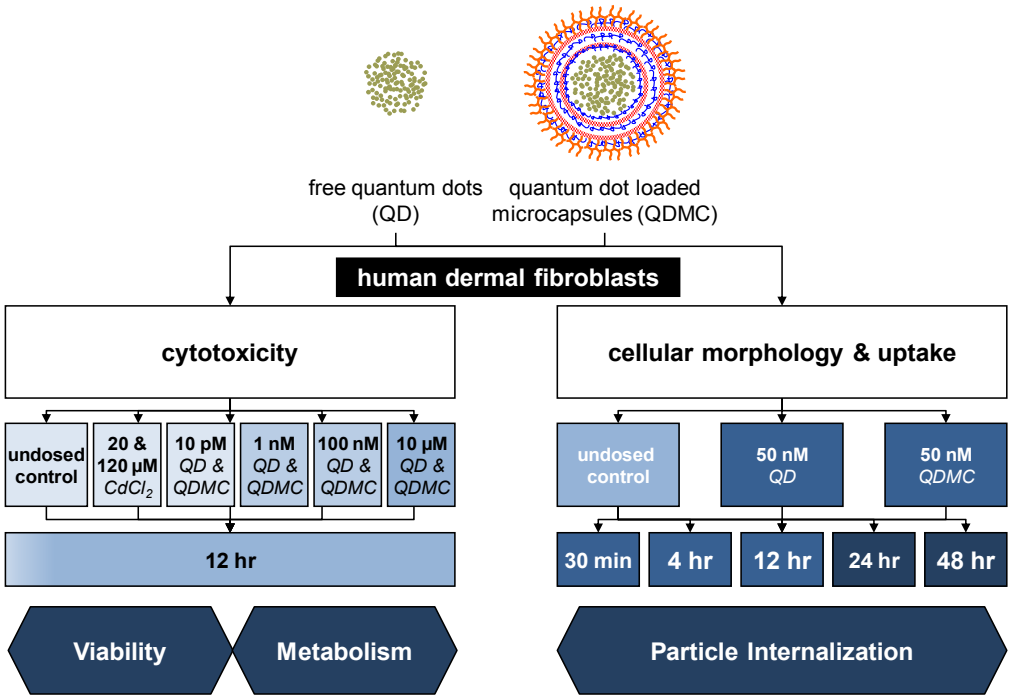

Fig. 5.2. Experimental design. Flowchart of the protocol used for testing the cellular response (cytotoxicity and morphology) of human dermal fibroblasts (HDF) to free quantum dots (QD) and quantum dot loaded microcapsules (QDMC). Cultured cells were exposed to either QD or QDMC for all experiments. $CdCl_2$ was used in some experiments as a positive control. Cytotoxicity, including % dead, metabolism, and apoptosis, were determined over a dose-response, while cellular morphology and uptake were determined over a time course.

5.2 Methods

5.2.1. QD synthesis

Core/shell (CdSe/ZnS) QDs were synthesized in a coordinating solvent tri-n-octylphosphine oxide (TOPO, 99%, Aldrich) in accordance with previously published procedures (Peng and Peng, 2001). The synthesis was performed in a single mode CEM Discover® microwave reactor operating at 300 W, 2.45 GHz. Cadmium oxide (CdO, 99.99%, Alfa Aesar, 0.0514 g, 0.4 mM) along with tetradecylphosphonic acid (TDPA,98%, Alfa Aesar, 0.2232 g, 0.8 mM) and TOPO (3.7768, 9 mM) were heated with continuous stirring in a 125 mL glass flask. The mixture was heated to approximately 300 ℃ under argon (Ar) flow for 15 min. A selenium stock solution (0.0411 g, 0.5 mM, Aldrich, 99 %) dissolved in 2.4 mL (2 g) of tri-n-octylphosphine (TOP, 99%, Aldrich) TOP) was injected at 270 ℃ and QDs were allowed to grow for 150 s. A ZnS shell was grown on the CdSe cores by injecting a mixture of Zn and S precursors: 1.6 mL (12 mM) dimethylzinc (DMZ-1M in heptane, Aldrich), 0.42 mL (2 mM) hexamethyldisilathiane (HMDS, Aldrich), and 6.3 mL (14 mM) TOP. The reaction mixture was heated for 30 min at 200 ℃. The quantum yield of the QDs increased on annealing the particles at a temperature of ~100 ℃ for a period of two hours.

The QDs were surface modified with high molecular weight branched PEI (b-PEI) (Aldrich, MW 25,000) using similarly reported procedures (Nann, 2005). Briefly, a 10 mg/mL solution of b-PEI in chloroform was mixed with an equal volume of 4-5 µM QDs. The mixture was tumbled overnight at room temperature. QDs were precipitated from the mixture by addition of excess cyclohexane (Sigma-Aldrich, >99%) and

suspended in deionized water. Excess PEI was extracted from the aqueous QD solution by addition of fresh chloroform, which phase-separated from water. The zeta potential of the PEI coated QDs was measured at approximately +29.7 ± 6.2 mV by a Zetasizer Nano ZS (Malvern Corp, Worcestershire, UK). The quantum yield of PEI coated QDs as produced is estimated to be 11.1 %.

5.2.2. QD microencapsulation

To microencapsulate the QDs in microcapsules (Figure 5.1), QDs were first entrapped in $CaCO_3$ microparticles using a modification of Petrov's protocol (Petrov et al., 2005). Briefly, 2.4 mL of a 2.17 μM PEI-coated QD solution was added to 7.6 mL of a Na_2CO_3 solution containing 40 mg of PSS (M_w = 70 kDa) for a final Na_2CO_3 concentration of 0.2 M. While stirring the Na_2CO_3 solution, 10 mL of a 0.2 M $CaCl_2$ solution was quickly added. After stirring for 30 s, the resulting particle suspension was centrifuged at 2500 *g* for 5 min to remove any remaining free QDs and unreacted salts; the precipitate was rinsed three times with deionized water and imaged using an inverted epifluorescence microscope (Nikon Eclipse TE2000-U) with a 40X objective (Nikon Plan Fluor, 0.75), 1.5X secondary magnification, and a color digital camera (Nikon DS-Fi1). Particle size measurements were performed using an Elzone II Particle Size Analyzer equipped with a 30 μm orifice tube (Micromeritics, Norcross, GA). Particle diameter was validated via optical microscopy. Zeta potential measurements, as an indicator of microcapsule surface charge, were performed using a Zetasizer Nano ZS (Malvern Corp, Worcestershire, UK). Encapsulation efficiency was estimated by

measuring the fluorescence intensity of the QDMC solution and dividing by the sum of the fluorescence intensities of the QDMC solution and the supernatant solution recovered from the CaCO3 microparticle precipitation, which contained unencapsulated QDs. Due to the high scattering of the samples, a PC1 photon counting spectrofluorometer (ISS, Champaign, IL) was modified using a bifurcated fiber optic bundle to collect fluorescence using 180° collection geometry. Empty $CaCO_3$ microcapsules (containing no QDs) were prepared using the aforementioned protocol, with the exception that 2.4 mL of deionized water was substituted for the PEI-coated QD solution.

Nanofilms were deposited on the $CaCO_3$ template using the LbL method, in which substrates are immersed in polyelectrolyte solutions of alternating charge (Caruso et al., 1998; Decher, 1997; Volodkin et al., 2004b). The first ten bilayers were comprised of polyelectrolytes PSS and PAH (M_w = 52 kDa). The surface charge of $CaCO_3$ microparticles at or below pH 8 is positive, so anionic PSS was the first polyelectrolyte deposited, followed by cationic PAH (Volodkin et al., 2004a). Deposition of each polyelectrolyte layer was achieved by suspending the particles in 1 mL of a 2 mg/mL polyelectrolyte solution containing 0.2 M NaCl. Lastly, the particles were coated with a terminal bilayer comprised of PSS and poly-L-lysine(100)-g[4.5]-polyethylene glycol(114) (PLL-g-PEG, Alamanda Polymers, M_w = 129 kDa), yielding $CaCO_3$ microparticles coated with a $(PSS/PAH)_{10}$/(PSS/PLL-g-PEG) nanofilm. Dissolution of the $CaCO_3$ template was accomplished via a mild treatment with 0.1 M ethylenediaminetetraacetic acid (EDTA) adjusted to pH 7.6; complete core dissolution

was visually confirmed using phase microscopy. Note: $(PSS/PAH)_5$/(PSS/PLL-g-PEG) nanofilm QDMCs were also made and compared to $(PSS/PAH)_{10}$/(PSS/PLL-g-PEG) QDMCs in figures 5.6-5.8.

5.2.3. Microscopy

HDF cells (ATCC, Manassas, VA) were cultured in Dulbecco's Modified Eagle's Medium (DMEM, Gibco, Austria), which was supplemented with 10% FBS and an antibiotic cocktail consisting of penicillin, streptomycin, and amphotericin (Sigma-Aldrich, St. Louis, MO). Incubation took place at 37°C with humidity and 5% CO_2. Live cells were cultured in this manner and treated with 50 pM QD and QDMC for 30 min, 4 hrs, 12 hrs, 24 hrs, and 48 hrs to determine the manner and extent of QD uptake into the fibroblasts. An undosed control was also included for comparison. Then, 0.25 µL stock solution Syto 63 (Invitrogen, Carlsbad, CA) was directly added to 1 mL of media in the borosilicate, dual-well chamber slides (Lab-Tek, Nagle Nunc Intl., Rochester, NY) for a 30 min incubation at 37°C. A Zeiss 510 Meta confocal microscope was utilized at 40X (1.3 NA, oil immersion) to image the treated and stained live cells. A 488 nm Ar ion and a 633 nm He-Ne laser were employed to excite the QDs and stain, respectively. Zeiss LSM 510 Software was used to acquire the images.

5.2.4. Metabolism

Cell populations (n=4) were then seeded in 24 well plates, allowed to grow to 80% confluency, and dosed with 0.05-50 nM concentration range for both the QD and

QDMC or left undosed as a negative control. A 20 and 120 μM $CdCl_2$ solution was utilized as a positive indicator for absence of fluorescent probe metabolism. The dosed media was aspirated after 12, 24, or 48 hr. The cells were washed with PBS and phenol red-free DMEM media was added. Resazurin dye (10% v/v, Sigma Aldrich, St. Louis, MO) was added and the cells were incubated for an additional 3 hr. Fluorescence intensity was obtained by exciting at 560 nm and recording emission at 590 nm. Fluorescence compatibility was measured prior to assay (Appendix Figure A-3). QD and QDMC toxicity to cells was measured in terms of percent healthy cells via microscopy.

5.2.5. Metallothionein expression

HDF were cultured in the same conditions as above. Cells in 6-well plates were treated with 30 nM QDs, 30 nM QDMCs, 30 μM cadmium chloride salt, 30 μM hydrogen peroxide, or left untreated. After 24 hrs exposure, cells were washed in ice cold 1X PBS, then protease inhibitor cocktail (Sigma-Aldrich) and high salt lysis buffer were added to wells. Protein was isolated by collecting supernatant via centrifugation. Samples were loaded into 10% SDS-PAGE gels and run at 120 mV. Gels were transferred to PVDF membranes, which were blocked in 5% milk and incubated in an anti-metallothionein primary antibody solution overnight at a concentration of 1:1000 (Santa Cruz Biotechnology, Santa Cruz, CA). Secondary antibody (Goat, anti-mouse, Santa Cruz) was prepared in fresh 5% milk solution at 1:5000 dilution and incubated at room temperature for two hours. Immobilon™ Western Chemiluminescent HRP

substrate (Millipore, Billerica, MA) was added to rinsed membranes and film exposures were taken. β-actin, 1:10,000 (Sigma, St. Louis, MO) was used as a loading control. Blots shown are representative of several independent experiments.

5.2.6. Sample supernatant metal analysis

To ensure microcapsule integrity after storage in 4°C conditions, cadmium, selenium, and zinc content within the supernatant from QDMC samples stored for a one month duration was analyzed using inductively coupled plasma-mass spectroscopy (ICP-MS). Supernatant was collected from vials of both empty and QD-loaded microcapsules stored in water for one month and compared with two types of digested QD samples at approximately the same concentration as would be present if all microcapsules their entire contents into the supernatant. All suspensions were digested under heat (60°C) and acid (5% HCl and 1% nitric acid, by volume), and analyzed for metal content via inductively coupled plasma mass spectroscopy (ICP-MS) using an Elan DRC II, Perkin Elmer SCIEX (Waltham, MA).

5.3 Results

5.3.1. Microencapsulation and QD-loading efficiency

The average microparticle diameter was determined to be 5.24 μm as measured with a particle size analyzer, with a standard deviation of 1.25 μm (95% confidence interval: 5.165 - 5.317 μm) (Table 5.1 and Figure 5.1B). This diameter was also

Table 5.1. QD and QDMC characterization table. *As measured on $CaCO_3$ microparticles coated with $(PSS/PAH)_{10}$/(PSS/PLL-g-PEG) nanofilms.

Property	QD	QDMC
Size in water	14-16 nm	3-5 μm
Surface charge	+29.7 ± 6.2 mV	near neutral*
Interior volume	-	14.14-65.45 μm^3
Calculated surface area	~706 nm^2	28.27-78.54 μm^2
No. of QDs/microcapsule	-	2.05e10
No. of Cd^{+2} ions/system	265.8	5.46e12
Excitation/Emission	380/545 nm	380/545 nm

observed via optical microscopy. The encapsulation efficiency was determined to be ~30.57%, resulting in about 9,000,000 QDs/microcapsule. At this encapsulated concentration, the volume occupied by the microencapsulated QDs is ~0.1% of the total microcapsule interior volume. Based on the diameter of the microcapsule, the average surface area would be 7.854×10^{-11} m^2 (i.e., 78.54 μm^2).

Figure 5.1 depicts the process used to form the QDMC. Morphology of the microcapsules was determined with microscopy. Following core dissolution, brightfield and fluorescence images of the resulting microcapsules were acquired (Figure 5.1 C-D). The brightfield image reveals a spherical morphology, and the fluorescence image confirms successful QD microencapsulation. Both the micrographs and the histogram show that the QDMC sample contains monodisperse microcapsules. In addition, QDs do not show evidence of self-quenching (i.e., red-shift of emission peak) once microencapsulated, as shown by the fluorescence emission spectra in Appendix Figure A-4.

5.3.2. Differential metabolism effects

Cellular viability was measured in two independent studies. First, viable cells were counted using brightfield microscopy (data not shown). Second, changes in metabolic activity were measured using the conversion of resazurin to resorufin (Figure 5.3). In both studies, HDF cells were exposed to QDs, QDMCs, and $CdCl_2$ (positive control). For comparison, the total number of QDs at each concentration was kept constant between the QD and QDMC samples; e.g., 5 nM QDMC refers to enough MCs

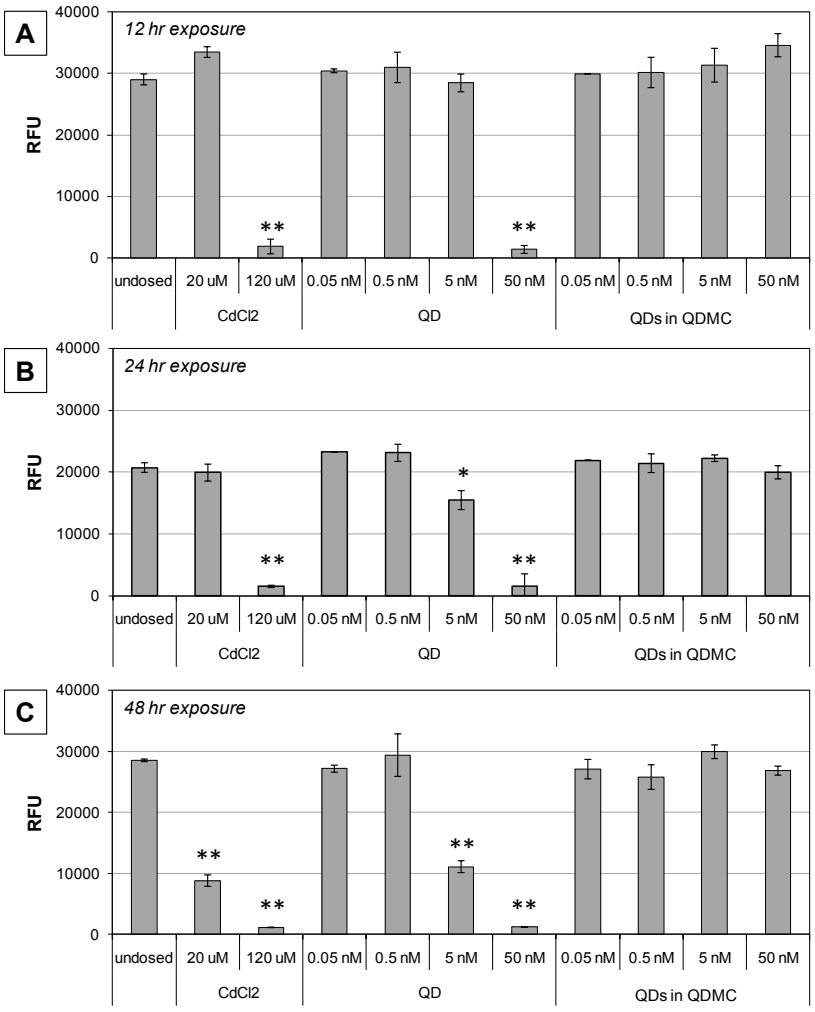

Fig. 5.3. Differential cytotoxicity. Cytotoxicity was measured at A) 12 hrs, B) 24 hrs, and C) 48 hrs via fluorescence intensity of reduced resazurin. HDF cells at all time points were either exposed to 0.05-50 nM QDs or microencapsulated QDMCs, 20 or 120 μM cadmium chloride positive control, or unexposed. * p-val < 0.05, ** p-val < 0.001. Note: the QDMC concentrations refer to the total concentration of QDs contained in the microcapsules.

to provide a total QD concentration of 5 nM. All responses were compared to those of undosed cells. Results indicated a strong dose- and time-dependent response relationship present in QD and $CdCl_2$-treated cells, but no significant changes in metabolic activity were found by 48 hr in QDMC-treated cells. Cells exposed to empty microcapsules were also examined for changes in viability and metabolic activity and no significant changes were found.

It is important to note that QDs are similarly toxic at much lower concentrations than the cadmium chloride positive control. This is not surprising since there are factors other than chemical composition (e.g. surface charge, particle size, ROS generation potential) that must be considered when evaluating nanoparticle cytotoxicity. For example, it has been shown that cadmium-containing QDs are more toxic to bacteria than an equivalent cadmium concentration of cadmium salt due to higher ROS generation, damaged cell membranes, and the presence of Se^0 and dissolved cadmium (Priester et al., 2009).

5.3.3. Cellular uptake and morphological changes

Metabolism study results corroborate the cellular uptake data (Figure 5.4), where the number of QD aggregates increases at approximately the same rate as toxicity progresses. Figure 5.5 illustrates that the free QDs visibly disrupted the cellular morphology, which became apparent after the 12 hr time point and progressed throughout the remainder of the experiment. Cells dosed with an equivalent Cd atom concentration of the QD-loaded microcapsules displayed no evidence of particle uptake

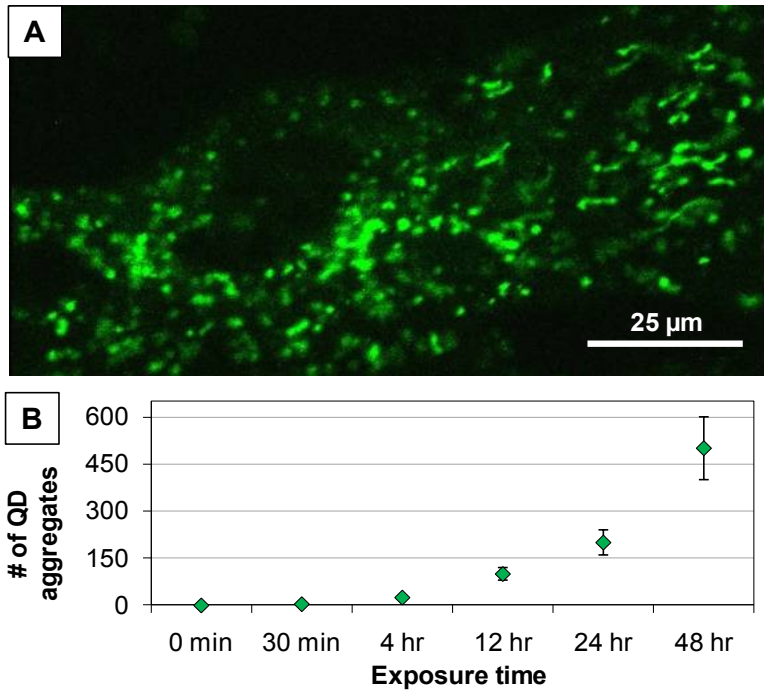

Fig. 5.4. QD association and cellular morphology. (A) QD accumulation in HDF mitochondria (Confocal, 60X, Zeiss). (B) The number of QD aggregates accumulating in HDF increases over time.

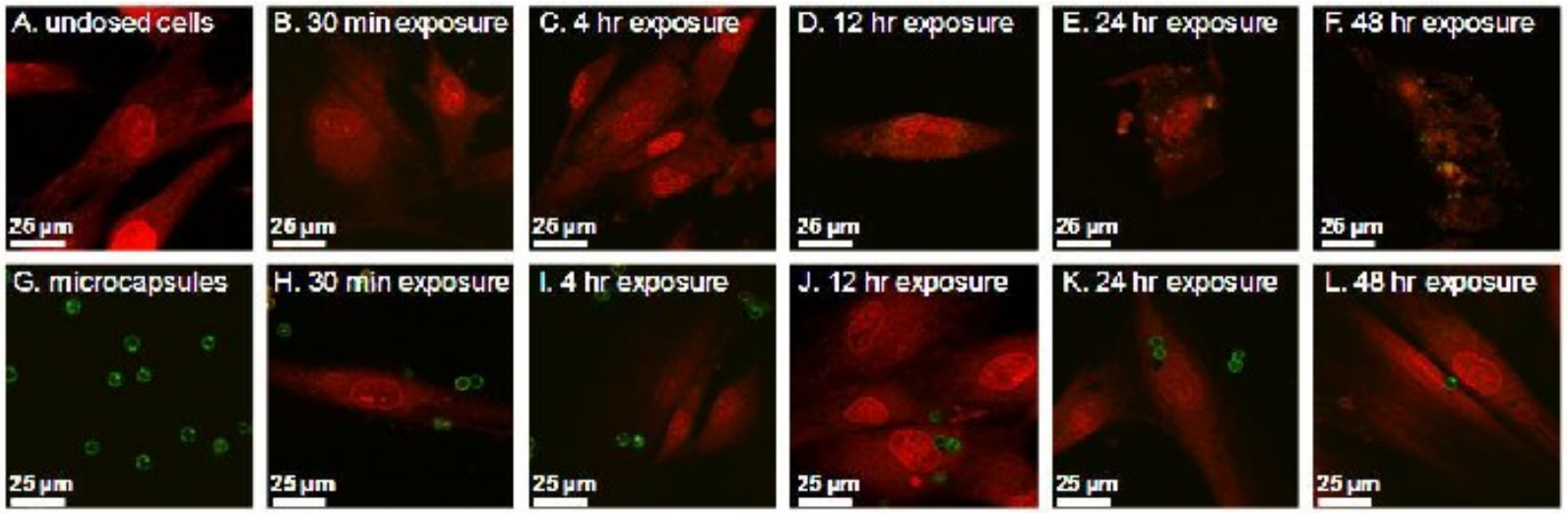

Figure 5.5. Comparative cell morphology over time in response to QDs and QDMCs. Fluorescence microscopy of micrographs B through F show the cellular morphology of HDFs exposed to QDs over a 30 minute to 48 hour time course study. As exposure time increases, the cells exhibit compromised cytoplasmic membranes. Micrographs H through L show the cellular morphology of HDFs exposed to QDMC over a 30 minute to 48 hour time course study. Cells remain intact and healthy over the course of the 2-day study. Z-stack images indicate that microcapsules do not enter cells. Microcapsules are resting on top of cells, but do not enter cells. QDMC-treated cells were dosed at an equivalent amount of Cd^{+2} ions relative to the amount present in QD treatments. Cells dosed with an equivalent Cd concentration of the QD-loaded microcapsules displayed no evidence of particle uptake and remained viable with no sign of deterioration through the 48 hr time point.

and remained viable with no sign of deterioration through the 48 hr time point.

5.3.4. Capsule integrity

Results from western blot analysis reveal differences in HDF metallothionein expression in response to presence or absence of microencapsulation and the number of bilayers applied to the template (Figure 5.6). Here, 5-bilayer capsules did not afford cells protection from metals leakage, as evidenced by a marked increase in protein expression, which was comparable to the cadmium chloride positive control. The 10-bilayer-treated cells, however, expressed very little metallothionein, which was slightly more than the untreated cells.

ICP-MS analysis of 10-bilayer capsules confirmed the effectiveness of the 10-bilayer approach, as only negligible amounts of cadmium, zinc, and selenide were found in capsule supernatant after a one-month storage in 4°C conditions (Table 5.2).

5.4 Discussion

Due to the recent surge of nanoparticle development for imaging and therapeutic applications, there is reason to evaluate toxicity of nanomaterials. Some studies suggest nanoparticles do affect biological systems at the cellular, subcellular, and protein levels (Ale-Agha et al., 2010; Choi et al., 2010; Lunov et al., 2010). Other works indicate that nanoparticles are cleared from circulation by macrophages depending on particle composition, size, charge, surrounding pH, dose, or route of exposure

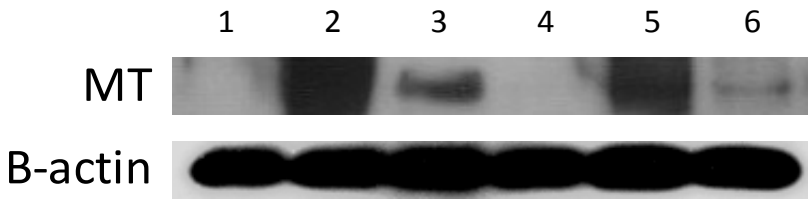

Figure 5.6. Metallothionein expression. HDF were treated for 24 hrs as follows: Lane 1, untreated; 2, 30 μM cadmium chloride salt; 3, 30 nM PEI-QD (positively charged); 4, 30 μM hydrogen peroxide; 5, 30 nM 5 bilayer microencapsulated QDs (positively charged); 6, 30 nM 10 bilayer microencapsulated QDs (neutrally charged). Western blotting for metallothionein, a protein upregulated in the presence of intracellular heavy metals, revealed differences between samples. β-actin was used as a loading control. Experiment was performed in duplicate with similar results.

Table 5.2. Microcapsule leakage analysis. Inductively coupled plasma-mass spectroscopy was utilized as a method to assess possible trace amounts of microcapsule leakage of cadmium, selenide, and zinc from quantum dot contents. Supernatant was collected from vials of both empty and QD-loaded microcapsules stored in water for one month and compared with two types of digested QD samples at approximately the same concentration as would be present if all microcapsules their entire contents into the supernatant. Levels of the three metals in QD-loaded capsules were nearly identical to empty microcapsules.

	(mg/L)			(mM)		
Sample ID	**Cd**	**Se**	**Zn**	**Cd**	**Se**	**Zn**
DI water	<0.00006	<0.00030	<0.0012	<0.000001	<0.000004	<0.00002
microcaps w/o QDs supernatant	<0.00006	<0.00030	0.0603	<0.000001	<0.000004	0.001
microcaps with QDs supernatant	<0.00006	0.00136	0.0141	<0.000001	0.00002	0.000
PEI-QD digested	21.7	10.3	53.4	0.193	0.130	0.817
DHLA-QD digested	79.2	35.5	62.4	0.705	0.450	0.954

(Dobrovolskaia et al., 2008; Moghimi and Gray, 1997; Moghimi and Szebeni, 2003; Semmler-Behnke et al., 2007). Nevertheless, there are concerns that Cd-containing QDs are toxic to both cell cultures and live animals because they contain a toxic heavy metal. Are there engineering solutions that can mitigate the nanoparticle toxicity while maintaining functionality? In this body of research, it can be concluded that 10-bilayer QD-loaded microcapsules are minimally cytotoxic, if at all, as Figures 5.3, 5.5, and 5.6 suggest. ICP-MS analysis confirmed a lack of heavy metal leakage from the capsules over time (refer to Table 5.2).

Preliminary studies with 5-bilayer capsules revealed the importance of a sufficient number of layers within the nanoshell. Figure 5.7 illustrates morphological differences via fluorescence microscopy after treatment with either QD-treated cells (top row), 5-bilayer QDMCs (middle row), or 10-bilayer QDMCs (bottom row). 5-bilayer microcapsules entered the cells and a few ruptured by the latest time point at 48 hrs. Upon examination of cellular morphology, 5-bilayer microcapsules caused altered cellular structure by 48 hrs, similar to QD-treated cells, whereas 10-bilayer microcapsules remained on the surface of cells and did not provoke any noticeable morphological changes. This suggests that the nanoshell partially degraded, changing the surface characteristics of the QDMCs and allowing entry across cytoplasmic membranes. Figure 5.8 depicts a proposed mechanism of the differences in interaction between single QDs and QDMCs with or without surface charge, where a neutral charge on a QDMC minimizes cellular contact and prevents uptake.

Previous studies have shown that the endocytosis of nanoparticles in acidic endosomes degrade nanomaterials and cause leaching of metals, thus producing stress, triggering apoptotic response, and eventual death (Xiao et al., 2010). We propose that the observed death could be mitigated by controlling uptake via microencapsulation and altering microcapsule outer surface charge. These mitigations can improve the biocompatibility of QDs by decreasing internalization. Data from the literature has indicated that particles that remain in the extracellular matrix are typically less toxic to cells than particles that have breached the cytoplasmic membrane (Brunner et al., 2006; Nel et al., 2006; Oberdorster et al., 2007) Research presented in this paper suggests that QDMC biocompatibility is due to lack of cellular uptake and is evidenced by normal mitochondrial function. Therefore, as new nanomaterials (including microencapsulated systems or composited materials) that possess useful physical and chemical properties are developed, understanding the propensity for cellular uptake and subsequent adverse cellular effects is vital.

Cellular uptake is an additional parameter to be considered in the design and evaluation of biocompatible nanoparticles for biological applications. This data provides strong evidence that specific microencapsulation of CdSe/ZnS particles imparts substantial protection. The most common capping strategies are known to decrease toxicity, but they also often decrease functionality by increasing the size of the QDs. We have shown here that by microencapsulation of the nanoparticle, toxicity is decreased, while luminescence – a precursor for functionality – remains uncompromised.

Salient points to be learned from this research:

- *Quantum dot microencapsulation results in decreased cellular uptake and toxicity in human dermal cells.*
- *Microencapsulation of quantum dots does not alter their fluorescent properties.*

Questions remaining unanswered:

- *Although microencapsulated quantum dots remain intact in water for extended periods of time, do they also remain intact in vivo over time?*
- *Is there any immunological response triggered in the dermal tissue resulting from exposure to quantum dot-loaded microcapsules?*

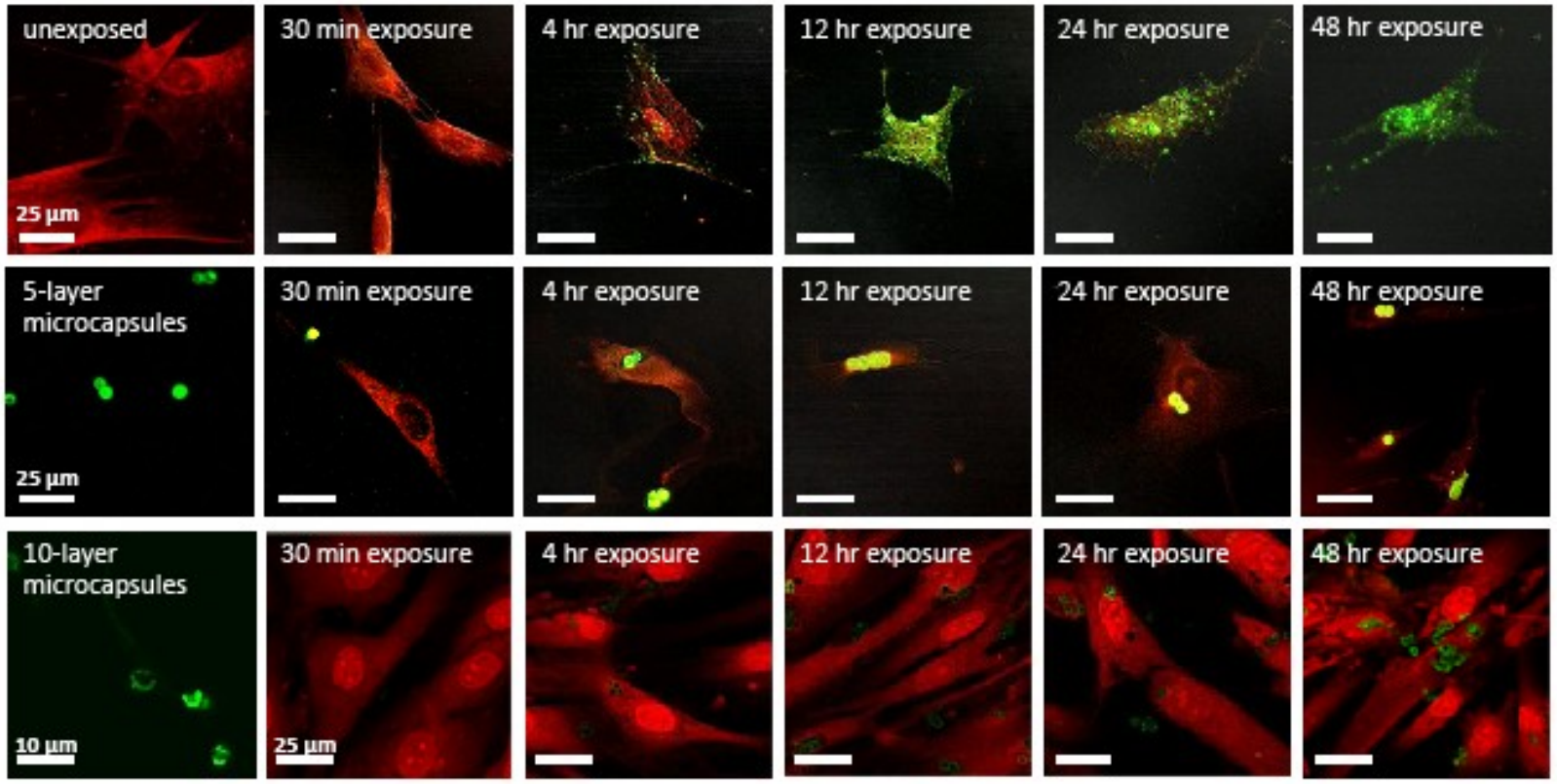

Figure 5.7. Confocal microscopy reveals differences in cellular uptake, based on surface charge. Top row: HDF cells exposed over time to unencapsulated PEI QDs (positive chg); Middle row: HDF cells exposed over time to 5-layer microencapsulated QDs (positive chg); Bottom row: HDF cells exposed over time to 10-layer microencapsulated QDs (neutral chg).

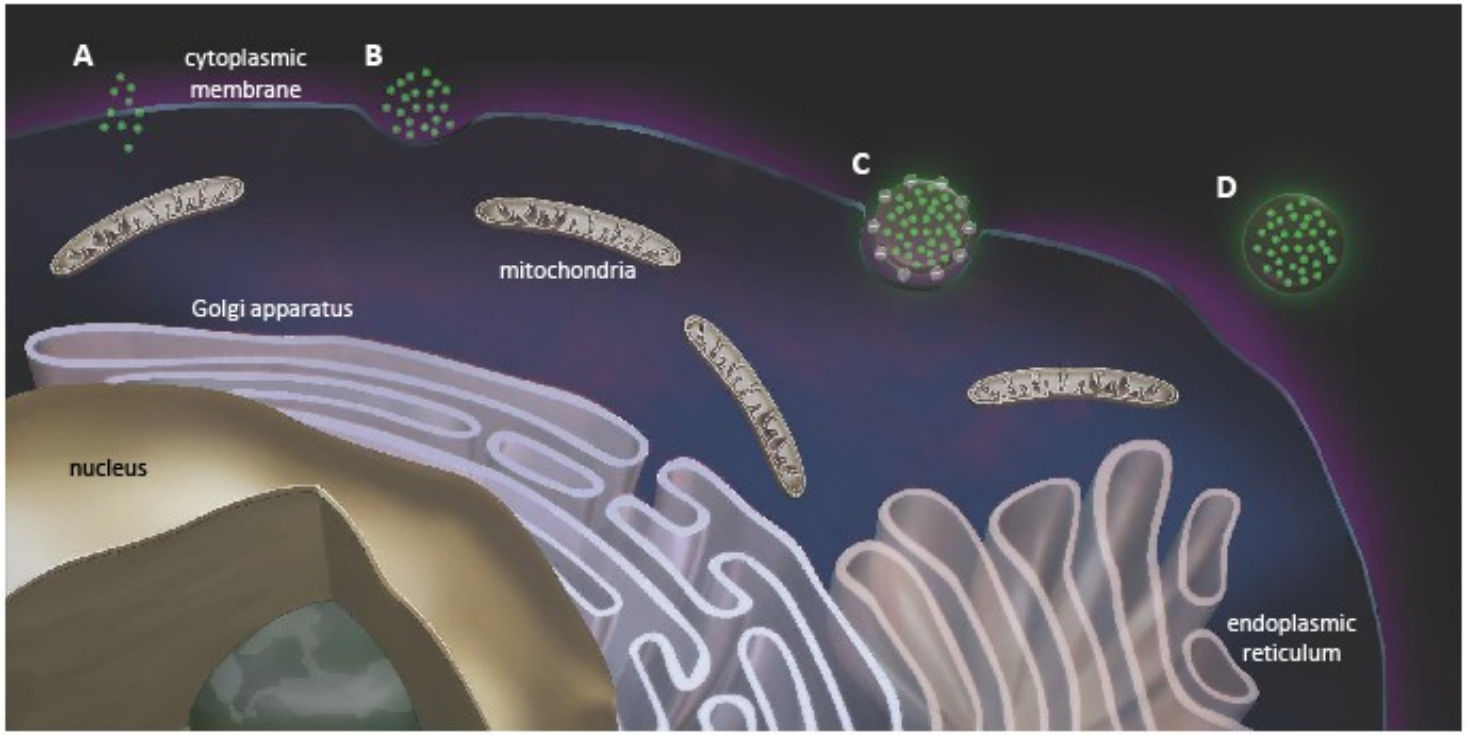

Figure 5.8. Proposed cellular-QD or cellular-QDMC interactions. A) Passive diffusion/Receptor-mediated (single QDs); B) Phagocytosis/Macropinocytosis (aggregated QDs); C) Phagocytosis/Macropinocytosis (charged microcapsules); D) Lack of uptake (neutral microcapsules).

CHAPTER VI

CONCLUSIONS

Due to the rapid growth of the nanotechnology sector, and thus an exponential increase in the number of consumer products utilizing nanomaterials, there is a need to determine whether the potential for negative human health effects exists. A precautionary approach in the incorporation of nanoparticles into consumer products is necessary because it remains possible that the same physicochemical properties which make nanomaterials beneficial, *may* also yield negative toxicological consequences.

At the nanoscale, much larger particle surface-to-volume ratios play a significant role in interactions at the biological interface upon exposure. Due to the 'non-bulk' properties of nanoparticles, including increased surface reactivity, processes such as dissolution or the generation of reactive oxygen species may be enhanced. The likelihood of this “enhancing effect” does heavily rely upon the physicochemical properties of each nanoparticle type, however. Additionally, particles at the nanoscale can gain access to cellular structures otherwise that would otherwise be restricted from entry of larger particles.

Quantum dots were utilized in much of this work as a “model” nanoparticle to study not only membrane penetrability, but also resulting toxicity. Their fluorescent properties and consistent size allowed for more sophisticated and precise data acquisition, as well as the ability to modify one physicochemical parameter at a time, such as surface charge. In general, dermal cells exposed to QD nanocrystals induced a

widespread modulation of genes and proteins, overall, when compared to unexposed control cell populations. Modulated factors included indicators of oxidative stress, apoptosis, inflammation, and more general immune responses. The effects of QDs on cells in culture are dependent on a variety of factors including, but not limited to, exposure time and dosing concentrations. Cellular effects from 15 nm CdSe/ZnS-COOH QD exposure were found to primarily follow the NF-κB pathway. In addition, QDs induced a differential cytotoxicity in keratinocytes and fibroblasts at different exposure concentrations and time points, even at physiologically relevant doses, thus emphasizing the need to investigate potential mechanisms of action among different cell types within the same target organ.

There are many efforts in understanding the effects of different nanoparticles on cell viability and metabolism, however, not much is known regarding the distinct molecular mechanisms of inflammation and cellular stress using low exposure concentrations. To address this gap in the literature, a novel experimental design was utilized that specifically probed the effects of a panel of commonly studied engineered nanomaterials along immunomodulatory pathways, including NF-κB. The panel of particles selected for this study included QD nanocrystals, titanium dioxide, hydroxylated fullerenes, and silver nanoparticles. Cell viability, antioxidant activity, select messenger RNA, and protein modulation were studied in primary human dermal fibroblasts (HDF) and NF-κB knockdown HDF cells. Differences in cellular response to nanoparticles in protein and antioxidant experiments were evident in NF-κB knockdown cells, emphasizing the importance and extent of NF-κB after nanoparticle exposures. All

nanoparticles used in the study caused concentration and time-dependent cell death, as well as NF-κB-dependent cell death where tested. Differential responses in NF-κB and ERK levels may be partially attributed to particle-specific physicochemical characteristics. For example, the more toxic response to silver particles may be associated with its relatively dense nature and/or instability in the aqueous phase that ultimately translates into higher exposure concentrations when compared to the other materials used in this study. Nanoparticles also caused modulation of genes known to be associated with inflammatory, immune, oxidative stress, and apoptotic responses. These methods, along with the resultant data sets, serve as a potential model for studying the complex pathway-specific biochemical responses in cell and tissue systems associated with nanoparticle exposures.

It is well documented that various nanoparticles are known to induce reactive oxygen species generation. This imbalance in the redox state of the cell has also been shown to induce a DNA damage cascade in cells and tissues. Nanoparticles are common in dermal preparations, such as sunscreens, cosmetics, and pharmaceuticals, thus there is a critical need to evaluate their DNA damage production capability in dermal models. Primary human dermal fibroblasts (HDF) exposed to <100 nm cerium oxide (CeO_2), titanium dioxide (TiO_2), and zinc oxide (ZnO) were examined in an attempt to determine the effects of three different, yet similarly sized metal oxide particles through the analysis of reactive oxygen species (ROS) generation, relevant protein upregulation response, and subsequent single and double strand break DNA damage. Cell death was most elevated with ZnO, followed by TiO_2 and CeO_2. ROS generation was measured

and indicated that CeO_2 and ZnO caused increases in relative fluorescence at the earlier time points, as compared to untreated cells. ZnO caused upregulation of HMOX-1 and phosphorylation of p38, whereas CeO_2 caused upregulation of SOD1. Comet assay and gamma-H2AX immunocytochemistry results indicated that ZnO triggered significant DNA strand break damage in HDF at 20 ppm concentrations. Cell cycle arrest was confirmed in ZnO-treated samples by flow cytometry and western blot techniques. These data suggest that, of the three particle types tested, ZnO may be most toxic in an *in vivo* dermal exposure scenario. Further studies comparing the ability of these nanoparticles to penetrate both intact and damaged skin surfaces would prove beneficial and possibly aid in the development of improved nanomaterials.

Lastly, QDs were microencapsulated in an effort to prevent cellular uptake and resulting toxicity of QDs in a dermal scenario with a particular nanomaterial application as the goal. When CdSe/ZnS-polyethyleneimine (PEI) quantum dots (QDs) are microencapsulated in polymeric microcapsules, human fibroblasts are protected from acute cytotoxic effects. Differences in cellular morphology, uptake, and viability were assessed after treatment with either microencapsulated or unencapsulated dots. Specifically, QDs contained in microcapsules terminated with polyethylene glycol (PEG) mitigate contact with and uptake by cells, thus providing a tool to retain particle luminescence for applications such as extracellular sensing and imaging. The microcapsule serves as the "first line of defense" for containing the QDs. This enables the individual QD coating to be designed primarily to enhance the function of the biosensor.

REFERENCES

Académie des Sciences and Académie des Technologies, 2004. Science and technology report no. 18: nanosciences and nanotechnologies http://www.tinyurl.com/nqwdda.

Adams, K. E., Medhurst, A. L., Dart, D. A. and Lakin, N. D., 2006. Recruitment of ATR to sites of ionising radiation-induced DNA damage requires ATM and components of the MRN protein complex. Oncogene 25, 3894-3904.

Ahamed, M., Akhtar, M. J., Siddiqui, M. A., Ahmad, J., Musarrat, J., AlSalhi, M. S. and Alrokayan, S. A., 2011. Oxidative stress mediated apoptosis induced by nickel ferrite nanoparticles in cultured A549 cells. Toxicology 283, 101-108.

Alam, J., Stewart, D., Touchard, C., Boinapally, S., Choi, A. M. and Cook, J. L., 1999. Nrf2, a cap'n'collar transcription factor, regulates induction of the heme oxygenase-1 gene. J. Biol. Chem. 274, 26071-26078.

Ale-Agha, N., Albrecht, C. and Klotz, L. O., 2010. Loss of gap junctional intercellular communication in rat lung epithelial cells exposed to carbon or silica-based nanoparticles. Biol. Chem. 391, 1333-1339.

Alivisatos, A. P., Gu, W. and Larabell, C., 2005. Quantum dots as cellular probes. Ann. Rev. Biomed. Eng. 7, 55-76.

Almeida, N. F., Beckman, E. J. and Ataai, M. M., 1993. Immobilization of glucose oxidase in thin polypyrrole films: influence of polymerization conditions and

film thickness on the activity and stability of the immobilized enzyme. Biotechnol. Bioeng. 42, 1037-1045.

Alvarez-Roma, R., Naika, Y. N., Kaliaa, A., Guy, R. H. and Fessi, H., 2004. Skin penetration and distribution of polymeric nanoparticles. J. Control. Release 99, 53-62.

Ambrosino, C. and Nebreda, A. R., 2001. Cell cycle regulation by p38 MAP kinases. Biol. Cell. 93, 47-51.

Antwerp, D. J. V., Martin, S. J., Kafri, T., Green, D. R. and Verma, I. M., 1996. Suppression of TNF-alpha-induced apoptosis by NF-kappaB. Science 274, 787-789.

AshaRani, P. V., Low Kah Mun, G., Hande, M. P. and Valiyaveettil, S., 2009. Cytotoxicity and genotoxicity of silver nanoparticles in human cells. ACS Nano 3, 279-290.

Atherton-Fessler, S., Feng, L., Gabrielli, B., Lee, M. S., Peng, C. and Piwnica-Worms, H., 1994. Cell cycle regulation of the p34cdc2 inhibitory kinases. Mol. Biol. Cell 5, 989-1001.

Auffan, M., Rose, J., Bottero, J., Lowry, G., Jolivet, J. and Wiesner, M., 2009a. Towards a definition of inorganic nanoparticles from an environmental, health and safety perspective. Nat. Nanotech. 4, 634-641.

Auffan, M., Rose, J., Orsiere, T., Meo, M. D., Thill, A., Zeyons, O., Proux, O., Masion, A., Chaurand, P., Spalla, O., Botta, A., Wiesner, M. R. and Bottero, J., 2009b.

CeO2 nanoparticles induce DNA damage towards human dermal fibroblasts in vitro. Nanotoxicology 3, 161-171.

Azzazy, H. M. E., Mansour, M. M. H. and Kazmierczak, S. C., 2007. From diagnostics to therapy: prospects of quantum dots. Clin. Biochem. 40, 917-927.

Bakkenist, C. J. and Kastan, M. B., 2003. DNA damage activates ATM through intermolecular autophosphorylation and dimer dissociation. Nature 421, 499-506.

Baroli, B., Ennas, M. G., Loffredo, F., Isola, M., Pinna, R. and López-Quintela, M. A., 2007. Penetration of metallic nanoparticles in humanfull-thickness skin. J. Invest. Dermatol. 127, 1701-1712.

Beg, A. A. and Baltimore, D., 1996. An essetial role for NF-kappaB in preventing TNF-alpha-induced cell death. Science 274, 782-784.

Benn, T., Westerhoff, P. and Herckes, P., 2011. Detection of fullerenes (C60 and C70) in commercial cosmetics. Environ. Pollut. 159, 1334-1342.

Bennat, C. and Muller-Goymann, C. C., 2000. Skin penetration and stabilization of formulations containing microfine titanium dioxide as physical UV filter. Int. J. Cosmet. Sci. 22, 271-283.

Berg, J. M., Romoser, A. R., Banerjee, N., Zebda, R. and Sayes, C., 2009. The relationship between pH and zeta potential of ~30 nm metal oxide nanoparticle suspensions relevant to *in vitro* toxicological evaluations. Nanotoxicology 3, 276-283.

Bhabra, G., Sood, A., Fisher, B., Cartwright, L., Saunders, M., Evans, W. H., Surprenant, A., Lopez-Castejon, G., Mann, S., Davis, S. A., Hails, L. A., Ingham,

E., Verkade, P., Lane, J., Heesom, K., Newson, R. and Case, C. P., 2009. Nanoparticles can cause DNA damage across a cellular barrier. Nat. Nanotech. 4, 876-883.

Bianco, A., Kostarelos, K. and Prato, M., 2005. Applications of carbon nanotubes in drug delivery. Curr. Opin. Chem. Biol. 9, 674-679.

Binková, B., Giguère, Y., Rössner Jr., P., Dostál, M. and Srám, R. J., 2000. The effect of dibenzo[a,1]pyrene and benzo[a]pyrene on human diploid lung fibroblasts: the induction of DNA adducts, expression of p53 and p21(WAF1) proteins and cell cycle distribution. Mut. Res. 471, 57-70.

Black, K. A., McFarland, R. D., Grisham, J. W. and Smith, G. J., 1989. S-phase block and cell death in human lymphoblasts exposed to benzo[a]pyrene diol epoxide or Nacetoxy-2-acetylaminofluorene. Toxicol. Appl. Pharmacol. 97, 463-472.

Broide, D. H., Lawrence, T., Doherty, T., Cho, J. Y., Miller, M., McElwain, K., McElwain, S. and Karin., M., 2005. Allergen-induced peribronchial fibrosis and mucus production mediated by IkappaB kinase beta-dependent genes in airway epithelium. PNAS 102, 17723-17728.

Brown, D., Stone, V. and Findlay, P., 1999. Increased inflammation and intracellular calcium caused by ultrafine carbon black is independent of transition metals or other soluable components. Occup. Environ. Med. 58, 85-91.

Brunner, T. J., Wick, P., Manser, P., Spohn, P., Grass, R. N., Limbach, L. K., Bruinink, A. and Stark, W. J., 2006. In vitro cytotoxicity of oxide nanoparticles:

comparison to asbestos, silica, and the effect of particle solubility. Environ. Sci. Technol. 40, 4374-4381.

Bulavin, D. V., Higashimoto, Y., Popoff, I. J., Gaarde, W. A., Basrur, V., Potapova, O., Appella, E. and Fornace Jr., A. J., 2001. Initiation of a G2/M checkpoint after ultraviolet radiation requires p38 kinase. Nature 411, 102-107.

Bulavin, D. V., Saito, S. A., Hollander, M. C., Sakaguchi, K., Anderson, C. W., Appella, E. and Fornace, A. J., 1999. Phosphorylation of human p53 by p38 kinase coordinates N-terminal phosphorylation and apoptosis in response to UV radiation. EMBO J. 18, 6845-6854.

Busch, W., Kühnel, D., Schirmer, K. and Scholz, S., 2010. Tungsten carbide cobalt nanoparticles exert hypoxia-like effects on the gene expression level in human keratinocytes. BMC Genomics 11, 65.

Caruso, F., Caruso, R. A. and Mohwald, H., 1998. Nanoengineering of inorganic and hybrid hollow spheres by colloidal templating. Science 282, 1111-1114.

Cerretti, D. P., Kozlosky, C. J., Mosley, B., Nelson, N., Ness, K. V., Greenstreet, T. A., March, C. J., Kronheim, S. R., Druck, T., Cannizzaro, L. A., Huebner, K. and Black, R. A., 1992. Molecular cloning of the interleukin-1 converting enzyme. Science 256, 97-99.

Chan, K. and Kan, Y. W., 1999. Nrf2 is essential for protection against acute pulmonary injury in mice. PNAS, 12731-12736.

Chang, E., Thekkek, N., Yu, W. W., Colvin, V. L. and Drezek, R., 2006. Evaluation of quantum dot cytotoxicity based on intracellular uptake. Small 2, 1412-1417.

Chen, P., Migita, S., Kanehira, K., Sonezaki, S. and Taniguchi, A., 2011. Development of sensor cells using NF-κB pathway activation for detection of nanoparticle-induced inflammation. Sensors 11, 7219-7230.

Chen, X. and Schluesener, H. J., 2008. Nanosilver: a nanoproduct in medical application. Tox. Lett. 176, 1-12.

Cho, H. Y., Reddy, S. P. and Kleeberger, S. R., 2006. Nrf2 defends the lung from oxidative stress. Antioxid. Redox. Signal. 8, 76-87.

Choi, J., Zheng, Q., Katz, H. E. and Guilarte, T. R., 2010. Silica-based nanoparticle uptake and cellular response by primary microglia. Environ. Health Perspect. 118, 589-595.

Connor, E. E., Mwamuka, J., Gole, A., Murphy, C. J. and Wyatt, M. D., 2005. Gold nanoparticles are taken up by human cells but do not cause acute cytotoxicity. Small 1, 325-327.

Cortez, D., Wang, Y., Qin, J. and Elledge, S. J., 1999. Requirement of ATM-dependent phosphorylation of BRCA1 in the DNA damage response to double-strand breaks. Science 286, 1162-1166.

Crosera, M., Bovenzi, M., Maina, G., Adami, G., Zanette, C., Florio, C. and Larese, F. F., 2009. Nanoparticle dermal absorption and toxicity: a review of the literature. Int. Arch. Occup. Environ. Health 82, 1043-1055.

Cross, S. E., Innes, B., Roberts, M. S., Tsuzuki, T., Robertson, T. A. and McCormick, P., 2007. Human skin penetration of sunscreen nanoparticles: in-vitro assessment of

a novel micronized zinc oxide formulation. Skin Pharmacol. Physiol. 20, 148-154.

Cullinan, S. B., Gordan, J. D., Jin, J., Harper, J. W. and Diehl, J. A., 2004. The Keap1-BTB protein is an adaptor that bridges Nrf2 to a Cul3-based E3 ligase: oxidative stress sensing by a Cul3-Keap1 ligase. Mol. Cell. Biol. 24, 8477-8486.

Dai, R., 2010. IBISWorld Industry Report 54171 Scientific research and development in the U.S. Santa Monica, CA: IBISWorld Inc.

Damiani, E., Greci, L., Parsons, R. and Knowland, J., 1999. Nitroxide radicals protect DNA from damage when illuminated in vitro in the presence of dibenzoylmethane and a common sunscreen ingredient. Free Rad. Biol. 26, 809-816.

Damiano, J. S., Oliveira, V., Welsh, K. and Reed, J. C., 2004. Heterotypic interactions among NACHT domains: implications for regulation of innate immune responses. Biochem. J. 381, 213-219.

Das, G., Chan, P. P. Y., Teo, A., Loo, J. S. C., Anderson, J. M. and Tan, T. T. Y., 2009. In vitro cytotoxicity evaluation of biomedical nanoparticles and their extracts. J. Biomed. Mater. Part A 93A, 337-346.

Dean, R. T., Fu, S., Stocker, R. and Davies, M. J., 1997. Biochemistry and pathology of radical-mediated protein oxidation. Biochem. J. 324, 1-18.

Decher, G., 1997. Fuzzy nanoassemblies: toward layered polymeric multicomposites. Science 277, 1232-1237.

Delehanty, J. B., Mattoussi, H., Medintz, I. L., Mattoussi, H. and Clapp, A. R., 2008. Delivering quantum dots into cells: strategies, progress and remaining issues. Anal. Bioanal. Chem. 393, 1091-1105.

Delehanty, J. B., Medintz, I. L., Pons, T., Brunel, F. M., Dawson, P. E. and Mattoussi, H., 2006. Self-assembled quantum dot-peptide bioconjugates for selective intracellular delivery. Bioconj. Chem. 17, 920–927.

Deng, Z. J., Liang, M., Monteiro, M., Toth, I. and Minchin, R. F., 2011. Nanoparticle-induced unfolding of fibrinogen promotes Mac-1 receptor activation and inflammation. Nat. Nanotech. 6, 39-44.

Derfus, A. M., Chan, W. C. W. and Bhatia, S. N., 2004. Probing the cytotoxicity of semiconductor quantum dots. Nano Lett. 4, 11-18.

Djordjevic, A., Canadanovic-Brunet, J., Vojinovic-Miloradov, M. and Bogdanovic, G., 2005. Antioxidant properties and hypothetical radical mechanism of fullerol C60(OH)24. Oxi. Commun. 27, 213-218.

Dobrovolskaia, M. A., Aggarwal, P., Hall, J. B. and McNeil, S. E., 2008. Preclinical studies to understand nanoparticle interaction with the immune system and its potential effects on nanoparticle biodistribution. Mol. Pharm. 5, 487-495.

Donaldson, K., Aitken, R., Tran, L., Stone, V., Duffi, R., Forrest, G. and Alexander, A., 2006. Carbon nanotubes: a review of their properties in relation to pulmonary toxicology and workplace safety. Toxicol. Sci. 92, 5-22.

Droge, W., 2002. Free radicals in the physiological control of cell function. Physiol. Rev. 82, 47-95.

Duan, H. and Nie, S., 2007. Cell-penetrating quantum dots based on multivalent and endosome-disrupting surface coatings. J. Am. Chem. Soc. 129, 3333-3338.

Dubertret, B., Skourides, P., Norris, D. J., Noireaux, V., Brivanlou, A. H. and Libchaber, A., 2002. In vivo imaging of quantum dots encapsulated in phospholipid micelles. Science 298, 1759-1762.

Dunford, R., Salinaro, A., Cai, L., Serpone, N., Horikoshi, S., Hidaka, H. and Knowlan, J., 1997. Chemical oxidation and DNA damage catalysed by inorganic sunscreen ingredients. FEBS Lett. 418, 87-90.

Elvers, I., 2011. Replication fork stability in mammalian cells, Ph.D thesis, Stockholm University, Stockholm, Sweden.

Emerich, D. F. and Thanos, C. G., 2006. The pinpoint promise of nanoparticle-based drug delivery and molecular diagnosis. Biomol. Eng. 23, 171-184.

Eom, H. and Choi, J., 2009a. Oxidative stress of CeO2 nanoparticles via p38-Nrf-2 signaling pathway in human bronchial epithelial cell, Beas-2B. Tox. Lett. 187, 77-83.

Eom, H. and Choi, J., 2009b. Oxidative stress of silica nanoparticles in human bronchial epithelial cell, Beas-2B. Tox. In Vitro 23, 1326-1332.

Eom, H. and Choi, J., 2010. p38 MAPK activation, DNA damage, cell cycle arrest and apoptosis as mechanisms of toxicity of silver nanoparticles in Jurkat T cells. Environ. Sci. Technol. 44, 8337–8342.

EPA, 2007. Nanotechnology white paper. Prepared for the U.S. Environmental Protection Agency by members of the Nanotechnology Workgroup, U.S. Environmental Protection Agency, Washington, DC.

Fantuzzi, L., Spadaro, F., Purificato, C., Cecchetti, S., Podo, F., Belardelli, F., Gessani, S. and Ramoni, C., 2008. Phosphatidylcholine-specific phospholipase C activation is required for CCR5-dependent, NF-kB-driven CCL2 secretion elicited in response to HIV-1 gp120 in human primary macrophages. Blood 111, 3355-3363.

Fernandez-Capetillo, O., Chen, H., Celeste, A., Ward, I., Romanienko, P. J., Morales, J. C., Naka, K., Xia, Z., Camerini-Otero, R. D., Motoyama, N., Carpenter, P. B., Bonner, W. M., Chen, J. and Nussenzweig, A., 2002. DNA damage-induced G2–M checkpoint activation by histone H2AX and 53BP1. Nat. Cell. Biol. 4, 993-997.

Filon, F. L., D'Agostin, F., Crosera, M., Adami, G., Renzi, N., Bovenzi, M. and Maina, G., 2009. Human skin penetration of silver nanoparticles through intact and damaged skin. Toxicology 255, 33-37.

Filon, L. F., Boeninger, M., Maina, G., Adami, G., Spinelli, P. and Damian, A., 2006. Skin absorption of inorganic lead and the effects of skin cleansers. J. Occup. Environ. Med. 48, 692-699.

Finkel, T. and Holbrook, N. J., 2000. Oxidants, oxidative stress, and the biology of ageing. Nature 408, 239-247.

Ford, J. M. and Hanawalt, P. C., 1997. Expression of wild-type p53 is required for efficient global genomic nucleotide excision repair in UV-irradiated human fibroblasts. J. Biol. Chem. 272, 28073-28080.

Fraker, P. J. and Telford, W. G., 1997. A reappraisal of the role of zinc in life and death decisions of cells. Proc. Soc. Exp. Biol. Med. 215, 229-236.

Gaihre, B., Khil, M. S. and Kim, H. Y., 2011. In vitro anticancer activity of doxorubicin-loaded gelatin-coated magnetic iron oxide nanoparticles. J. Microencapsulation 28, 286-293.

Gao, X., Cui, Y., Levenson, R. M., Chung, L. W. K. and Nie, S., 2004. In vivo cancer targeting and imaging with semiconductor quantum dots. Nat. Biotechnol. 22, 969-976.

Gatei, M., Young, D., Cerosaletti, K. M., Desai-Mehta, A., Spring, K., Kozlov, S., Lavin, M. F., Gatti, R. A., Concannon, P. and Khanna, K., 2000. ATM-dependent phosphorylation of nibrin in response to radiation exposure. Nat. Genet. 25, 115-119.

Ge, Y., Bruno, M., Wallace, K., Winnik, W. and Prasad, R. Y., 2011. Proteome profiling reveals potential toxicity and detoxification pathways following exposure of BEAS-2B cells to engineered nanoparticle titanium dioxide. Proteomics 11, 2406-2422.

Gerion, D., Pinaud, F., Williams, S. C., Parak, W. J., Zanchet, D., Weiss, S. and Alivisatos, A. P., 2001. Synthesis and properties of biocompatible water-soluble

silica-coated CdSe/ZnS semiconductor quantum dots. J. Phys. Chem. B 105, 8861-8871.

Gopee, N. V., Roberts, D. W., Webb, P., Cozart, C. R., Siitonen, P. H., Latendresse, J. R., Warbitton, A. R., Yu, W. W., Colvin, V. L., Walker, N. J. and Howard, P. C., 2009. Quantitative determination of skin penetration of PEG-coated CdSe quantum dots in dermabraded but not intact SKH-1 hairless mouse skin. Toxicol. Sci. 111, 37-48.

Graham, B. and Gibson, S. B., 2005. The two faces of NFkappaB in cell survival responses. Cell Cycle 4, 1342-1345.

Greten, F. R., Eckmann, L., Greten, T. F., Park, J. M., Li, Z. W., Egan, L. J., Kagnoff, M. F. and Karin., M., 2004. IKKbeta links inflammation and tumorigenesis in a mouse model of colitis-associated cancer. Cell 118, 285-296.

Guma, M., Stepniak, D., Shaked, H., Spehlmann, M. E., Shenouda, S., Cheroutre, H., Vicente-Suarez, I., Eckmann, L., Kagnoff, M. F. and Karin, M., 2011. Constitutive intestinal NF-kB does not trigger destructive inflammation unless accompanied by MAPK activation. JEM 208, 1889-1900.

Guterres, S. S., Alves, M. P. and Pohlmann, A. R., 2006. Nanoparticles: health effects—pros and cons. Environ. Health Perspect. 114, 1818-1825.

Halliwell, B., 2007. Oxidative stress and cancer: have we moved forward? Biochem. J. 401, 1-11.

Halliwell, B., 2009. The wanderings of the free radical. Free Rad. Biol. 46, 531-542.

Hanasoge, S. and Ljungman, M., 2007. H2AX phosphorylation after UV irradiation is triggered by DNA repair intermediates and is mediated by the ATR kinase. Carcinogenesis 28, 2298-2304.

Hansen, S. F., Larsen, B. H., Olsen, S. I. and Baun, A., 2007. Categorization framework to aid hazard identification of nanomaterials. Nanotoxicology 1, 243-250.

Hild, W. A., Breunig, M. and Goepferich, A., 2008. Quantum dots: nano-sized probes for the exploration of cellular and intracellular targeting. Eur. J. Pharm. Biopharm. 68, 153-168.

Hillyer, J. F. and Albrecht, R. M., 2001. Gastrointestinal persorption and tissue distribution of differently sized colloidal gold nanoparticles. J. Pharm. Sci. 90, 1927-1936.

Hochino, T., Kurata, Y., Terasaki, Y. and Susa, K., 2001. Mechanism of polishing of SiO_2 films by CeO_2 particles. J. Non-Cryst. Solids 283, 129-136.

Hoshino, A., Fujioka, K., Oku, T., Suga, M., Sasaki, Y. F., Ohta, T., Yasuhara, M., Suzuki, K. and Yamamoto, K., 2004. Physicochemical properties and cellular toxicity of nanocrystal quantum dots depend on their surface modification. Nano Lett. 4, 2163–2169.

Hoshino, A., Hanada, S., Manabe, N., Nakayama, T. and Yamamoto, K., 2009. Immune response induced by fluorescent nanocrystal quantum dots in vitro and in vivo. IEEE Trans Nanobiosci. 8, 51-57.

Hsina, Y., Chena, C., Huanga, S., Shihc, T., Lai, P. and Chueha, P. J., 2008. The apoptotic effect of nanosilver is mediated by a ROS- and JNK-dependent

mechanism involving the mitochondrial pathway in NIH3T3 cells. Tox. Lett. 179, 130-139.

Huang, C. C., Aronstam, R. S., Chen, D. R. and Huang, Y. W., 2010. Oxidative stress, calcium homeostasis, and altered gene expression in human lung epithelial cells exposed to ZnO nanoparticles. Tox. In Vitro 24, 45-55.

Huber, M. A., Kraut, N., Addicks, T. and Peter, R. U., 2000. Cell-type-dependent induction of eotaxin and CCR3 by ionizing radiation. Biochem. Biophys. Res. Comm. 269, 546-552.

Hussain, S. M., Javorina, A. K., Schrand, A. M., Duhart, H. M., Ali, S. F. and Schlager, J. J., 2006. The interaction of manganese nanoparticles with PC-12 cells induces dopamine depletion. Toxicol. Sci. 92, 456-463.

Ipe, B. I., Lehnig, M. and Niemeyer, C. M., 2005. On the generation of free radical species from quantum dots. Small 1, 706–709.

Isakovic, A., Markovic, Z., Todorovic-Markovic, B., Nikolic, N., Vranjes-Djuric, S., Mirkovic, M., Dramicanin, M., Harhaji, L., Raicevic, N., Nikolic, Z. and Trajkovic, V., 2006. Distinct cytotoxic mechanisms of pristine versus hydroxylated fullerene. Toxicol. Sci. 91, 173-183.

Itoh, K., Chiba, T., Takahashi, S., Ishii, T., Igarashi, K., Katoh, Y., Oyake, T., Hayashi, N., Satoh, K., Hatayama, I., Yamamoto, M. and Nabeshima, Y., 1997. An Nrf2/small Maf heterodimer mediates the induction of phase II detoxifying enzyme genes through antioxidant response elements. Biochem. Biophys. Res. Commun. 236, 313-322.

Itoh, K., Tong, K. and Yamamoto, M., 2004. Molecular mechanism activating Nrf2-Keap1 pathway in regulation of adaptive response to electrophiles. Free Rad. Biol. Med. 36, 1208-1213.

Jacobsen, N. R., Pojana, G., White, P., Møller, P., Cohn, C. A., Korsholm, K. S., Vogel, U., Marcomini, A., Loft, S. and Wallin, H., 2008. Genotoxicity, cytotoxicity, and reactive oxygen species induced by single-walled carbon nanotubes and C(60) fullerenes in the FE1-Mutatrade mark mouse lung epithelial cells. Environ. Mol. Mut. 49, 476-487.

Jaiswal, J. K., Mattoussi, H., Mauro, J. M. and Simon, S. M., 2003. Longterm multiple color imaging of live cells using quantum dot bioconjugates. Nat. Biotechnol. 21, 47-51.

Jamieson, T., Bakhshi, R., Petrova, D., Pocock, R., Imani, M. and Seifalian, A. M., 2007. Biological applications of quantum dots. Biomaterials 28, 4717-4732.

Jani, P., Halbert, G. W., Langridge, J. and Florence, A. T., 1990. Nanoparticle uptake by the rat gastrointestinal mucosa: quantitation and particle size dependency. J. Pharm. Pharmacol. 442, 821-826.

Jazayeri, A., Falck, J., Lukas, C., Bartek, J., Smith, G. C., Lukas, J. and Jackson, S. P., 2006. ATM- and cell cycle-dependent regulation of ATR in response to DNA double-strand breaks. Nat. Cell Biol. 8, 37-45.

Jiang, G., Oberdörster, G., Elder, A., Gelein, R., Mercer, P. and Biswas, P., 2008. Does nanoparticle activity depend upon size and crystal phase? Nanotoxicology 2, 33-42.

Jung, H., Kittelson, D. and Zachariah, M., 2004. The influence of a cerium additive on ultrafine diesel particle emissions and kinetics of oxidation. Combust. Flame 142, 276-288.

Kaewamatawong, T., Kawamura, N., Okajima, M., Sawada, M., Morita, T. and Shimada, A., 2005. Acute pulmonary toxicity caused by exposure to colloidal silica: particle size dependent pathological changes in mice. Toxicol. Pathol. 33, 745-751.

Kamohara, H., Matsuyama, W., Shimozato, O., Abe, K., Galligan, C., Hashimoto, S., Matsushima, K. and Yoshimura, T., 2004. Regulation of tumour necrosis factor-related apoptosis-inducing ligand (TRAIL) and TRAIL receptor expression in human neutrophils. Immunology 111, 186-194.

Kaneko, Y. S., Watanabe, N., Morisaki, H., Akita, H., Fujimoto, A., Tominaga, K., Terasawa, M., Tachibana, A., Ikeda, K. and Nakanishi, M., 1999. Cell-cycle-dependent and ATM-independent expression of human Chk1 kinase. Oncogene 18, 3673-3681.

Kielhorn, J., Melching-Kollmuss, S. and Mangelsdorf, I., 2006. Controversial topics in the assessment of dermal absorption, World Health Organization, Dermal Absorption Geneva, pp. 112-123.

Kim, E. Y., Koh, J. Y., Kim, Y. H., Sohn, S., Joe, E. and Gwag, B. J., 1999. Zn2+ entry produces oxidative neuronal necrosis in cortical cell cultures. Eur. J. Neurosci. 11, 327-334.

Kim, S. and Bawendi, M. G., 2003. Oligomeric ligands for luminescent and stable nanocrystal quantum dots. J. Am. Chem. Soc. 125, 14652-14653.

Kirchner, C., Javier, A. M., Susha, A. S., Rogach, A. L., Kreft, O., Sukhorukov, G. B. and Parak, W. J., 2005a. Cytotoxicity of nanoparticle-loaded polymer capsules. Talanta 67, 486-491.

Kirchner, C., Liedl, T., Kudera, S., Pellegrino, T., Javier, A. M., Gaub, H. E., Stolzle, S., Fertig, N. and Parak, W. J., 2005b. Cytotoxicity of colloidal CdSe and CdSe/ZnS nanoparticles. Nano Lett. 5, 331–338.

Klumpp, C., Kostarelos, K., Prato, M. and Bianco, A., 2006. Functionalized carbon nanotubes as emerging nanovectors for the delivery of therapeutics. Biochem. Biophys. Acta 1758, 404-412.

Knowland, J., McKenzie, E. A., McHugh, P. J. and Cridland, N. A., 1993. Sunlight-induced mutagenicity of a common sunscreen ingredient. FEBS Lett. 324, 309-313.

Kobayashi, K., Kang, M., Okawa, H., Ohtsuji, M., Zenke, Y., Chiba, T., Igarashi, K., and Yamamoto, M., 2004. Oxidative stress sensor Keap1 functions as an adaptor for Cul3-based E3 ligase to regulate proteasomal degradation of Nrf2. Mol. Cell. Biol. 24, 7130-7139.

Kopf, M., Baumann, H., Freer, G., Freudenberg, M., Lamers, M., Kishimoto, T., Zinkernagel, R., Bluethmann, H. and Köhler, G., 1994. Impaired immune and acute-phase responses in interleukin-6-deficient mice. Nature 368, 339-342.

Korus, M., Mahon, G. M., Cheng, L. and Whitehead, I. P., 2002. p38 MAPK-mediated activation of NF-kappaB by the RhoGEF domain of Bcr. Oncogene 21, 4601-4612.

Kurosu, T., Takahashi, Y., Fukuda, T., Koyama, T., Miki, T. and Miura, O., 2005. p38 MAP kinase plays a role in G2 checkpoint activation and inhibits apoptosis of human B cell lymphoma cells treated with etoposide. Apoptosis 10, 1111-1120.

Kwong, M., Kan, Y. W. and Chan, J. Y., 1999. The CNC basic leucine zipper factor, Nrf1, is essential for cell survival in response to oxidative stress-inducing agents. J. Biol. Chem. 274, 37491-37498.

Lademann, J., Weigmann, H. J., Rickmeyer, C., Barthelmes, H., Schaefer, H., Mueller, G. and Sterry, W., 1999. Penetration of titanium dioxide in sunscreen formulation into the horny layer and the follicular orifice. Skin Pharmacol. Appl. Skin Physiol. 12, 247-256.

Larese, F. F., D'Agostin, F., Crosera, M., Adami, G., Renzi, N., Bovenzi, M. and Maina, G., 2009. Human skin penetration of silver nanoparticles through intact and damaged skin. Toxicology 255, 33-37.

Le, J., Weinstein, D., Gubler, U. and Vilcek, J., 1987. Induction of membrane associated interleukin-1 by tumor necrosis factor in human fibroblasts. J .Immunol. 138, 2137-2142.

Lee, H., Shin, D., Song, H., Yuk, J., Lee, Z., Lee, S., Hwang, S. M., Kim, J., Lee, C. and Jo, E., 2009. Nanoparticles up-regulate tumor necrosis factor-! and CXCL8 via

reactive oxygen species and mitogen-activated protein kinase activation. Toxicol. Appl. Pharmacol. 238, 160-169.

Lee, J. H. and Paull, T. T., 2005. ATM activation by DNA double-strand breaks through the Mre11- Rad50-Nbs1 complex. Science 308, 551-554.

Li, J., Stein, T. and Johnson, J., 2004. Genetic dissection of systemic autoimmune disease in Nrf2-deficient mice. Physiol. Genomics 18, 261-272.

Li, Z. B., Cai, W. and Chen, X., 2007. Semiconductor quantum dots for in vivo imaging. J. Nanosci. Nanotech. 7, 2567-2581.

Limbach, L. K., Wick, P., Manser, P., Grass, R. N., Bruinink, A. and Stark, W. J., 2007. Exposure of engineered nanoparticles to human lung epithelial cells: influence of chemical composition and catalytic activity on oxidative stress. Environ. Sci. Technol. 41, 4158-4163.

Lin, W., Huang, Y., Zhou, X. and Ma, Y., 2006. *In vitro* toxicity of silica nanoparticles in human lung cancer cells. Toxicol. Appl. Pharmacol. 217, 252-259.

Lipovsky, A., Nitzan, Y., Gedanken, A. and Lubart, R., 2011. Antifungal activity of ZnO nanoparticles—the role of ROS mediated cell injury. Nanotechnology 22, 105101.

Liu, Z. G., Hsu, H., Goeddel, D. V. and Karin, M., 1996. Dissection of TNF receptor 1 effector functions: JNK activation is not linked to apoptosis while NF-kappaB activation prevents cell death. Cell 87, 565-576.

Livak, K. J. and Schmittgen, T. D., 2001. Analysis of relative gene expression data using real-time quantitative PCR and the 22DDCT method. Methods 25, 402–408.

Livolsi, A., Busuttil, V., Imbert, V., Abraham, R. T. and Peyron, J. F., 2001. Tyrosine phosphorylation-dependent activation of NF-kappaB. Eur. J. Biochem. 268, 1508-1515.

Lukas, C., Bartkova, J., Latella, L., Falck, J., Mailand, N., Schroeder, T., Sehested, M., Lukas, J. and Bartek, J., 2001. DNA damage-activated kinase Chk2 is independent of proliferation or differentiation yet correlates with tissue biology. Cancer Res. 61, 4990-4993.

Lunov, O., Syrovets, T., Büchele, B., Jiang, X., Röcker, C., Tron, K., Nienhaus, G. U., Walther, P., Mailänder, V., Landfester, K. and Simmet, T., 2010. The effect of carboxydextran-coated superparamagnetic iron oxide nanoparticles on c-Jun N-terminal kinase-mediated apoptosis in human macrophages. Biomaterials 31, 5063-5071.

Mahendra, S., Zhu, H., Colvin, V. L. and Alvarez, P. J., 2008. Quantum dot weathering results in microbial toxicity. Environ. Sci. Technol. 42, 9424–9430.

Manke, I. A., Nguyen, A., Lim, D., Stewart, M. Q., Elia, A. E. and Yaffe, M. B., 2005. MAPKAP kinase-2 is a cell cycle checkpoint kinase that regulates the G2/M transition and S phase progression in response to UV irradiation. Mol. Cell 17, 37-48.

Marchesiello, M. and Genies, E., 1993. A theoretical model for an amperometric glucose sensor using polypyrrole as the immobilization matrix. J. Electroanal. Chem. 358, 35-48.

Masui, T., Hirai, H., Hamada, R., Imanaka, N., Adachi, G., Sakata, T. and Mori, H., 2003. Synthesis and characterization of cerium oxide nanoparticles coated with turbostratic boron nitride. J. Mater. Chem. 13, 622-627.

Maynard, A. D. and Kuempel, E. D., 2005. Airborne nanostructured particles and occupational health. J. Nanopart. Res. 7, 587-614.

McFarland-Mancini, M. M., Funk, H. M., Paluch, A. M., Zhou, M., Giridhar, P. V., Mercer, C. A., Kozma, S. C. and Drew, A. F., 2010. Differences in wound healing in mice with deficiency of IL-6 versus IL-6 receptor. J. Immunol. 184, 7219-7228.

McNichols, R. J. and Cote, G. L., 2000. Optical glucose sensing in biological fluids: an overview. J. Biomed. Opt. 5, 5-16.

McShane, M. and Ritter, D., 2010. Microcapsules as optical biosensors. J. Mat. Chem. 20, 8189-8193.

McShane, M. J., 2002. Potential for glucose monitoring with nanoengineered fluorescent biosensors. Diab. Technol. Ther. 4, 533-538.

McShane, M. J., 2006. Microcapsules as "smart tattoo" glucose sensors: engineering systems with enzymes and glucose-binding sensing elements. In Geddes C. D. and Lakowicz J. R. (Eds.), Vol. 11, Springer, New York.

Medintz, I. L., Mattoussi, H. and Clapp, A. R., 2008. Potential clinical applications of quantum dots. Int. J. Nanomed. 3, 151.

Medintz, I. L., Uyeda, H. T., Goldman, E. R. and Mattoussi, H., 2005. Quantum dot bioconjugates for imaging, labelling and sensing. Nat. Mater. 4, 435-446.

Miao, A., Zhang, X., Luo, Z., Chen, C., Chin, W., Santschi, P. H. and Quigg, A., 2010. Zinc oxide-engineered nanoparticles: dissolution and toxicity to marine phytoplankton. Environ. Toxicol. Chem. 29, 2814-2822.

Michalet, X., Pinaud, F. F., Bentolila, L. A., Tsay, J. M., Doose, S., Li, J. J., Sundaresan, G., Wu, A. M., Gambhir, S. S. and Weiss, S., 2005. Quantum dots for live cells, in vivo imaging, and diagnostics. Science 307, 538–544.

Mikhailov, A., Shinohara, M. and Rieder, C. L., 2005. The p38-mediated stress-activated checkpoint: a rapid response system for delaying progression through antephase and entry into mitosis. Cell Cycle 4, 57-62.

Mirkov, S. M., Djordjevic, A., Andric, N. L., Andric, S. A., Kostic, T. S., Bogdanovic, G. M., Vojinovic-Miloradovc, M. B. and Kovacevic, R. Z., 2004. Nitric oxide-scavenging activity of polyhydroxylated fullerenol, C60(OH)24. Nitric Oxide 11, 201-207.

Mitchnick, M. A., Fairhurst, D. and Pinnell, S. R., 1999. Microfine zinc oxide (Z-Cote) as a photostable UVA/UVB sunblock agent. J. Am. Acad. Dermatol. 40, 85-89.

Miura, M., Zhu, H., Rotello, R., Hartwieg, E. A. and Yuan, J., 1993. Induction of apoptosis in fibroblasts by IL-1-beta-converting enzyme, a mammalian homolog of the c-elegans cell-death gene ced-3. Cell 75, 653-660.

Mocchegiani, E., Muzzioli, M. and Giacconi, R., 2000. Zinc and immunoresistance to infection in aging: new biological tools. Trends Pharmacol. Sci. 21, 205-208.

Moghimi, S. M. and Gray, T., 1997. A single dose of intravenously injected poloxamine-coated long-circulating particles triggers macrophage clearance of subsequent doses in rats. Clin. Sci. 93, 371-379.

Moghimi, S. M. and Szebeni, J., 2003. Stealth liposomes and long circulating nanoparticles: critical issues in pharmacokinetics, opsonization and protein-binding properties. Prog. Lipid Res. 42, 463-478.

Molnar, A., Theodoras, A. M., Zon, L. I. and Kyriakis, J. M., 1997. Cdc42Hs, but not Rac1, inhibits serum-stimulated cell cycle progression at G1/S through a mechanism requiring p38/RK*. J. Biol. Chem. 272, 13229–13235.

Monteiller, C., Tran, L., MacNee, W., Faux, S., Jones, A., Miller, B. and Donaldson, K., 2007. The pro-inflammatory effects of low-toxicity low-solubility particles, nanoparticles and fine particles, on epithelial cells in vitro: the role of surface area. Occup. Environ. Med. 64, 609-615.

Mortensen, L. J., Oberdörster, G., Pentland, A. P. and Delouise, L. A., 2008. In vivo skin penetration of quantum dot nanoparticles in the murine model: the effect of UVR. Nano Lett. 8, 2779-2787.

Mroz, R. M., Schins, R. P. F., Li, H., Drost, E. M., Macnee, W. and Donaldson, K., 2007. Nanoparticle carbon black driven DNA damage induces growth arrest and AP-1 and NF-kB DNA binding in lung epithelial A549 cell line. J Physiol. Pharmacol. 58, 461-470.

Mroz, R. M., Schins, R. P. F., Li, H., Jimenez, L. A., Drost, E. M., Holownia, A., MacNee, W. and Donaldson, K., 2008. Nanoparticle-driven DNA damage mimics irradiation-related carcinogenesis pathways. Eur. Respir. J. 31, 241-251.

Müller, M., Morotti, A. and Ponzetto, C., 2002. Activation of NF-κB is essential for hepatocyte growth factor-mediated proliferation and tubulogenesis. Mol. Cell Biol. 22, 1060-1072.

Murphree, L. J., Sullivan, G. W., Marshall, M. A. and Linden, J., 2005. Lipopolysaccharide rapidly modifies adenosine receptor transcripts in murine and human macrophages: role of NF-kB in A2A adenosine receptor induction. Biochem. J. 391, 575-580.

Nann, T., 2005. Phase-transfer of CdSe/ZnS quantum dots using amphiphilic hyperbranched polyethylenimine. Chem. Comm. 13, 1735-1736

Nanoscale Science Engineering and Technology Subcommittee, 2004. US National Science and Technology Council. The national nanotechnology initiative: strategic plan http://www.nano.gov/NNI_Strategic_Plan_2004.pdf

Nasterlack, M., Zober, A. and Oberlinner, C., 2008. Considerations on occupational medical surveillance in employees handling nanoparticles. Int. Arch. Occup. Environ. Health 81, 721-726.

National Institute of Occupational Safety and Health (NIOSH), 2007. Progress toward safe nanotechnology in the workplace—a report from the NIOSH Nanotechnology Research Center #2007-123 http://www.cdc.gov/niosh.

National Institute of Standards and Technology (NIST), 2009. US Dept of Commerce. Environmental leaching of nanoparticles from consumer products http://www.nist.gov/mml/analytical/inorganic/leachnano.cfm.

Nel, A., Xia, T., Madler, L. and Li, N., 2006. Toxic potential of materials at the nanolevel. Science 311, 622-627.

Nguyen, T., Yang, C. and Pickett, C., 2004. The pathways and molecular mechanisms regulating Nrf2 activation in response to chemical stress. Free Rad. Biol. Med. 37, 433-441.

Nielsen, J. B., 2005. Percutaneous penetration through slightly damaged skin. Arch. Dermatol. Res. 296, 560-567.

Nielsen, J. B., Nielsen, F. and Sørensen, J. A., 2007. Defense against dermal exposures is only skin deep: significantly increased penetration through slightly damaged skin. Arch. Dermatol. Res. 299, 423-431.

Norbury, C., Blow, J. and Nurse, P., 1991. Regulatory phosphorylation of the p34cdc2 protein kinase in vertebrates. EMBO J. 10, 3321-3329.

Oberdorster, G., 2010. Safety assessment for nanotechnology and nanomedicine: concepts of nanotoxicology. J. Int. Med. 267, 89-105.

Oberdorster, G., Ferin, J. and Lehnert, B., 1994. Correlation between particle size, in vivo particle persistence, and lung injury. Environ. Health Perspect. 102, 173-179.

Oberdorster, G., Oberdorster, E. and Oberdorster, J., 2005. Nanotoxicology: an emerging discipline evolving from studies of ultrafine particles. Environ. Health Perspect. 113, 823-839.

Oberdorster, G., Stone, V. and Donaldson, K., 2007. Toxicology of nanoparticles: a historical perspective. Nanotoxicology 1, 2-25.

Ohta, A. and Sitkovsky, M., 2001. Role of G-protein-coupled adenosine receptors in downregulation of inflammation and protection from tissue damage. Nature 414, 916-920.

Pacurari, M., Yin, X. J., Zhao, J., Ding, M., Leonard, S. S., Schwegler-Berry, D., Ducatman, B. S., Sbarra, D., Hoover, M. D., Castranova, V. and Vallyathan, V., 2008. Raw single-wall carbon nanotubes induce oxidative stress and activate MAPKs, AP-1, NF-κB, and Akt in normal and malignant human mesothelial cells. Environ. Health Perspect. 116, 1211-1217.

Park, E., Yi, J., Kim, Y., Choi, K. and Park, K., 2010. Silver nanoparticles induce cytotoxicity by a Trojan-horse type mechanism. Tox. In Vitro 24, 872-878.

Parthasarathy, R. V. and Martin, C. R., 1994. Synthesis of polymeric microcapsule arrays and their use for enzyme immobilization. Nature 369, 298-301.

Parthasarathy, R. V. and Martin, C. R., 1998. Enzyme and chemical encapsulation in polymeric microcapsules. J. Appl. Polymer Sci. 62, 875-886.

Pastore, A., Piemonte, F., Locatelli, M., Russo, A. L., Gaeta, L. M., Tozzi, G. and Federici, G., 2003. Determination of blood total, reduced, and oxidized glutathione in pediatric subjects. Clin. Chem. 47, 1467-1469.

Paull, T. T., Rogakou, E. P., Yamazaki, V., Kirchgessner, C. U., Gellert, M. and Bonner, W. M., 2000. A critical role for histone H2AX in recruitment and repair factors to nuclear foci after DNA damage. Current Biol. 10, 886-895.

Peng, Z. A. and Peng, X., 2001. Formation of high-quality CdTe, CdSe, and CdS nanocrystals using CdO as precursor. J. Am. Chem. Soc. 123, 183-184.

Peters, A., Wichmann, H. E., Tuch, T., Heinrich, J. and Heyder, J., 1997. Respiratory effects are associated with the number of ultrafine particles. Am. J. Respir. Crit. Care Med. 155, 1376-1383.

Petrini, J. H. and Stracker, T. H., 2003. The cellular response to DNA double-strand breaks: defining the sensors and mediators. Trends Cell Biol. 13, 458-462.

Petrov, A. I., Volodkin, D. V. and Sukhorukov, G. B., 2005. Protein-calcium carbonate coprecipitation: a tool for protein encapsulation. Biotech. Prog. 21, 918-925.

Pinnell, S. R., Fairhurst, D., Gillies, R., Mitchnick, M. A. and Kollias, N., 2001. Microfine zinc oxide is a superior sunscreeningredient to microfine titanium dioxide. Dermatol. Surg. 26, 309-314.

Podhorecka, M., Skladanowski, A. and Bozko, P., 2010. H2AX phosphorylation: its role in DNA damage response and cancer therapy. J. Nucl. Acids 2010, 920161.

Pompella, A., Visvikis, A., Paolicchi, A., Tata, V. D. and Casini, A. F., 2003. The changing faces of glutathione, a cellular protagonist. Biochem. Pharmacol. 66, 1499-1503.

Prasad, B. R., Nikolskaya, N., Connolly, D., Smith, T. J., Byrne, S. J., Gerard, V. A., Gun'ko, Y. K. and Rochev, Y., 2010. Long-term exposure of CdTe quantum dots

on PC12 cellular activity and the determination of optimum non-toxic concentrations for biological use. J. Nanobiotech. 8, 7.

Prasad, R. Y., Wallace, K., Tennant, A. H., Kitchin, K. T., Kligerman, A. D. and Blackman, C. F., 2009. US EPA Office of Research and Development, The genotoxicity of titanium dioxide and cerium oxide nanoparticles in vitro [abstract]. http://cfpub.epa.gov/si/si_public_record_report.cfm?dirEntryId=216689.

Priester, J. H., Stoimenov, P. K., Mielke, R. E., Webb, S. M., Ehrhardt, C., Zhang, J. P., Stucky, G. D. and Holden, P. A., 2009. Effects of soluble cadmium salts versus CdSe quantum dots on the growth of planktonic pseudomonas aeruginosa. Environ. Sci. Technol. 43, 2589-2594.

Przybytkowski, E., Behrendt, M., Dubois, D. and Maysinger, D., 2009. Nanoparticles can induce changes in the intracellular metabolism of lipids without compromising cellular viability. FEBS J. 276, 6204-6217.

Pujalté, I., Passagne, I., Brouillaud, B., Tréguer, M., Durand, E., Ohayon-Courtès, C. and L'Azou, B., 2011. Cytotoxicity and oxidative stress induced by different metallic nanoparticles on human kidney cells. Part. Fib. Toxicol. 8, 1.

Rahman, I., Yang, S. R. and Biswas, S. K., 2006. Current concepts of redox signaling in the lungs. Antioxid. Redox Signal. 8, 681-689.

Rallo, R., France, B., Liu, R., Nair, S., George, S., Damoiseaux, R., Giralt, F., Nel, A., Bradley, K. and Cohen, Y., 2011. Self-organizing map analysis of toxicity-

related cell signaling pathways for metal and metal oxide nanoparticles. Environ. Sci. Technol. 45, 1695–1702.

Ramage, L., Proudfoot, L. and Guy, K., 2004. Expression of C-reactive protein in human lung epithelial cells and upregulation by cytokines and carbon particles. Inh. Toxicol. 16, 607–613.

Rancan, F., Rosan, S., Boehm, F., Cantrell, A., Brellreich, M., Schoenberger, H., Hirsch, A. and Moussa, F., 2002. Cytotoxicity and photocytotoxicity of a dendritic C-60 mono-adduct and a malonic acid C-60 tris-adduct on Jurkat cells. J. Photochem. Photobiol. B-Biol 67, 157-162.

Rehberg, M., Praetner, M., Leite, C. F., Reichel, C. A., Bihari, P., Mildner, K., Duhr, S., Zeuschner, D. and Krombach, F., 2010. Quantum dots modulate leukocyte adhesion and transmigration depending on their surface modification. Nano Lett. 10, 3656–3664.

Reinhardt, H. C., Aslanian, A. S., Lees, J. A. and Yaffe, M. B., 2007. p53-deficient cells rely on ATM- and ATR-mediated checkpoint signaling through the p38MAPK/MK2 pathway for survival after DNA damage. Cancer Cell 11, 175-189.

Reinhardt, H. C. and Yaffe, M. B., 2009. Kinases that control the cell cycle in response to DNA damage: Chk1, Chk2, and MK2. Curr. Opin. Cell Biol. 21, 245-255.

Ridley, S. H., Sarsfield, S. J., Lee, J. C., Bigg, H. F., Cawston, T. E., Taylor, D. J., DeWitt, D. L. and Saklatvala, J., 1997. Actions of IL-1 are selectively controlled

by p38 mitogen-activated protein kinase: regulation of prostaglandin H synthase-2, metalloproteinases, and IL-6 at different levels. J. Immunol. 158, 3165-3173.

Roberts, W. J. and Sloan, K. B., 2000. Prediction of transdermal flux of prodrugs of 5-fluorouracil, theophylline, and 6-mercaptopurine with a series/parallel model. J. Pharm. Sci. 89, 1415-1431.

Roco, M. C., 2003. Broader societal issues of nanotechnology. J. Nanopart. Res. 5, 181–189.

Romoser, A., Ritter, D., Majitha, R., Meissner, K. E., McShane, M. and Sayes, C. M., 2011a. Mitigation of quantum dot cytotoxicity by microencapsulation. PLoS ONE 6, e22079 doi:10.1371/journal.pone.0022079.

Romoser, A. A., Chen, P. L., Berg, J. M., Seabury, C., Ivanov, I., Criscitiello, M. F. and Sayes, C. M., 2011b. Quantum dots trigger immunomodulation of the NFκB pathway in human skin cells. Mol. Immunol. 48, 1349-1359.

Rouse, J. G., Yang, J., Ryman-Rasmussen, J. P., Barron, A. R. and Monteiro-Riviere, N. A., 2007. Effects of mechanical flexion on the penetration of fullerene amino acid-derivatized peptide nanoparticles through skin. Nano Lett. 7, 155-160.

Ryman-Rasmussen, J. P., Riviere, J. E. and Monteiro-Riviere, N. A., 2006. Penetration of intact skin by quantum dots with diverse physicochemical properties. Toxicol. Sci. 91, 159-165.

Ryman-Rasmussen, J. P., Riviere, J. E. and Monteiro-Riviere, N. A., 2007. Surface coatings determine cytotoxicity and irritation potential of quantum dot nanoparticles in epidermal keratinocytes. J. Invest. Dermatol. 127, 143–153.

Ryman-Rasmussen, J. P., Riviere, J. E. and Monteiro-Riviere, N. A., 2007b. Variables influencing interactions of untargeted quantum dot nanoparticles with skin cells and identification of biochemical modulators. Nano Lett. 7, 1344–1348.

Rzigalinski, B. A. and Strobl, J. S., 2009. Cadmium-containing nanoparticles: perspectives on pharmacology and toxicology of quantum dots. Toxicol. Appl. Pharmacol. 238, 280-288.

Samberg, M., Oldenburg, S. and Monteiro-Riviere, N., 2010. Evaluation of silver nanoparticle toxicity in skin in vivo and keratinocytes in vitro. Environ. Health Perspect. 118, 407-413.

Sanjiv, D., Sharma, A. K., Arora, R. C., Slezak, J. and Singal, P. K., 2009. IL-10 attenuates TNF-a-induced NFkB pathway activation and cardiomyocyte apoptosis. Cardiovasc. Res. 82, 59-66.

Saraiva, M. and O'Garra, A., 2010. The regulation of IL-10 production by immune cells. Nat. Rev. Immunol. 10, 170-181.

Sayes, C. M., Fortner, J. D., Guo, W., Lyon, D., Boyd, A. M., Ausman, K. D., Tao, Y. J., Sitharaman, B., Wilson, L. J., Hughes, J. B., West, J. L. and Colvin, V. L., 2004. The differential cytotoxicity of water-soluble fullerenes. Nano Lett. 4, 1881-1887.

Sayes, C. M., Gobin, A. M., Ausman, K. D., Mendez, J., West, J. L. and Colvin, V. L., 2005. Nano-C60 cytotoxicity is due to lipid peroxidation. Biomaterials 26, 7587–7595.

Scheuplein, R. J., 1967. Mechanisms of percutaneous absorption, II: transient diffusion and the relative importance of various routes of skin penetration. J. Invest. Dermatol. 48, 79-88.

Schins, R., 2002. Mechanisms of genotoxicity of particles and fibers. Inh. Toxicol. 14, 57-78.

Schmidt, C., 2009. Nanotechnology-related environment, health, and safety research: examining the national strategy. Environ. Health Perspect. 117, A158-A161.

Schulte, P. A., Geraci, C., Zumwalde, R., Hoover, M. and Kuempel, E., 2008. Occupational risk management of engineered nanoparticles. J. Occup. Environ. Hyg. 5, 239-249.

Semmler-Behnke, M., Takenaka, S., Fertsch, S., Wenk, A., Seitz, J., Mayer, P., Oberdorster, G. and Kreyling, W. G., 2007. Efficient elimination of inhaled nanoparticles from the alveolar region: evidence for interstitial uptake and subsequent reentrainment onto airway epithelium. Environ. Health Perspect. 115, 728-733.

Senzui, M., Tamura, T., Miura, K., Ikarashi, Y., Watanabe, Y. and Fujii, M., 2010. Study on penetration of titanium dioxide (TiO(2)) nanoparticles into intact and damaged skin in vitro. J. Toxicol. Sci. 35, 107-113.

Serpone, N., Dondi, D. and Albini, A., 2007. Inorganic and organic UV filters: their role and efficacy in sunscreens and suncare products. Inorg. Chim. Acta 360, 794-802.

Sharma, V., Singh, S. K., Anderson, D., Tobin, D. J. and Dhawan, A., 2011. Zinc oxide nanoparticle induced genotoxicity in primary human epidermal keratinocytes. J. Nanosci. Nanotechnol. 11, 3782-3788.

She, Q. B., Bode, A. M., Ma, W. Y., Chen, N. Y. and Dong, Z., 2001. Resveratrol-induced activation of p53 and apoptosis is mediated by extracellular-signal-regulated protein kinases and p38 kinase. Cancer Res. 61, 1604-1610.

She, Q. B., Chen, N. and Dong, Z., 2000. ERKs and p38 kinase phosphorylate p53 protein at serine 15 in response to UV radiation. J. Biol. Chem. 275, 20444-20449.

Shimada, A., Kawamura, N., Okajima, M., Kaewamatawong, T., Inoue, H. and Morita, T., 2006. Translocation pathway of the intratracheally instilled ultrafine particles from the lung into the blood circulation in the mouse. Toxicol. Pathol. 34, 949-957.

Shukla, R., Bansal, V., Chaudhary, M., Basu, A., Bhonde, R. R. and Sastry, M., 2005. Biocompatibility of gold nanoparticles and their endocytotic fate inside the cellular compartment: a microscopic overview. Langmuir 21, 10644-10654.

Siliciano, J. D., Canman, C. E., Taya, Y., Sakaguchi, K., Appella, E. and Kastan, M. B., 1997. DNA damage induces phosphorylation of the amino terminus of p53. Genes Dev. 11, 3471-3481.

Sonavane, G., Tomoda, K., Sano, A., Ohshima, H., Terada, H. and Makino, K., 2008. In vitro permeation of gold nanoparticles through rat skin and rat intestine: effect of particle size. Coll. Surf. B: Biointerfaces 65, 1-10.

Song, W., Zhang, J., Guo, J., Zhang, J., Ding, F., Li, L. and Sun, Z., 2010. Role of the dissolved zinc ion and reactive oxygen species in cytotoxicity of ZnO nanoparticles. Tox Lett. 199, 389-397.

Stewart, G. S., Wang, B., Bignell, C. R., Taylor, A. M. R. and Elledge, S. J., 2003. MDC1 is a mediator of the mammalian DNA damage checkpoint. Nature 421, 961-966.

Stoeger, T., Takenaka, S., Frankenberger, B., Ritter, B., Karg, E., Maier, K., Schulz, H. and Schmid, O., 2009. Deducing in vivo toxicity of combustion-derived nanoparticles from a cell-free oxidative potency assay and metabolic activation of organic compounds. Environ. Health Perspect. 117, 54-60.

Stone, V., Shaw, J., Brown, D. M., Macnee, W., Faux, S. P. and Donaldson, K., 1998. The role of oxidative stress in the prolonged inhibitory effect of ultrafine carbon black on epithelial cell function. Tox. In Vitro 12, 649-659.

Su, Y., He, Y., Lu, H., Sai, L., Li, Q., Li, W., Wang, L., Shen, P., Huang, Q. and Fan, C., 2009. The cytotoxicity of cadmium based, aqueous phase – Synthesized, quantum dots and its modulation by surface coating. Biomaterials 30, 19-25.

Sun, Y., Jiang, X., Chen, S., Fernandes, N. and Price, B. D., 2005. A role for the Tip60 histone acetyltransferase in the acetylation and activation of ATM. PNAS 102, 13182-13187.

Sydlik, U., Bierhals, K., Soufi, M., Abel, J., Schins, R. P. F. and Unfried, K., 2006. Ultrafine carbon particles induce apoptosis and proliferation in rat lung epithelial

cells via specific signaling pathways both using EGF-R. Lung Cell. Mol. Phys. 291, L725-L733.

Tang, M., Xing, T., Zeng, J., Wang, H., Li, C., Yin, S., Yan, D., Deng, H., Liu, J., Wang, M., Chen, J. and Ruan, D. Y., 2008. Unmodified CdSe quantum dots induce elevation of cytoplasmic calcium levels and impairment of functional properties of sodium channels in rat primary cultured hippocampal neurons. Environ. Health Perspect. 116, 915–922.

Thannickal, V. J. and Fanburg, B. L., 2000. Reactive oxygen species in cell signaling. Am. J. Physiol. Lung Cell. Mol. Physiol. 279, L1005-L1028.

The Royal Society and The Royal Academy of Engineering, 2004. Nanoscience and nanotechnology: opportunities and uncertainties, http://www.nanotec.org.uk.

Thornton, T. M. and Rincon, M., 2009. Non-classical p38 map kinase functions: cell cycle checkpoints and survival. Int. J. Biol. Sci. 5, 44-51.

Tinkle, S. S., Antonini, J. M., Rich, B. A., Roberts, J. R., Salmen, R., DePree, K. and Adkins, E. J., 2003. Skin as a route of exposure and sensitization in chronic beryllium disease. Environ. Health Perspect. 111, 1202-1208.

Toyokuni, S. and Akatsuka, S., 2007. Pathological investigation of oxidative stress in the post-genomic era. Pathol. Int. 57, 461-473.

Trincavelli, M. L., Falleni, A., Chelli, B., Tuscano, D., Costa, B., Gremigni, V., Lucacchini, A. and Martini, C., 2003. A(2A) adenosine receptor ligands and proinflammatory cytokines induce PC 12 cell death through apoptosis. Biochem. Pharmacol. 66, 1953-1962.

Trouiller, B., Reliene, R., Westbrook, A., Solaimani, P. and Schiestl, R. H., 2009. Titanium dioxide nanoparticles induce DNA damage and genetic instability in vivo in mice. Cancer Res. 69, 8784-8789.

Truong-Tran, A. Q., Carter, J., Ruffin, R. E. and Zalewski, P. D., 2001. The role of zinc in caspase activation and apoptotic cell death. Biometals 14, 315-330.

Uboldi, C., Bonacchi, D., Lorenzi, G., Hermanns, M. I., Pohl, C., Baldi, G., Unger, R. E. and Kirkpatrick, C. J., 2009. Gold nanoparticles induce cytotoxicity in the alveolar type-II cell lines A549 and NCIH441. Part. Fib. Toxicol. 6, 18.

Unfried, K., Sydlik, U., Bierhals, K., Weissenberg, A. and Abel, J., 2008. Carbon nanoparticle-induced lung epithelial cell proliferation is mediated by receptor-dependent Akt activation. Lung Cell. Mol. Phys. 294, L358-L367.

Vandesompele, J., De Preter, K., Pattyn, F., Poppe, B., Van Roy, N., De Paepe, A. and Speleman, F., 2002. Accurate normalization of real-time quantitative RT-PCR data by geometric averaging of multiple internal control genes. Gen. Biol. 3, 1-11.

Venugopal, R. and Jaiswal, A. K., 1996. Nrf1 and Nrf2 positively and c-Fos and Fra1 negatively regulate the human antioxidant response element-mediated expression of NAD(P)H: quinone oxidoreductase1 gene. PNAS 93, 14960-14965.

Venugopal, R. and Jaiswal, A. K., 1998. Nrf2 and Nrf1 in association with Jun proteins regulate antioxidant response element-mediated expression and coordinated induction of genes encoding detoxifying enzymes. Oncogene 17, 3145-3156.

Vogt, A., Combadiere, B., Hadam, S., Stieler, K. M., Lademann, J., Schaefer, H., Autran, B., Sterry, W. and Blume-Peytav, U., 2006. 40 nm, but not 750 or 1,500 nm, nanoparticles enter epidermal CD1a+ cells after transcutaneous application on human skin. J. Invest. Dermatol. 126, 1316-1322.

Volodkin, D. V., Larionova, N. I. and Sukhorukov, G. B., 2004a. Protein encapsulation via porous CaCO3 microparticles templating. Biomacromolecules 5, 1962-1972.

Volodkin, D. V., Petrov, A. I., Prevot, M. and Sukhorukov, G. B., 2004b. Matrix polyelectrolyte microcapsules: New system for macromolecule encapsulation. Langmuir 20, 3398-3406.

Waetzig, G. H., Rosenstiel, P., Arlt, A., Till, A., Bräutigam, K., Schäfer, H., Rose-John, S., Seegert, D. and Schreiber, S., 2004. Soluble tumor necrosis factor (TNF) receptor-1 induces apoptosis via reverse TNF signaling and autocrine transforming growth factor-β1. FASEB 19, 91-93.

Wagner, E. F. and Nebreda, A. R., 2009. Signal integration by JNK and p38 MAPK pathways in cancer development. Nat. Rev. Cancer 8, 537-549.

Walling, M. A., Novak, J. A. and Shepard, J. R. E., 2009. Quantum dots for live cell and in vivo imaging. Int. J. Mol. Sci. 10, 441–491.

Wang, C. Y., Mayo, M. W. and Baldwin, A. S., 1996. TNF- and cancer therapy-induced apoptosis: potentiation by inhibition of NF-kappaB. Science 274, 784-787.

Wang, F., Gao, F., Lan, M., Yuan, H., Huang, Y. and Liu, J., 2009. Oxidative stress contributes to silica nanoparticle-induced cytotoxicity in human embryonic kidney cells. Tox. In Vitro 23, 808-815.

Wang, I. C., Tai, L. A., Lee, D. D., Kanakamma, P. P., Shen, C. K. F., Luh, T. Y., Cheng, C. H. and Hwang, K. C., 1991. C60 and water soluble fullerene derivatives as antioxidant against radical-initiated lipid peroxidation. J. Med. Chem. 42, 4614-4620.

Wang, X. Z. and Ron, D., 1996. Stress-induced phosphorylation and activation of the transcription factor CHOP (GADD153) by p38 MAP Kinase. Science 272, 1347-1349.

Watjen, W., Haase, H., Biagioli, M. and Beyersmann, D., 2002. Induction of apoptosis in mammalian cells by cadmium and zinc. Environ. Health Perspect. 110, 865-867.

West, J. L., 2009. Diagnostic and therapeutic applications of nanotechnology. Cancer Res 69, 484s-484s.

Wijayanti, N., Huber, S., Samoylenko, A., Kietzmann, T. and Immenschuh, S., 2004. Role of NF-kappaB and p38 MAP kinase signaling pathways in the lipopolysaccharide-dependent activation of heme oxygenase-1 gene expression. Antioxid. Redox Signal. 6, 802-810.

Wilson, M., Lightbody, J., Donaldson, K., Sales, J. and Stone, V., 2002. Interactions between ultrafine particles and transition metals in vivo and in vitro. Toxicol. Appl. Pharmacol. 184, 172-179.

Wolter, S., Doerrie, A., Weber, A., Schneider, H., Hoffmann, E., von der Ohe, J., Bakiri, L., Wagner, E. F., Resch, K. and Kracht, M., 2008. C-jun controls histone

modifications, NF-kB recruitment, and RNA Polymerase II function to activate the CCL2 gene. Mol. Cell. Biol. 28, 4407-4423

Wood, C. D., Thornton, T. M., Sabio, G., Davis, R. A. and Rincon, M., 2009. Nuclear localization of p38 MAPK in response to DNA damage. Int. J. Biol. Sci. 5, 428-437.

Woodrow Wilson International Center for Scholars, 2011. Nanotechnology consumer products inventory http://www.nanotechproject.org/inventories/consumer/analysis_draft/, Washington, D. C.

Wu, J., Liu, W., Xue, C., Zhou, S., Lan, F., Bi, L., Xu, H., Yang, X. and Zeng, F., 2009. Toxicity and penetration of TiO2 nanoparticles in hairless mice and porcine skin after subchronic dermal exposure. Tox. Lett. 191, 1-8.

Xia, T., Kovochich, M., Brant, J., Hotze, M., Sempf, J., Oberley, T., Sioutas, C., Yeh, J. I., Wiesner, M. R. and Nel, A. E., 2006. Comparison of the abilities of ambient and manufactured nanoparticles to induce cellular toxicity according to an oxidative stress paradigm. Nano Lett. 6, 1794-1807.

Xia, T., Kovochich, M., Liong, M., Mädler, L., Gilbert, B., Shi, H., Yeh, J. I., Zink, J. I. and Nel, A., 2008. Comparison of the mechanism of toxicity of zinc oxide and cerium oxide nanoparticles based on dissolution and oxidative stress properties. ACS Nano 2, 2121-2134.

Xia, X. R., Monteiro-Riviere, N. A. and Riviere, J. E., 2010. Skin penetration and kinetics of pristine fullerenes (C60) topically exposed in industrial organic solvents. Toxicol. Appl. Pharmacol. 242, 29-37.

Xiao, Y., Forry, S. P., Gao, X., Holbrook, R. D., Telford, W. G. and Tona, A., 2010. Dynamics and mechanisms of quantum dot nanoparticle cellular uptake. J. Nanobiotech. 8, 1-9.

Yabe, S. and Sato, T., 2003. Cerium oxide for sunscreen cosmetics. J. Solid State Chem. 171, 7-11.

Yachie, A., Niida, Y., Wada, T., Igarashi, N., Kaneda, H., Toma, T., Ohta, K., Kasahara, Y. and Koizumi, S., 1999 Oxidative stress causes enhanced endothelial cell injury in human heme oxygenase-1 deficiency. J. Clin. Invest. 103, 129-135.

Yu, W. W., Chang, E., Drezek, R. and Colvin, V. L., 2006. Water-soluble quantum dots for biomedical applications. Biochem. Biophys. Res. Comm. 348, 781–786.

Zalewski, P. D., Forbes, I. J. and Betts, W. H., 1993. Correlation of apoptosis with change in intracellular labile Zn(II) using zinquin [(2-methyl-8-ptoluenesulphonamido- 6-quinolyloxy)acetic acid], a new specific fluorescent probe for Zn(II). Biochem. J. 296, 403-408.

Zandi, E., 1997. The IkB kinase complex (IKK) contains two kinase subunits, IKKa and IKKb, necessary for IkB phosphorylation and NF-kB activation. Cell 91, 243-252.

Zarubin, T. and Han, J., 2005. Activation and signaling of the p38 MAP kinase pathway. Cell Res. 15, 11-18.

Zhang, L. W. and Monteiro-Riviere, N. A., 2008. Assessment of quantum dot penetration into intact, tape-stripped, abraded and flexed rat skin. Skin Pharm. Phys. 21, 166-180.

Zhang, L. W. and Monteiro-Riviere, N. A., 2009. Mechanisms of quantum dot nanoparticle cellular uptake. Toxicol. Sci. 110, 138-155.

Zhang, L. W., Yu, W. W., Colvin, V. L. and Monteiro-Riviere, N. A., 2008. Biological interactions of quantum dot nanoparticles in skin and in human epidermal keratinocytes. Toxicol. Appl. Pharmacol. 228, 200-211.

Zhang, T., Stilwell, J. L., Gerion, D., Ding, L., Elboudwarej, O., Cooke, P. A., Gray, J. W., Alivisatos, A. P. and Chen, F. F., 2006. Cellular effect of high doses of silica-coated quantum dot profiled with high throughput gene expression analysis and high content cellomics measurements. Nano Lett. 6, 800-808.

Zou, L. and Elledge, S. J., 2003. Sensing DNA damage through ATRIP recognition of RPA-ssDNA complexes. Science 300, 1542-1548.

Zvyagin, A. V. and Zhao, X., 2008. Imaging of zinc oxide nanoparticle penetration in human skin in vitro and in vivo. J. Biomed. Opt. 13, 064031/1-064031/9.

APPENDIX

A-1. Gene table I. Complete data set of all the genes studied by real time PCR. Key to classified responses: (1) oxidative stress, (2) apoptosis, (3) inflammation, (4) non-inflammatory immune responses.

						CdSe 8hr	CdSe 48hr	CdSe 8hr	CdSe 48hr	CdSe ZnS 8hr	CdSe ZnS 48hr	CdSe ZnS 8hr	CdSe ZnS 48hr	
Pos	Unigene	GeneBank	Symbol	Description	Gene Name	low dose	low dose	high dose	high dose	low dose	low dose	high dose	high dose	Class
A01	Hs.197029	NM_000675	ADORA2A	Adenosine A2a receptor	ADORA2/RDC8	0.60	0.82	0.77	0.50	4.53	1.21	7.06	1.44	2,3
A02	Hs.494997	NM_001735	C5	Complement component 5	CPAMD4	1.01	0.86	1.23	0.47	1.08	0.80	0.91	0.81	3,4
A03	Hs.93210	NM_000562	C8A	Complement component 8, alpha polypeptide	C8A	0.88	1.08	1.07	0.92	0.00	0.86	0.00	1.27	4
A04	Hs.51120	NM_004345	CAMP	Cathelicidin antimicrobial peptide	CAP18/CRAMP	1.00	1.08	-	0.92	-	0.00	0.12	1.27	4
A05	Hs.2490	NM_033292	CASP1	Caspase 1, apoptosis-related cysteine peptidase (interleukin 1, beta, convertase)	ICE/IL1BC	0.89	1.64	0.91	1.18	0.87	1.26	1.21	1.68	2
A06	Hs.138378	NM_001225	CASP4	Caspase 4, apoptosis-related cysteine peptidase	ICE(rel)II/ICEREL-II	0.86	1.09	0.80	0.94	0.93	0.94	0.87	1.22	2
A07	Hs.303649	NM_002982	CCL2	Chemokine (C-C motif) ligand 2	GDCF-2/HC11	0.77	0.71	0.77	0.51	4.03	1.13	6.68	1.57	3
A08	Hs.506190	NM_001837	CCR3	Chemokine (C-C motif) receptor 3	CC-CKR-3/CD193	0.18	0.93	0.20	1.18	0.59	0.88	0.36	1.08	3
A09	Hs.163867	NM_000591	CD14	CD14 molecule	CD14	0.77	0.62	0.52	0.31	0.20	1.09	0.58	0.60	3,4
A10	Hs.1799	NM_001766	CD1D	CD1d molecule	CD1A/R3	0.14	1.08	0.26	0.92	-	0.86	-	1.27	4
A11	Hs.126517	NM_000574	CD55	CD55 molecule, decay accelerating factor for complement (Cromer blood group)	CR/CROM	0.92	1.44	0.93	1.17	0.85	1.39	0.90	1.62	4
A12	Hs.198998	NM_001278	CHUK	Conserved helix-loop-helix ubiquitous kinase	IKBKA/IKK-alpha	1.06	1.21	0.86	1.00	0.86	1.06	0.88	1.47	3
B01	Hs.464422	NM_130386	COLEC12	Collectin sub-family member 12	CLP1/NSR2	0.84	0.62	0.76	0.54	0.89	0.47	0.63	0.58	4
B02	Hs.709456	NM_000567	CRP	C-reactive protein, pentraxin-related	PTX1	0.88	1.08	1.07	0.92	0.92	0.86	0.99	1.27	3,4
B03	Hs.593413	NM_003467	CXCR4	Chemokine (C-X-C motif) receptor 4	CD184/D2S201E	-	0.00	-	0.92	-	0.00	2.64	0.00	4
B04	Hs.292356	NM_000397	CYBB	Cytochrome b-245, beta polypeptide	CGD/GP91-1	0.88	-	1.07	-	0.00	-	0.99	0.12	1,3,4
B05	Hs.105924	NM_004942	DEFB4	Defensin, beta 4	DEFB-2/DEFB102	-	1.08	-	0.92	-	0.86	-	1.27	4
B06	Hs.279611	NM_004406	DMBT1	Deleted in malignant brain tumors 1	GP340/muclin	0.88	-	1.07	-	0.00	-	0.99	-	4
B07	Hs.203717	NM_002026	FN1	Fibronectin 1	CIG/DKFZp686F10164	0.84	0.88	0.91	0.75	0.95	1.13	0.92	1.05	1,4
B08	Hs.517581	NM_002133	HMOX1	Heme oxygenase (decycling) 1	HO-1/HSP32	0.18	3.86	0.22	5.86	0.04	1.60	0.05	2.31	1,4
B09	Hs.37026	NM_024013	IFNA1	Interferon, alpha 1	IFL/IFN	0.13	0.88	0.43	0.82	0.04	2.33	0.23	0.88	4
B10	Hs.93177	NM_002176	IFNB1	Interferon, beta 1, fibroblast	IFB/IFF	0.60	1.54	1.48	1.51	0.55	2.17	1.39	1.95	4
B11	Hs.520414	NM_000416	IFNGR1	Interferon gamma receptor 1	CD119/IFNGR	0.92	0.97	0.71	1.06	1.13	1.06	1.32	1.01	3,4
B12	Hs.634632	NM_005534	IFNGR2	Interferon gamma receptor 2 (interferon gamma transducer 1)	AF-1/IFGR2	1.03	0.90	0.74	0.77	1.38	1.13	1.43	1.04	3,4

A-1 (cont.)

Pos	Unigene	GeneBank	Symbol	Description	Gene Name	CdSe 8hr low dose	CdSe 48hr low dose	CdSe 8hr high dose	CdSe 48hr high dose	CdSe ZnS 8hr low dose	CdSe ZnS 48hr low dose	CdSe ZnS 8hr high dose	CdSe ZnS 48hr high dose	Class
C01	Hs.597664	NM_001556	IKBKB	Inhibitor of kappa light polypeptide gene enhancer in B-cells, kinase beta	IKK-beta/IKK2	1.12	1.12	1.44	0.86	1.17	1.52	1.17	1.13	1,3,4
C02	Hs.193717	NM_000572	IL10	Interleukin 10	CSIF/IL-10	0.51	1.47	1.82	1.54	0.18	1.67	0.13	1.69	3,4
C03	Hs.479347	NM_001559	IL12RB2	Interleukin 12 receptor, beta 2	RP11-102M16.1	0.41	1.00	0.43	0.03	0.51	0.82	0.43	0.66	4
C04	Hs.1722	NM_000575	IL1A	Interleukin 1, alpha	IL-1A/IL1	0.43	0.53	0.48	1.42	1.19	2.41	1.56	0.45	3,4
C05	Hs.126256	NM_000576	IL1B	Interleukin 1, beta	IL-1/IL1-BETA	0.68	1.42	0.61	0.56	7.62	2.01	13.00	2.19	3,4
C06	Hs.306974	NM_173161	IL1F10	Interleukin 1 family, member 10 (theta)	FIL1-theta/FKSG75	0.88	1.08	1.07	-	0.92	-	0.99	-	3
C07	Hs.516301	NM_012275	IL1F5	Interleukin 1 family, member 5 (delta)	FIL1/FIL1(DELTA)	0.00	0.00	1.07	0.92	0.92	0.86	0.99	1.27	3
C08	Hs.278910	NM_014440	IL1F6	Interleukin 1 family, member 6 (epsilon)	FIL1/FIL1(EPSILON)	0.88	0.00	1.07	0.00	0.92	0.00	-	0.00	3
C09	Hs.166371	NM_173205	IL1F7	Interleukin 1 family, member 7 (zeta)	FIL1/FIL1(ZETA)	2.22	0.37	1.87	0.76	0.90	2.14	1.14	1.17	3
C10	Hs.278909	NM_173178	IL1F8	Interleukin 1 family, member 8 (eta)	FIL1/FIL1-(ETA)	0.88	1.08	1.07	0.92	0.92	0.86	0.99	0.00	3
C11	Hs.211238	NM_019618	IL1F9	Interleukin 1 family, member 9	IL-1F9/IL-1H1	2.17	1.08	-	0.92	-	0.86	-	1.27	3
C12	Hs.701982	NM_000877	IL1R1	Interleukin 1 receptor, type I	CD121A/D2S1473	0.75	0.88	0.67	0.74	0.70	0.75	0.68	0.78	3
D01	Hs.25333	NM_004633	IL1R2	Interleukin 1 receptor, type II	CD121b/IL1RB	0.19	0.00	0.08	0.00	0.07	0.86	0.08	0.00	3
D02	Hs.478673	NM_002182	IL1RAP	Interleukin 1 receptor accessory protein	C3orf13/IL-1RAcP	0.79	1.19	1.08	0.95	0.89	1.21	0.86	0.96	3
D03	Hs.675519	NM_017416	IL1RAPL2	Interleukin 1 receptor accessory protein-like 2	IL-1R9/IL1R9	0.22	0.40	0.35	0.33	0.03	0.54	0.31	0.04	3
D04	Hs.659863	NM_003854	IL1RL2	Interleukin 1 receptor-like 2	IL1R-rp2/IL1RRP2	0.21	0.49	0.56	0.66	0.26	0.61	0.29	0.29	3
D05	Hs.81134	NM_000577	IL1RN	Interleukin 1 receptor antagonist	ICIL-1RA/IL-1ra3	1.00	1.08	0.05	0.92	0.21	0.86	-	0.00	3
D06	Hs.654458	NM_000600	IL6	Interleukin 6 (interferon, beta 2)	BSF2/HGF	0.85	0.80	0.82	0.65	7.16	2.04	11.79	2.16	3,4
D07	Hs.522819	NM_001569	IRAK1	Interleukin-1 receptor-associated kinase 1	IRAK/pelle	1.74	0.86	1.07	1.00	1.21	0.80	0.96	0.90	3
D08	Hs.449207	NM_001570	IRAK2	Interleukin-1 receptor-associated kinase 2	IRAK-2	1.15	2.13	0.81	1.73	2.85	1.08	4.26	1.92	3
D09	Hs.436061	NM_002198	IRF1	Interferon regulatory factor 1	IRF-1/MAR	0.89	0.97	0.86	0.83	1.57	1.13	1.64	1.02	3
D10	Hs.72938	NM_002289	LALBA	Lactalbumin, alpha-	MGC138521	0.88	0.00	1.07	0.00	0.92	0.86	0.99	0.00	4
D11	Hs.154078	NM_004139	LBP	Lipopolysaccharide binding protein	MGC22233	0.88	0.00	1.07	0.92	0.92	0.00	0.00	1.27	4
D12	Hs.529517	NM_002343	LTF	Lactotransferrin	GIG12/HLF2	0.88	1.08	1.07	0.00	0.92	0.86	0.99	1.27	4
E01	Hs.660766	NM_015364	LY96	Lymphocyte antigen 96	MD-2/MD2	0.64	1.34	1.02	1.22	0.86	1.01	0.78	1.66	3,4
E02	Hs.524579	NM_000239	LYZ	Lysozyme (renal amyloidosis)	LZM/lysozyme	44.63	-	-	-	-	1.10	-	-	4
E03	Hs.485233	NM_001315	MAPK14	Mitogen-activated protein kinase 14	CSBP1/CSBP2	0.66	0.67	0.93	0.76	0.94	0.88	0.86	0.82	3
E04	Hs.138211	NM_002750	MAPK8	Mitogen-activated protein kinase 8	JNK/JNK1	1.01	0.92	0.89	0.90	1.14	1.27	1.14	1.22	3
E05	Hs.407995	NM_002415	MIF	Macrophage migration inhibitory factor (glycosylation-inhibiting factor)	GIF/GLIF	0.85	0.89	0.88	0.78	1.01	1.04	0.98	1.48	3,4

A-1. (cont.)

						CdSe 8hr	CdSe 48hr	CdSe 8hr	CdSe 48hr	CdSe ZnS 8hr	CdSe ZnS 48hr	CdSe ZnS 8hr	CdSe ZnS 48hr	
Pos	Unigene	GeneBank	Symbol	Description	Gene Name	low dose	low dose	high dose	high dose	low dose	low dose	high dose	high dose	Class
E06	Hs.82116	NM_002468	MYD88	Myeloid differentiation primary response gene (88)	MYD88D	1.09	0.91	0.86	0.73	1.23	0.85	1.35	0.80	3,4
E07	Hs.474781	NM_000631	NCF4	Neutrophil cytosolic factor 4, 40kDa	NCF/P40PHOX	-	1.08	0.12	5.82	0.10	0.86	0.11	1.27	1,4
E08	Hs.654408	NM_003998	NFKB1	Nuclear factor of kappa light polypeptide gene enhancer in B-cells 1	DKFZp686C01211/EBP-1	0.97	0.95	1.21	0.79	1.93	1.05	2.22	1.51	2,3,4
E09	Hs.73090	NM_002502	NFKB2	Nuclear factor of kappa light polypeptide gene enhancer in B-cells 2 (p49/p100)	LYT-10/LYT10	0.89	1.04	0.72	0.73	0.75	0.93	0.69	0.64	1,3,4
E10	Hs.81328	NM_020529	NFKBIA	Nuclear factor of kappa light polypeptide gene enhancer in B-cells inhibitor, alpha	IKBA/MAD-3	1.07	0.91	1.01	0.75	2.20	1.14	2.66	1.37	2
E11	Hs.574741	NM_021209	NLRC4	NLR family, CARD domain containing 4	CARD12/CLAN	0.67	2.39	1.07	1.61	1.04	1.30	0.99	1.91	2
E12	Hs.709191	NM_000625	NOS2	Nitric oxide synthase 2, inducible	HEP-NOS/INOS	0.98	1.08	0.30	0.92	0.02	0.86	0.93	1.27	1,3
F01	Hs.137583	NM_005091	PGLYRP1	Peptidoglycan recognition protein 1	PGLYRP/PGRP	1.13	0.67	0.93	1.08	1.71	1.39	0.71	0.98	4
F02	Hs.282244	NM_052890	PGLYRP2	Peptidoglycan recognition protein 2	HMFT0141/PGLYRPL	-	1.08	1.07	-	-	-	-	1.27	4
F03	Hs.348266	NM_052891	PGLYRP3	Peptidoglycan recognition protein 3	PGRP-Ialpha/PGRPIA	0.52	1.08	0.63	0.92	2.50	0.86	0.92	1.27	4
F04	Hs.2164	NM_002704	PPBP	Pro-platelet basic protein (chemokine (C-X-C motif) ligand 7)	B-TG1/Beta-TG	0.88	1.08	1.07	0.92	0.92	0.00	0.99	1.27	1
F05	Hs.224698	NM_000312	PROC	Protein C (inactivator of coagulation factors Va and VIIIa)	PC/PROC1	0.70	0.58	4.59	0.03	-	0.39	0.25	0.58	2
F06	Hs.709174	NM_000952	PTAFR	Platelet-activating factor receptor	PAFR	1.58	0.26	0.99	-	1.88	2.73	2.13	0.31	3,4
F07	Hs.19413	NM_005621	S100A12	S100 calcium binding protein A12	CAAF1/CAGC	0.25	1.08	-	0.92	0.03	0.86	-	1.27	3,4
F08	Hs.525557	NM_000295	SERPINA1	Serpin peptidase inhibitor, clade A (alpha-1 antiproteinase, antitrypsin), member 1	A1A/A1AT	2.57	1.21	1.73	0.35	2.19	0.83	2.95	1.26	4
F09	Hs.414795	NM_000602	SERPINE1	Serpin peptidase inhibitor, clade E (nexin, plasminogen activator inhibitor type 1), member 1	PAI/PAI-1	0.85	0.84	0.74	0.82	0.92	1.08	0.91	1.09	4
F10	Hs.253495	NM_003019	SFTPD	Surfactant protein D	COLEC7/PSP-D	0.98	0.78	1.10	0.80	0.99	0.69	0.54	0.77	4
F11	Hs.645227	NM_000660	TGFB1	Transforming growth factor, beta 1	CED/DPD1	1.01	0.83	0.63	0.78	0.93	1.00	0.88	0.82	2
F12	Hs.654532	NM_003263	TLR1	Toll-like receptor 1	CD281/DKFZp547I0610	0.00	0.00	0.00	0.00	0.00	0.00	0.00	0.00	3,4
G01	Hs.120551	NM_030956	TLR10	Toll-like receptor 10	CD290	0.03	1.08	0.74	0.92	0.03	0.86	0.32	1.27	3,4
G02	Hs.519033	NM_003264	TLR2	Toll-like receptor 2	CD282/TIL4	0.16	1.01	2.13	1.41	1.01	0.88	1.85	1.46	3
G03	Hs.657724	NM_003265	TLR3	Toll-like receptor 3	CD283	0.37	0.97	0.92	0.85	0.97	0.76	1.36	0.66	3,4
G04	Hs.174312	NM_138554	TLR4	Toll-like receptor 4	ARMD10/CD284	0.63	0.97	0.88	0.66	0.68	0.77	0.72	1.09	3
G05	Hs.662185	NM_006068	TLR6	Toll-like receptor 6	CD286	0.75	0.60	0.82	1.21	0.89	0.68	0.67	0.65	3,4
G06	Hs.660543	NM_138636	TLR8	Toll-like receptor 8	CD288	-	1.08	0.06	0.92	-	0.86	-	1.27	3,4
G07	Hs.87968	NM_017442	TLR9	Toll-like receptor 9	CD289	0.01	1.08	0.34	0.92	0.01	0.00	0.01	0.00	3,4

A-1. (cont.)

						CdSe 8hr	CdSe 48hr	CdSe 8hr	CdSe 48hr	CdSe ZnS 8hr	CdSe ZnS 48hr	CdSe ZnS 8hr	CdSe ZnS 48hr	
Pos	Unigene	GeneBank	Symbol	Description	Gene Name	low dose	low dose	high dose	high dose	low dose	low dose	high dose	high dose	Class
G08	Hs.241570	NM_000594	TNF-α	Tumor necrosis factor (TNF superfamily, member 2)	DIF/TNF-alpha	0.26	1.74	1.07	0.44	0.55	1.59	1.14	0.28	2,3
G09	Hs.279594	NM_001065	TNFRSF1A	Tumor necrosis factor receptor superfamily, member 1A	CD120a/FPF	0.82	1.29	0.78	1.22	0.95	1.16	0.93	1.58	2,3
G10	Hs.368527	NM_019009	TOLLIP	Toll interacting protein	IL-1RAcPIP	1.20	1.54	1.04	1.49	0.95	1.19	1.05	1.39	3
G11	Hs.591983	NM_004620	TRAF6	TNF receptor-associated factor 6	MGC:3310/RNF85	0.91	1.01	0.73	0.78	0.95	1.05	0.81	0.99	3,4
G12	Hs.283022	NM_018643	TREM1	Triggering receptor expressed on myeloid cells 1	TREM-1	-	-	-	-	-	0.10	2.30	-	3

A-2. Gene table II. Complete data set of all the genes studied by real time PCR.

						8h				24h			
Pos	Unigene	GeneBank	Symbol	Description	Gene Name	Sil	Full	QD	TiO_2	Sil	Full	QD	TiO_2
A01	Hs.197029	NM_000675	ADORA2A	Adenosine A2a receptor	ADORA2/RDC8		0.420		1.031		0.632		0.805
A02	Hs.494997	NM_001735	C5	Complement component 5	CPAMD4	0.787	1.211	1.013	1.025	0.668		0.736	0.414
A03	Hs.93210	NM_000562	C8A	Complement component 8, alpha polypeptide	C8A					0.822	1.765	1.122	1.45
A04	Hs.51120	NM_004345	CAMP	Cathelicidin antimicrobial peptide	CAP18/CRAMP								
A05	Hs.2490	NM_033292	CASP1	Caspase 1, apoptosis-related cysteine peptidase (interleukin 1, beta, convertase)	ICE/IL1BC	0.678	0.798	0.867	0.943				
A06	Hs.138378	NM_001225	CASP4	Caspase 4, apoptosis-related cysteine peptidase	ICE(rel)II/ICEREL-II	1.181	0.846	0.883	1.051	1.202	1.713	1.398	1.062
A07	Hs.303649	NM_002982	CCL2	Chemokine (C-C motif) ligand 2	GDCF-2/HC11	0.807	0.620	0.770	0.878	1.281	1.269	0.999	1.033
A08	Hs.506190	NM_001837	CCR3	Chemokine (C-C motif) receptor 3	CC-CKR-3/CD193	0.648	0.995	0.807	0.715	0.955	0.824	1.071	1.360
A09	Hs.163867	NM_000591	CD14	CD14 molecule	CD14					1.013	0.912	0.242	0.745
A10	Hs.1799	NM_001766	CD1D	CD1d molecule	CD1A/R3					0.403	14.23	2.762	12.85
A11	Hs.126517	NM_000574	CD55	CD55 molecule, decay accelerating factor for complement (Cromer blood group)	CR/CROM	1.117	1.014	1.013	1.050				
A12	Hs.198998	NM_001278	CHUK	Conserved helix-loop-helix ubiquitous kinase	IKBKA/IKK-alpha	0.945	0.626	0.774	0.837	1.944	2.259	1.50	0.949
B01	Hs.464422	NM_130386	COLEC12	Collectin sub-family member 12	CLP1/NSR2	0.653	1.129	0.933	0.963	1.757	1.592	1.283	0.770
B02	Hs.709456	NM_000567	CRP	C-reactive protein, pentraxin-related	PTX1					0.877	1.441	0.971	0.810
B03	Hs.593413	NM_003467	CXCR4	Chemokine (C-X-C motif) receptor 4	CD184/D2S201E								
B04	Hs.292356	NM_000397	CYBB	Cytochrome b-245, beta polypeptide	CGD/GP91-1								
B05	Hs.105924	NM_004942	DEFB4	Defensin, beta 4	DEFB-2/DEFB102								
B06	Hs.279611	NM_004406	DMBT1	Deleted in malignant brain tumors 1	GP340/muclin								
B07	Hs.203717	NM_002026	FN1	Fibronectin 1	CIG/DKFZp686F10164	0.545	1.106	0.917	1.139				
B08	Hs.517581	NM_002133	HMOX1	Heme oxygenase (decycling) 1	HO-1/HSP32	27.62	1.134	0.739	0.795	1.685	2.240	1.762	1.732
B09	Hs.37026	NM_024013	IFNA1	Interferon, alpha 1	IFL/IFN	0.483	0.955	0.862	1.011	11.15	1.789	1.475	0.627
B10	Hs.93177	NM_002176	IFNB1	Interferon, beta 1, fibroblast	IFB/IFF					1.129	1.34	1.455	2.15
B11	Hs.520414	NM_000416	IFNGR1	Interferon gamma receptor 1	CD119/IFNGR	0.946	1.024	0.691	0.915	0.861	2.598	1.521	3.281
B12	Hs.634632	NM_005534	IFNGR2	Interferon gamma receptor 2 (interferon gamma transducer 1)	AF-1/IFGR2	0.908	0.759	0.866	0.824	1.311	1.615	1.491	1.331
C01	Hs.597664	NM_001556	IKBKB	Inhibitor of kappa light polypeptide gene enhancer in B-cells, kinase beta	IKK-beta/IKK2	0.919	1.202	1.000	1.138	0.904	1.698	1.726	1.417
C02	Hs.193717	NM_000572	IL10	Interleukin 10	CSIF/IL-10	0.785	1.233	0.502	1.344	1.124	2.259	1.151	1.683
C03	Hs.479347	NM_001559	IL12RB2	Interleukin 12 receptor, beta 2	RP11-102M16.1	0.584	0.828	0.428	0.642	1.455	1.075	0.684	1.896

A-2. (cont.)

						8h				24h			
Pos	Unigene	GeneBank	Symbol	Description	Gene Name	Sil	Full	QD	TiO_2	Sil	Full	QD	TiO_2
C04	Hs.1722	NM_000575	IL1A	Interleukin 1, alpha	IL-1A/IL1	0.604	1.261	1.360	0.791		1.041	2.123	5.595
C05	Hs.126256	NM_000576	IL1B	Interleukin 1, beta	IL-1/IL1-BETA	0.777	0.798	0.550	1.089	5.126	2.258	2.374	2.181
C06	Hs.306974	NM_173161	IL1F10	Interleukin 1 family, member 10 (theta)	FIL1-theta/FKSG75					4.239	1.898	1.257	2.264
C07	Hs.516301	NM_012275	IL1F5	Interleukin 1 family, member 5 (delta)	FIL1/FIL1(DELTA)								
C08	Hs.278910	NM_014440	IL1F6	Interleukin 1 family, member 6 (epsilon)	FIL1/FIL1(EPSILON)								
C09	Hs.166371	NM_173205	IL1F7	Interleukin 1 family, member 7 (zeta)	FIL1/FIL1(ZETA)	0.281	1.324	0.967	0.521				
C10	Hs.278909	NM_173178	IL1F8	Interleukin 1 family, member 8 (eta)	FIL1/FIL1-(ETA)	2.429	1.178	0.837	2.163	29.49	14.72	13.95	36.11
C11	Hs.211238	NM_019618	IL1F9	Interleukin 1 family, member 9	IL-1F9/IL-1H1	0.393		1.468					
C12	Hs.701982	NM_000877	IL1R1	Interleukin 1 receptor, type I	CD121A/D2S1473	0.650	0.825	0.857	0.930		5.483	1.837	
D01	Hs.25333	NM_004633	IL1R2	Interleukin 1 receptor, type II	CD121b/IL1RB	1.009	0.237	0.466	0.238	0.629	1.555	1.165	0.960
D02	Hs.478673	NM_002182	IL1RAP	Interleukin 1 receptor accessory protein	C3orf13/IL-1RAcP	0.916	1.664	1.027	1.364	0.634	0.617	0.241	
D03	Hs.675519	NM_017416	IL1RAPL2	Interleukin 1 receptor accessory protein-like 2	IL-1R9/IL1R9	0.601	0.989	1.390	0.688	1.987	2.388	1.327	2.130
D04	Hs.659863	NM_003854	IL1RL2	Interleukin 1 receptor-like 2	IL1R-rp2/IL1RRP2	1.112	0.653	0.991	0.558		0.514	0.910	1.413
D05	Hs.81134	NM_000577	IL1RN	Interleukin 1 receptor antagonist	ICIL-1RA/IL-1ra3	0.837	1.284	0.499	0.462	0.402	1.637	1.086	1.204
D06	Hs.654458	NM_000600	IL6	Interleukin 6 (interferon, beta 2)	BSF2/HGF	1.515	0.814	0.878	0.769				
D07	Hs.522819	NM_001569	IRAK1	Interleukin-1 receptor-associated kinase 1	IRAK/pelle	0.889	1.196	1.180	1.876	2.644	2.418	1.575	1.080
D08	Hs.449207	NM_001570	IRAK2	Interleukin-1 receptor-associated kinase 2	IRAK-2	0.768	0.580	0.700	0.644	2.705	2.290	3.198	3.198
D09	Hs.436061	NM_002198	IRF1	Interferon regulatory factor 1	IRF-1/MAR	0.756	1.298	0.819	1.206	1.389	0.630	0.739	0.820
D10	Hs.72938	NM_002289	LALBA	Lactalbumin, alpha-	MGC138521					0.765	1.544	1.454	1.813
D11	Hs.154078	NM_004139	LBP	Lipopolysaccharide binding protein	MGC22233								
D12	Hs.529517	NM_002343	LTF	Lactotransferrin	GIG12/HLF2								
E01	Hs.660766	NM_015364	LY96	Lymphocyte antigen 96	MD-2/MD2	0.841	1.045	0.847	1.036				
E02	Hs.524579	NM_000239	LYZ	Lysozyme (renal amyloidosis)	LZM/lysozyme	0.273		0.988		1.817	1.237	1.093	0.899
E03	Hs.485233	NM_001315	MAPK14	Mitogen-activated protein kinase 14	CSBP1/CSBP2	0.728	1.054	0.920	1.148				1.158
E04	Hs.138211	NM_002750	MAPK8	Mitogen-activated protein kinase 8	JNK/JNK1	0.770	0.849	0.940	0.937	1.263	1.582	1.480	1.509
E05	Hs.407995	NM_002415	MIF	Macrophage migration inhibitory factor (glycosylation-inhibiting factor)	GIF/GLIF	0.935	1.197	0.998	1.161	1.557	1.809	1.575	1.626
E06	Hs.82116	NM_002468	MYD88	Myeloid differentiation primary response gene (88)	MYD88D	0.769	1.181	1.180	1.335	1.669	1.350	1.085	0.904
E07	Hs.474781	NM_000631	NCF4	Neutrophil cytosolic factor 4, 40kDa	NCF/P40PHOX		1.155		1.112	1.249	1.742	1.447	1.784
E08	Hs.654408	NM_003998	NFKB1	Nuclear factor of kappa light polypeptide gene enhancer in B-cells 1	DKFZp686C01211/EBP-1	0.896	0.901	0.947	0.902				

A-2. (cont.)

						8h				24h			
Pos	Unigene	GeneBank	Symbol	Description	Gene Name	Sil	Full	QD	TiO_2	Sil	Full	QD	TiO_2
E09	Hs.73090	NM_002502	NFKB2	Nuclear factor of kappa light polypeptide gene enhancer in B-cells 2 (p49/p100)	LYT-10/LYT10	0.717	1.292	1.136	1.288	1.470	1.298	1.163	0.802
E10	Hs.81328	NM_020529	NFKBIA	Nuclear factor of kappa light polypeptide gene enhancer in B-cells inhibitor, alpha	IKBA/MAD-3	1.116	1.034	0.954	0.995	1.176	1.76	2.209	1.356
E11	Hs.574741	NM_021209	NLRC4	NLR family, CARD domain containing 4	CARD12/CLAN	0.366	0.520	0.813	0.526	1.046	1.113	1.113	0.651
E12	Hs.709191	NM_000625	NOS2	Nitric oxide synthase 2, inducible	HEP-NOS/INOS					1.910	2.593	1.993	0.552
F01	Hs.137583	NM_005091	PGLYRP1	Peptidoglycan recognition protein 1	PGLYRP/PGRP								
F02	Hs.282244	NM_052890	PGLYRP2	Peptidoglycan recognition protein 2	HMFT0141/PGLYRPL					7.073	11.47	4.892	9.837
F03	Hs.348266	NM_052891	PGLYRP3	Peptidoglycan recognition protein 3	PGRP-Ialpha/PGRPIA			0.334					
F04	Hs.2164	NM_002704	PPBP	Pro-platelet basic protein (chemokine (C-X-C motif) ligand 7)	B-TG1/Beta-TG								
F05	Hs.224698	NM_000312	PROC	Protein C (inactivator of coagulation factors Va and VIIIa)	PC/PROC1								
F06	Hs.709174	NM_000952	PTAFR	Platelet-activating factor receptor	PAFR		1.887						
F07	Hs.19413	NM_005621	S100A12	S100 calcium binding protein A12	CAAF1/CAGC								
F08	Hs.525557	NM_000295	SERPINA1	Serpin peptidase inhibitor, clade A (alpha-1 antiproteinase, antitrypsin), member 1	A1A/A1AT	1.225	1.594	1.016	1.019				
F09	Hs.414795	NM_000602	SERPINE1	Serpin peptidase inhibitor, clade E (nexin, plasminogen activator inhibitor type 1), member 1	PAI/PAI-1	0.788	1.092	0.797	1.079	0.769	1.553		1.961
F10	Hs.253495	NM_003019	SFTPD	Surfactant protein D	COLEC7/PSP-D	0.410	0.582	0.740	0.506	0.976	1.473	0.883	1.296
F11	Hs.645227	NM_000660	TGFB1	Transforming growth factor, beta 1	CED/DPD1	0.871	1.033	1.008	1.135	146.5	170.3	110.0	404.2
F12	Hs.654532	NM_003263	TLR1	Toll-like receptor 1	CD281/DKFZp547I0610					0.935	1.548	1.617	1.765
G01	Hs.120551	NM_030956	TLR10	Toll-like receptor 10	CD290						2.639	0.749	0.799
G02	Hs.519033	NM_003264	TLR2	Toll-like receptor 2	CD282/TIL4								
G03	Hs.657724	NM_003265	TLR3	Toll-like receptor 3	CD283	1.169	2.587	1.795	1.920	0.634	1.213	1.140	
G04	Hs.174312	NM_138554	TLR4	Toll-like receptor 4	ARMD10/CD284	1.134	0.852	0.930	0.994	0.744	1.416	1.379	0.837
G05	Hs.662185	NM_006068	TLR6	Toll-like receptor 6	CD286	1.085	1.841	1.361	0.969	1.089	1.005	0.948	0.872
G06	Hs.660543	NM_138636	TLR8	Toll-like receptor 8	CD288					1.278	1.866	1.377	1.277
G07	Hs.87968	NM_017442	TLR9	Toll-like receptor 9	CD289								
G08	Hs.241570	NM_000594	TNF-α	Tumor necrosis factor (TNF superfamily, member 2)	DIF/TNF-alpha								
G09	Hs.279594	NM_001065	TNFRSF1A	Tumor necrosis factor receptor superfamily, member 1A	CD120a/FPF	0.895	1.105	0.902	1.003	0.444	0.535	0.356	0.397
G10	Hs.368527	NM_019009	TOLLIP	Toll interacting protein	IL-1RAcPIP	1.155	0.707	1.016	0.753	0.836	1.133	0.860	0.366
G11	Hs.591983	NM_004620	TRAF6	TNF receptor-associated factor 6	MGC:3310/RNF85	1.133	0.773	0.979	0.791	1.389	1.320	1.216	0.645
G12	Hs.283022	NM_018643	TREM1	Triggering receptor expressed on myeloid cells 1	TREM-1	1.284			3.535	1.377	1.578	1.376	0.923

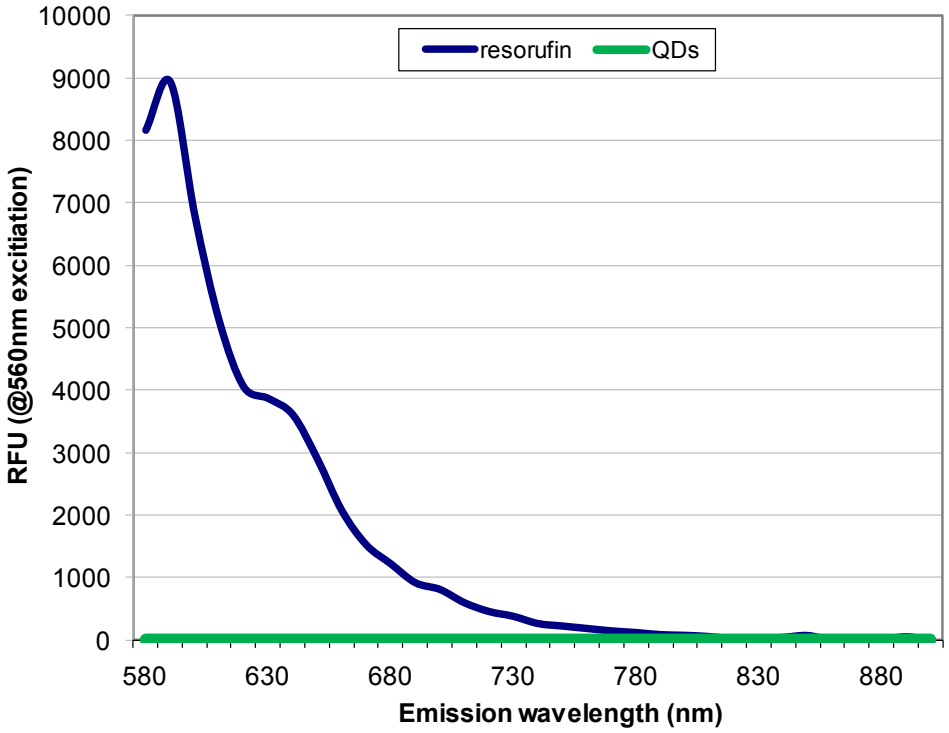

A-3. Fluorescence compatibility. Fluorescence spectral emission wavelengths of QDs and resorufin, product of resazurin (i.e. the viability marker), when excited at 560 nm. Resazurin assay data was collected at 590 nm.

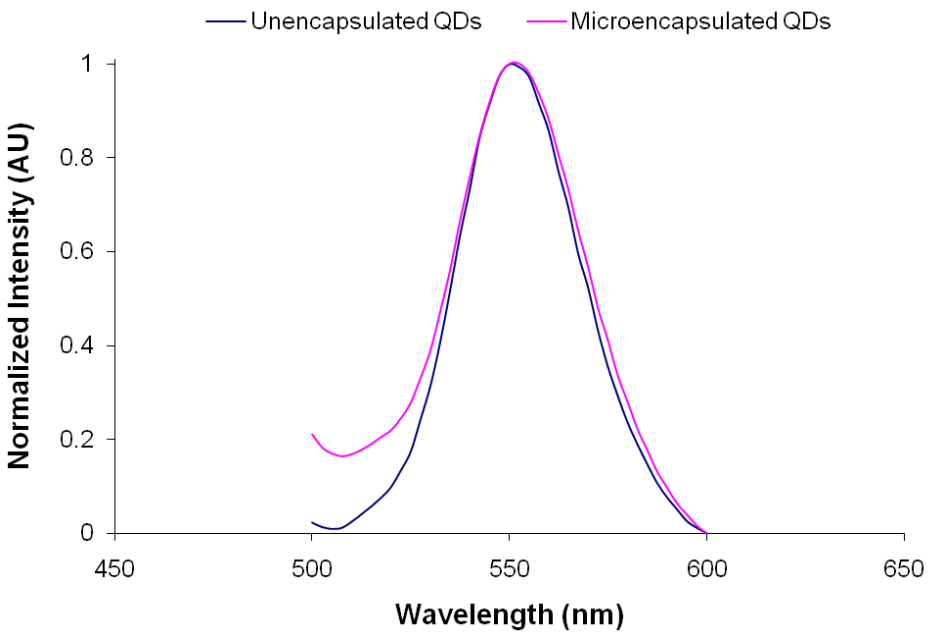

Figure A-4. Unencapsulated QD and QDMC fluorescence emission spectra (after normalization to peak intensity). Because no spectral shift to longer wavelength occurs upon microencapsulation, the quantum dots are not self-quenching within the microcapsules after microencapsulation. The spectra are essentially the same, and there is no evidence of the characteristic red-shift that is associated with self-quenching.

VITA

Name: Amelia Antonia Romoser

Address: Interdisciplinary Faculty of Toxicology
Department of Veterinary Physiology and Pharmacology
College of Veterinary Medicine
Texas A&M University
4466 TAMU
College Station, TX 77843-4466

Email Address: aromoser@cvm.tamu.edu

Education: B.S., Bioenvironmental Sciences, Texas A&M University, 2008
Ph.D., Toxicology, Texas A&M University, 2012